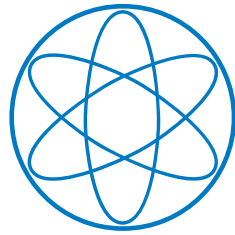


PHYSIK-DEPARTMENT



Upgrade of the COMPASS calorimetric trigger
and determination of
the charged-pion polarizability

Dissertation von Stefan Huber



TECHNISCHE UNIVERSITÄT
MÜNCHEN

Technische Universität München
Physik Department E18

Upgrade of the COMPASS calorimetric trigger
and determination of the charged-pion polarisability

Stefan Huber

Vollständiger Abdruck der von der Fakultät für Physik der Technischen Universität München zur Erlangung des akademischen Grades eines

Doktors der Naturwissenschaften

genehmigten Dissertation.

Vorsitzender:

apl. Prof. Dr. Norbert Kaiser

Prüfer der Dissertation:

1. Univ-Prof. Dr. Stephan Paul

2. Univ-Prof. Dr. Laura Fabietti

Die Dissertation wurde am 22.12.2016 bei der Technischen Universität München eingereicht und durch die Fakultät für Physik am 17.03.2017 angenommen.

Abstract

COMPASS is a fixed-target experiment at CERN's SPS accelerator. Its focus is to study the structure and spectroscopy of hadrons. It uses hadron and muon beams with momenta up to $200 \text{ GeV}/c$. During the years 2009 and 2012 focus was put on the measurement of so-called Primakoff reactions using a pion beam impinging on a Nickel target. In these reactions a quasi-real photon is exchanged giving access to the regime of low-energy QCD. This exchange has the key signature of very low four-momentum transfers which are selected by cutting on $Q^2 < 1.5 \times 10^{-3} (\text{GeV}/c)^2$.

The focus of these measurements was on final states containing neutral particles. A main ingredient to detect events with highly energetic photons in the final state is the trigger. A new approach using a purely digital implementation in the existing front-end electronics is developed and used during two years of data taking with COMPASS. The full operation principle as well as the performance of this trigger system is discussed.

Using this trigger data taken in 2009 are analyzed focusing on the reaction $\pi^- \text{Ni} \rightarrow \text{Ni} \pi^- \gamma$ where one photon is produced in the final state. From this data a sample of 63000 events is selected and analyzed. This analysis results in the world's most precise value of the charged-pion polarizability of $\alpha_\pi = (2.0 \pm 0.6_{\text{stat.}} \pm 0.7_{\text{syst.}}) \times 10^{-4} \text{ fm}^3$ under the assumption $\alpha_\pi = -\beta_\pi$. This analysis is discussed including all details on the treatment of systematic errors and it was published in [1].

Finally, the data taken in 2012 are discussed. Here the main efforts were put into the preparation of the data-reconstruction as well as the understanding of new simulation framework based on Geant4. The precision of the reconstruction of the electromagnetic calorimeters is improved and the determination of the beam particle ID is implemented in the reconstruction framework. Further the new simulation is compared to the simulation performed with the previous framework as well with data.

Zusammenfassung

COMPASS ist ein Fixed-Target-Experiment am SPS Beschleuniger des CERN. Sein Schwerpunkt ist die Untersuchung der Struktur und die Spektroskopie von Hadronen. Dabei werden Hadronen- und Myonenstrahlen mit Impulsen bis zu $200 \text{ GeV}/c$ verwendet. In den Jahren 2009 und 2012 lag der Schwerpunkt auf der Messung von sogenannten Primakoff Reaktionen unter Verwendung eines Pionenstrahls welcher auf einem Nickel-Target geschossen wurde. Bei diesen Reaktionen werden quasi reelle Photonen ausgetauscht was Zugriff auf das Regime der Niedrigenergie-QCD gibt. Dieser Austausch wird bestimmt von sehr niedrigen Viererimpulsüberträgen, diese werden durch Schneiden auf $Q^2 < 1.5 \times 10^{-3} (\text{GeV}/c)^2$ ausgewählt.

Der Schwerpunkt dieser Messungen waren Endzustände welche neutrale Teilchen enthalten. Ein Hauptbestandteil um Ereignisse mit hochenergetischen Photonen im Endzustand zu erkennen, ist der Trigger. Ein neuer Ansatz für eine rein digitale Implementierung in die bestehende Front-End-Elektronik wurde entwickelt und während zwei Jahren Datennahme mit COMPASS eingesetzt. Das komplette Funktionsprinzip sowie die Leistung dieses Triggersystem wird diskutiert.

Die Daten aus dem Jahr 2009 welche unter Verwendung dieses Triggers genommen wurden sind auf die Reaktion $\pi^- \text{Ni} \rightarrow \text{Ni} \pi^- \gamma$ analysiert. Dabei wird ein Photon im Endzustand erzeugt. Aus diesen Daten wurden 63000 Ereignisse ausgewählt und analysiert. Diese Analyse führt zu dem weltweit präzisesten Wert der Polarisierbarkeit von geladenen Pionen, $\alpha_\pi = (2.0 \pm 0.6_{\text{stat.}} \pm 0.7_{\text{Syst.}}) \times 10^{-4} \text{ fm}^3$ unter der Annahme $\alpha_\pi = -\beta_\pi$. Diese Analyse wird in allen Details diskutiert einschließlich der Behandlung von systematischen Fehlern und wurde in [1] veröffentlicht.

Schließlich werden die im Jahr 2012 genommenen Daten diskutiert. Die meisten Anstrengungen wurden in die Vorbereitung der Daten-Rekonstruktion gesetzt sowie das Verständnis des neuen Simulations-Frameworks basierend auf Geant4. Die Genauigkeit der Rekonstruktion der elektromagnetischen Kalorimeter wurde verbessert und die Bestimmung der Teilchenstrahl-ID wurde in die Rekonstruktion eingebaut. Weiterhin wird die neue Simulation mit der bisherigen Simulation verglichen sowie mit den gemessenen Daten.

Contents

| | | |
|----------|---|-----------|
| 1 | Introduction | 1 |
| 1.1 | Hadron physics | 1 |
| 1.2 | Polarizability | 2 |
| 1.3 | Theoretical approach to the pion polarizability | 3 |
| 1.4 | Experimental situation | 4 |
| 1.5 | The Primakoff Compton reaction | 6 |
| | | |
| 2 | COMPASS | 11 |
| 2.1 | The Beam Line | 11 |
| 2.2 | The target region | 13 |
| 2.3 | Tracking | 14 |
| 2.4 | Calorimeter | 16 |
| 2.4.1 | ECAL2 | 16 |
| 2.4.2 | ECAL1 | 18 |
| 2.5 | Particle identification | 19 |
| 2.5.1 | CEDAR | 19 |
| 2.5.2 | RICH | 20 |
| | | |
| 3 | The calorimeter readout and the trigger system | 23 |
| 3.1 | The MSADC readout system | 23 |
| 3.1.1 | Mezzanine card | 23 |
| 3.2 | The data format | 26 |
| 3.3 | The new data format | 27 |

CONTENTS

| | | |
|----------|---|-----------|
| 3.4 | Trigger strategy | 28 |
| 3.5 | Signal detection and feature extraction | 29 |
| 3.6 | Time and energy calibration | 34 |
| 3.7 | Interface to the carrier-card | 34 |
| 3.7.1 | 2009 setup | 34 |
| 3.7.2 | 2012 setup | 35 |
| 3.8 | Interface to the backplane | 36 |
| 3.8.1 | 2009 setup | 36 |
| 3.8.2 | 2012 setup | 36 |
| 3.9 | The 2012 backplane card | 37 |
| 3.10 | High speed interface between the backplane cards | 38 |
| 3.11 | Implementation on the backplane | 40 |
| 3.12 | Slow-control | 42 |
| 3.13 | Commissioning of the trigger | 42 |
| 3.14 | Elements in the trigger | 45 |
| 3.15 | Tuning the thresholds | 48 |
| 3.16 | Performance | 49 |
| 4 | Extraction of the charged-pion polarizability from 2009 data | 53 |
| 4.1 | Target | 53 |
| 4.2 | Trigger | 53 |
| 4.3 | Event selection | 54 |
| 4.3.1 | Reconstruction of photons | 54 |
| 4.3.2 | Preselection | 56 |
| 4.3.3 | Excluded data | 56 |
| 4.3.4 | Quality cuts on the scattered particle | 56 |
| 4.3.5 | Cut on the trigger mask | 57 |
| 4.3.6 | Cuts on the beam parameters | 57 |
| 4.3.7 | Vertex position | 58 |
| 4.3.8 | Four-momentum transfer | 58 |

| | | |
|----------|--|-----------|
| 4.3.9 | Cut on additional tracks in the spectrometer | 59 |
| 4.3.10 | Cut on the recoil proton detector | 59 |
| 4.3.11 | Exclusivity cut | 60 |
| 4.3.12 | Cut on the invariant mass of the $\pi\gamma$ -system | 60 |
| 4.3.13 | Cut on the transverse momentum of the scattered pion (p_T) | 61 |
| 4.3.14 | Cut on the number of photons in the final state | 61 |
| 4.3.15 | Identification of the beam particle | 63 |
| 4.3.16 | Beam momentum measurement by the BMS | 63 |
| 4.4 | Monte Carlo Simulation | 63 |
| 4.4.1 | Beam and vertex generation | 63 |
| 4.4.2 | Event generators | 64 |
| 4.4.3 | Simulating the COMPASS experiment | 65 |
| 4.5 | Backgrounds | 67 |
| 4.5.1 | Different particles in the initial state | 67 |
| 4.5.2 | Processes with more than two final state particles | 68 |
| 4.5.3 | Background from strong interaction | 73 |
| 4.6 | Systematic effects | 74 |
| 4.6.1 | Muon measurement | 74 |
| 4.6.2 | Uncertainty on the radiative corrections | 75 |
| 4.6.3 | Influence of the background subtraction | 75 |
| 4.6.4 | Correctness of the chiral expansion | 75 |
| 4.6.5 | Effect of the cut on the invariant mass | 76 |
| 4.7 | The result in context with other experiments and theory | 76 |
| 5 | Preparing the analysis for the data taken in 2012 | 81 |
| 5.1 | CEDAR | 81 |
| 5.1.1 | CEDAR reconstruction | 82 |
| 5.1.2 | Getting the event samples | 82 |
| 5.1.3 | Calculating the probabilities | 84 |
| 5.1.4 | Getting the likelihood and calculating the PID | 85 |

| | | |
|----------|---|------------|
| 5.2 | Performance | 89 |
| 5.2.1 | Stability and application to other years | 89 |
| 5.2.2 | Determination of the beam composition | 91 |
| 5.3 | Beam momentum | 91 |
| 5.4 | ECAL calibration | 95 |
| 5.4.1 | Electron calibration | 95 |
| 5.4.2 | LED calibration | 95 |
| 5.4.3 | New feature extraction | 97 |
| 5.4.4 | π^0 -calibration | 99 |
| 5.4.5 | Energy correction dependent on the position in the cell | 102 |
| 5.4.6 | Dependence of the reconstructed cluster position on the position inside a cell | 103 |
| 5.5 | Alignment | 104 |
| 5.6 | Reconstruction | 105 |
| 5.7 | Simulation | 109 |
| 5.7.1 | Verification of the simulation | 109 |
| 5.7.2 | Detector efficiencies | 113 |
| 6 | Conclusion and Outlook | 115 |
| A | Calibration files for 2012 | 121 |
| A.1 | CEDAR 1 calibration file | 121 |
| A.2 | CEDAR 2 calibration file | 128 |
| A.3 | ECAL2 position dependent correction file | 136 |

Chapter 1

Introduction

1.1 Hadron physics

All known forces and particles existing in nature are described by the standard model of particle physics. The well understood theory of quantum electrodynamics is unified with the theory of weak interaction to the so-called electro-weak theory which was finally experimentally confirmed by the discovery of the Higgs boson in 2012. The last ingredient of this theory is the strong interaction which is described by quantum chromodynamics (QCD).

The basic ingredient of this theory is that the quarks carry in addition to their electromagnetic charge a so-called color-charge which is mediated by the gauge-bosons of this theory, the gluons. As the gluons carry color-charge themselves, they may interact with each other leading to a very complex structure of the theory. For instance the quarks are confined into hadrons which are the particles that can be observed in nature.

The most abundant hadrons are the nucleons, proton and neutron. They belong to the baryons which are systems of three quarks bound into one hadron. On the other hand there are the mesons which can be described as a bound system of quarks and anti-quarks. The lightest meson is the pion and thus it can be seen as the most fundamental hadron.

In order to get a better understanding of QCD the internal structure of these particles needs to be understood. This can be performed on nucleons where for instance the contribution of the individual particles to the total hadron spin is studied [2]. Another approach is to understand more basic properties of the particles like the polarizability. This is done in this thesis.

1.2 Polarizability

Polarizability is a quantity which describes the stiffness of an object in the presence of electric or magnetic fields. In a classical picture it describes how far charges will be separated by an electric field or how strong the currents are which are induced by a magnetic field. The first order contribution to the Hamiltonian can be written in terms of the dipole polarizabilities α_{E_1} and β_{M_1} resulting in

$$(1.1) \quad H = \frac{1}{2}\alpha_{E_1}\vec{E}^2 + \frac{1}{2}\beta_{M_1}\vec{B}^2,$$

in presence of the electric field \vec{E} and the magnetic field \vec{B} . For systems like the hydrogen atom the electric polarizability can be measured by directly applying an electric field and measuring the energy shifts given by the quadratic Stark effect [3]. They can be calculated by second-order perturbation theory

$$(1.2) \quad \Delta E = -\frac{9}{4}a^3\vec{E}^2,$$

with the atomic radius a . The polarizability is then given by $\alpha_{E_1} = 9/2a^3 \approx 6.66 \times 10^{-4} \text{ nm}^3$. In this case the main contribution comes from the displacement of the electron shell relatively to the nucleus. As this binding is purely electromagnetic it is relatively weak and the polarizability is large.

In case of hadrons with dimensions in the order of 1 fm and a binding mainly mediated by the strong interaction the measurement principle has to be changed. The induced force by the electric and magnetic fields are now mediated by the interaction with single photons. This is a very important measurement because the understanding of the polarizabilities implies a certain knowledge of the internal structure and the forces holding the object together and leads to a better understanding about quantum chromodynamics (QCD). In case of stable hadrons like the proton the measurement is performed by Compton scattering of a photon beam on the hadron $p\gamma \rightarrow p\gamma$, fig. 1.1. The result of the polarizabilities are $\alpha_p = (12.0 \pm 0.6) \times 10^{-4} \text{ fm}^3$ and $\beta_p = (1.9 \pm 0.5) \times 10^{-4} \text{ fm}^3$ [4].

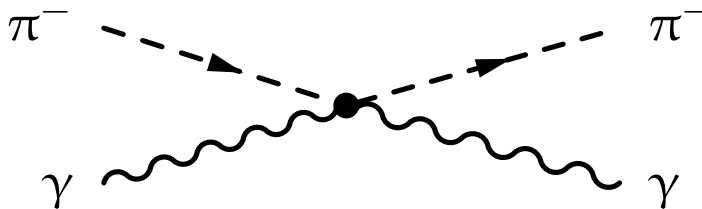


Figure 1.1 Sketch of the Compton scattering process for a pion.

In case of particles with a short life-time like the pion the measurement is more complicated because no target made of pions can be constructed. This means the pion-photon

interaction has to be imposed by embedding it into another process and extrapolating the result to the case of real Compton scattering. The methods applied here will be discussed throughout this chapter.

1.3 Theoretical approach to the pion polarizability

The polarizability of a hadron is a parameter stemming from its internal structure and thus should be predictable by the theory of strong interaction at low energies. Due to the properties of QCD the coupling constant α_s is growing in the regime of low energies and thus a perturbative approach in α_s is not possible. This has the well-known consequence of the confinement of quarks into hadrons.

In order to handle effects taking place at low energies another approach has to be taken. One possibility is to use effective field theories and here specially the Chiral Perturbation Theory χ PT [5]. The QCD Lagrangian has the symmetry $SU(3)$ where the left and right-handed currents of the quarks are mixed only by the mass term

$$(1.3) \quad \mathcal{L}_M = q_L^\dagger M q_R + q_R^\dagger M q_L.$$

In case of vanishing masses of the three light quarks the symmetry is split up to a $SU(3)_L \times SU(3)_R$ symmetry where the two chiral states transform independently. Even without the explicit breaking of the symmetry by mass, due to a non vanishing vacuum expectation value of the mixture of left-handed quarks with right-handed antiquarks

$$(1.4) \quad \langle 0 | \bar{Q} Q | 0 \rangle = \langle 0 | \bar{Q}_L Q_R + \bar{Q}_R Q_L | 0 \rangle \neq 0$$

the symmetry is spontaneously broken and the $Q\bar{Q}$ condensate leads to the appearance of eight mass-less Goldstone bosons which can be identified by the pseudo-scalar mesons appearing in the ground-state octet: $\pi^\pm, \pi^0, K^\pm, K^0, \bar{K}^0, \eta$. They gain mass because of the non-vanishing quark mass in a realistic description.

These mesons are the fundamental particles in this theory and thus their properties are of even greater importance. The perturbative expansion can now be performed in terms of momentum and the mass of the Goldstone bosons rather than in terms of a coupling constant. And thus the dipole polarizabilities of the charged pion can be calculated in this framework:

$$(1.5) \quad \alpha_\pi + \beta_\pi = \frac{\alpha_{\text{em.}}}{16\pi^2 F_\pi^2 M_\pi} \left(c_{1\pm} + d_{1\pm} \cdot \frac{M_\pi^2}{16\pi^2 F_\pi^2} + O(M_\pi^4) \right) [6].$$

Here $F_\pi = (130.41 \pm 0.03) \text{ MeV}$ [4] is the pion decay constant and $c_{1+}, c_{1-}, d_{1+}, d_{1-}$ are values derived from the so-called low energy constants of χ PT which are fundamental to the theory but have to be determined by experiment. In future they might be calculated by lattice QCD [7]. In the next to leading order expansion six of these constants have to be known. It has to be stated that in leading order the polarizability is proportional to

1 INTRODUCTION

c_{1-} and therefore the difference of the constants \bar{l}_6 and \bar{l}_5 describing the pion weak form factors F_V and F_A

$$(1.6) \quad c_{1-} = \frac{2}{3} (\bar{l}_6 - \bar{l}_5) = 6 \frac{F_A}{F_V}$$

which have been extracted in [8] from the radiative pion decay $\pi^+ \rightarrow e^+ \nu_e \gamma$. Using this as an input, χ PT predicts a value of the pion polarizability of

$$(1.7) \quad \begin{aligned} \alpha_\pi - \beta_\pi &= (5.7 \pm 1.0) \times 10^{-4} \text{ fm}^3 \\ \alpha_\pi + \beta_\pi &= (0.16 \pm 0.10) \times 10^{-4} \text{ fm}^3 [6]. \end{aligned}$$

There are predictions from other theoretical models for this quantity. For instance the quark confinement model [9] gives a value of $\alpha_\pi - \beta_\pi = 7.1 \times 10^{-4} \text{ fm}^3$ and some version of dispersion relations [10] result even in $\alpha_\pi - \beta_\pi = (13.6 \pm 2.1) \times 10^{-4} \text{ fm}^3$. All theories predict a similar value for $\alpha_\pi + \beta_\pi$ to be close to zero. The result of the dispersive calculation is disputed [11, 12]. Due to the success of χ PT the value predicted by this theory is considered rather solid while it still waits for experimental confirmation.

1.4 Experimental situation

In order to measure the desired process of Compton scattering on the pion, it has to be embedded into a more complex process. The variants exploited so far are shown in fig. 1.3.

The extraction of the polarizability from e^+e^- -collision in the reaction depicted in fig. 1.3 (a) is published using the compilation of several experiments as data source. Non of these experiments have been explicitly performed to extract the polarizability and the data are re-analyzed by different groups. The reaction has to be extrapolated to the case of Compton scattering using crossing symmetry, implying knowledge about resonance parametrizations. This cannot be done in a model independent way [13] and leads to a rather wide spread of results depending on the data source and the analyzer, table 1.1.

The method using radiative pion photoproduction $\gamma p \rightarrow \gamma \pi^+ n$ has been tackled in two experiments, fig. 1.3 (b). The first measurement [15] has rather poor statistical accuracy and a value of $\alpha_\pi = (20 \pm 12) \times 10^{-4} \text{ fm}^3$ was extracted. The more recent measurement [16] determines the polarizability by comparing the measured data with two different theoretical predictions for the cross-section. The final result of this measurement is $\alpha_\pi - \beta_\pi = 11.6 \pm 1.5_{\text{stat.}} \pm 3.0_{\text{syst.}} \pm 0.5_{\text{mod.}}$. This process implies pion exchange and meson baryon-resonance contributions, which requires some theoretical modeling. The uncertainty from this modeling is rather complex and the quoted error of $\pm 0.5 \times 10^{-4} \text{ fm}^3$ underestimated [30].

The method that has been utilized in ref. [14] uses the same Primakoff [31] method as applied in this work, fig. 1.3 (c), and will be explained in the next chapter. The experi-

Table 1.1 Overview over the previous measurements of the pion polarizability [29].

| | process | $\alpha_\pi - \beta_\pi [10^{-4} \text{ fm}^{-3}]$ |
|--|--|--|
| experimental analyzes | | |
| Sigma (Serpukhov) [14] | $\pi^- Z \rightarrow \pi^- \gamma Z$ | $13.6 \pm 2.8 \pm 2.4$ |
| PACHRA/Lebedev Inst. [15] | $\gamma p \rightarrow \gamma \pi^+ n$ | 40 ± 24 |
| A2(MAMI/JGU) [16] | $\gamma p \rightarrow \gamma \pi^+ n$ | $11.6 \pm 1.5 \pm 3.0 \pm 0.5$ |
| re-analysis <i>D.Babusci et.al.</i> [17] | | |
| PLUTO (PETRA/DESY) [18] | $\gamma\gamma \rightarrow \pi^+ \pi^-$ | $38.2 \pm 9.6 \pm 11.4$ |
| DM1 (DCI/Orsay) [19] | $\gamma\gamma \rightarrow \pi^+ \pi^-$ | 34.4 ± 9.2 |
| DM2 (DCI/Orsay) [19] | $\gamma\gamma \rightarrow \pi^+ \pi^-$ | 52.6 ± 14.8 |
| MARK II (EPPEP/SLAC) [20] | $\gamma\gamma \rightarrow \pi^+ \pi^-$ | 4.4 ± 3.2 |
| re-analysis Donoghue and Holstein [21] | | |
| Mark II | $\gamma\gamma \rightarrow \pi^+ \pi^-$ | 5.3 ± 3.5 |
| combined analysis Kaloshin et.al. [22] | | |
| Mark II, Crystal Ball (DESY) [23] | $\gamma\gamma \rightarrow \pi^+ \pi^-$ | 5.3 ± 1.0 |
| combined analysis Fil'kov et.al. [10] | | |
| Mark II, TPC/2 γ [24], CELLO [25], VENUS [26], ALEPH [27], BELLE [28] | $\gamma\gamma \rightarrow \pi^+ \pi^-$ | $13.0^{+2.6}_{-1.9}$ |

mental setup used a pion beam with a momentum of 40 GeV/ c impinging mainly on a carbon target. Other targets were used for systematic checks. The 7000 events, collected allowed to extract a polarizability value α_π with a statistical precision of $\pm 1.4 \times 10^{-4} \text{ fm}^3$. The possibility to check systematic effects is limited in this case due to this small amount of events.

Dedicated measurements statistically agree with a confidence level of 0.67, fig. 1.3. Having this in mind a world average of $\alpha_\pi - \beta_\pi = (12.7 \pm 2.5) \times 10^{-4} \text{ fm}^3$ is calculated, which is in significant tension with the theoretical prediction [6]. This is the main motivation for the new measurement described in this thesis, aiming for clarification of the situation.

1 INTRODUCTION

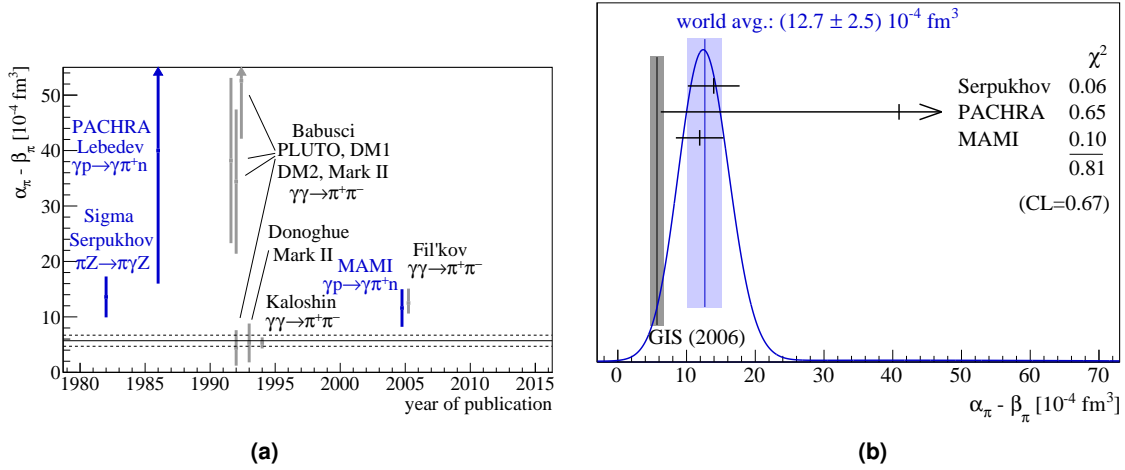


Figure 1.2 Overview over all previous measurements of the pion polarizability(a). The dedicated measurements are indicated in blue and all others in grey. The theoretical prediction from [6] is shown as a horizontal line. Panel (b) shows the world average computed from the dedicated measurements in blue, it is compared with the theoretical prediction shown as grey band with the label GIS(2006). The confidence level is calculated from the deviation of the individual measurements from the world average.

1.5 The Primakoff Compton reaction

The method discussed here originates from the proposal of Henry Primakoff who described a measurement in which π^0 -mesons are produced in the collision of a photon with a photon stemming from the Coulomb field of a nucleus [31]. It was used to measure the π^0 -lifetime by measuring the corresponding production cross-section. Currently there are ongoing efforts at Jefferson Lab to increase the precision [32].

Extending this original idea, one speaks of Primakoff reactions or the Primakoff effect when ultra-relativistic particles scatter off the Coulomb-field quanta surrounding a nucleus. In the case of electrons it was first described by C.F. von Weizsäcker [33] and E.J. Williams [34] for discussing bremsstrahlung. For a reaction which involves the scattering off a Coulomb-field quantum, the cross-section of scattering on a nucleus can be factorized. This factorization gets one term from the cross-section of the real pion-photon scattering process $d\sigma_{\pi\gamma\rightarrow X}/d\Phi_n$ and one term from the density of quasi-real photons stemming from the coulomb field. This factorization is called the Weizsäcker-Williams approximation or the equivalent-photon approximation (EPA)[35]

$$(1.8) \quad \frac{d\sigma_{(A,Z)}^{\text{EPA}}}{ds dQ^2 d\Phi_n} = \frac{Z^2 \alpha}{\pi(s - m_\pi^2)} F^2(Q^2) \frac{Q^2 - Q_{\min}^2}{Q^4} \frac{d\sigma_{\pi\gamma\rightarrow X}}{d\Phi_n}.$$

Z denotes the charge of the nucleus and $F^2(Q^2)$ its electromagnetic form-factor. The cross-section, starting at $Q^2 = Q_{\min}^2$, has its maximum at $Q^2 = 2Q_{\min}^2$ and then a strong drop with increasing squared four-momentum transfer $Q^2 = -(p_{\text{beam}}^\mu - p_X^\mu)^2$. This dependence of the cross-section is usually referred to as Primakoff peak. The minimal four-

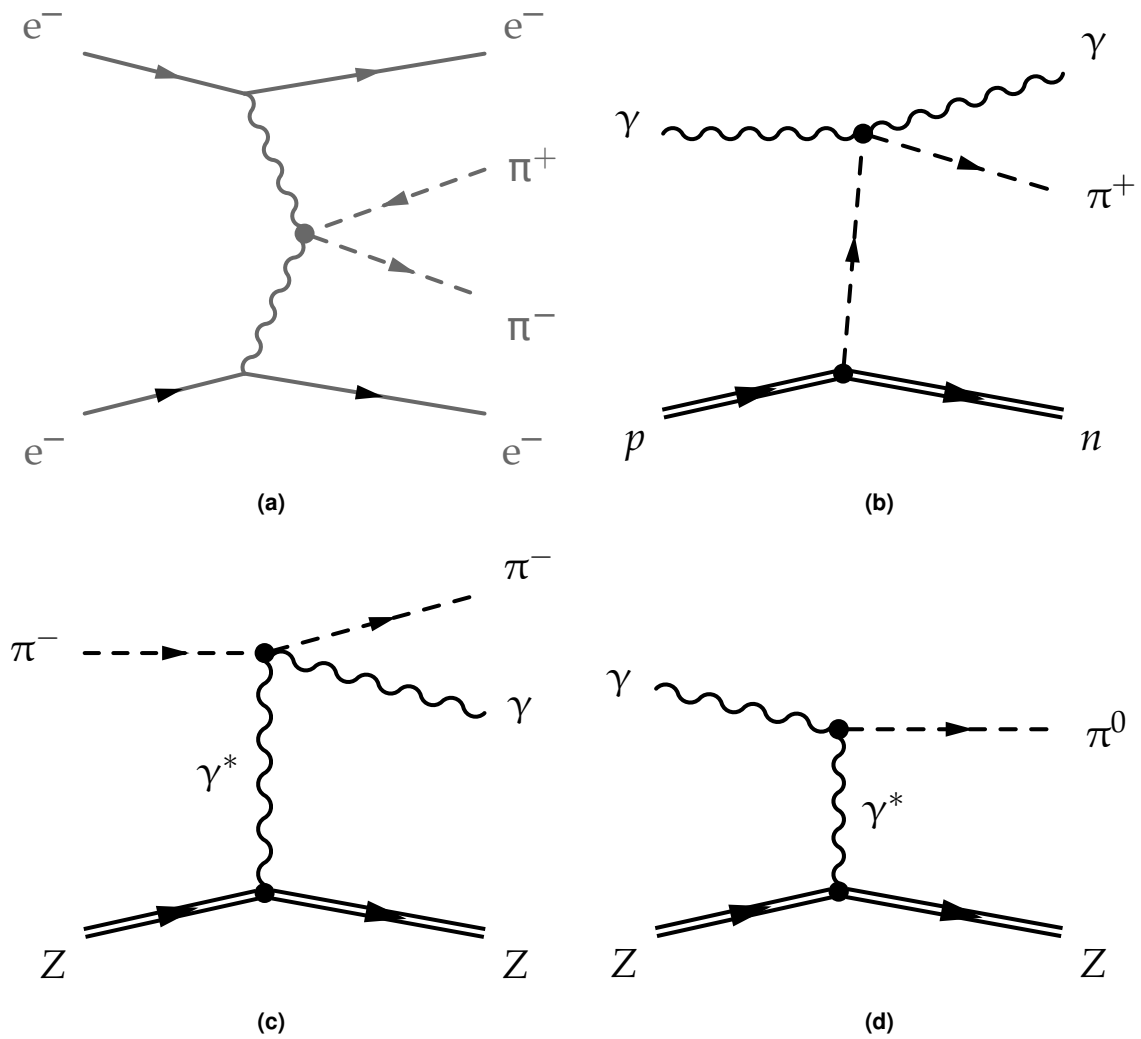


Figure 1.3 (a-c) show processes embedding the pion Compton scattering. In (d) the original Primakoff process is shown.

1 INTRODUCTION

momentum transfer can be evaluated to be

$$(1.9) \quad Q_{\min}^2 = \frac{(s - m_\pi^2)^2}{4E_{\text{beam}}^2}.$$

The electromagnetic form-factor can be described, for a rough estimate of the low- Q^2 behavior, using the sharp-radius approximation

$$(1.10) \quad F^2(Q^2) = \left(\frac{3}{(qr)^3} (\sin(qr) - qr \cos(qr)) \right)^2,$$

where r is the charge-radius of the nucleus and $q = \sqrt{Q^2}$. In fig. 1.4 a simulated spectrum of q is shown.

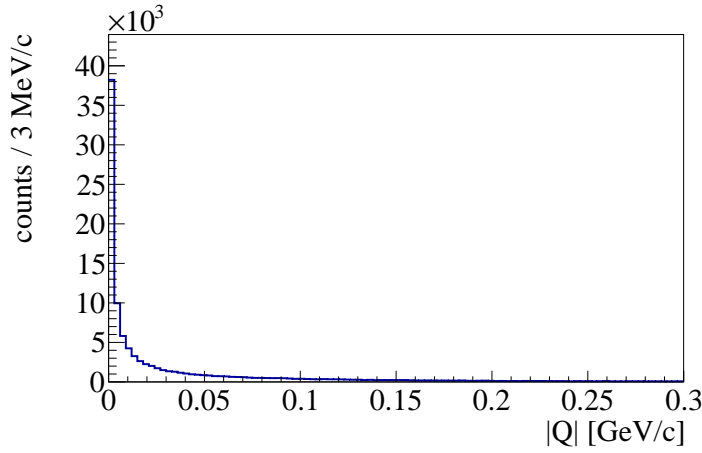


Figure 1.4 Four-momentum transfer taken from simulation for the reaction $\pi^- \text{Ni} \rightarrow \text{Ni} \pi^- \gamma$. For better visualization of the features in the peak-region the quantity $q = \sqrt{Q^2}$ is shown. The horizontal scale is chosen to match fig. 4.6.

In the analysis, the four-momentum-transfer for Primakoff processes is constrained to of $Q^2 < 1.5 \times 10^{-3} (\text{GeV}/c)^2$. In this case the energy transferred to the nucleus can be approximated to be $\Delta E = Q^2 / (2M_{\text{Ni}}) < 13 \text{ keV}$. It is negligible compared to all other involved energies and their uncertainties, and the energy conservation for the reaction $\pi^- \text{Ni} \rightarrow \text{Ni} \pi^- \gamma$ therefore can be written as

$$(1.11) \quad E_{\text{beam}} - E_\gamma - E_\pi = 0.$$

Extraction of the pion polarizability is possible by connecting the cross-section of Compton scattering [36, 37]

$$(1.12) \quad \frac{d\sigma_{\pi\gamma}}{d\Omega} = \left(\frac{d\sigma_{\pi\gamma}}{d\Omega} \right)_{\text{Born}} - \frac{\alpha m_\pi^3 (s - m_\pi^2)^2}{4s (s z_+ + m_\pi^2 z_-)} \left(z_-^2 (\alpha_\pi - \beta_\pi) + \frac{s^2}{m_\pi^4} z_+^2 (\alpha_\pi + \beta_\pi) \right).$$

with eq. 1.8 giving a full description of the scattering on the Nickel nucleus. The po-

larizability effect appears as first order correction to the pure born cross-section in the center-of-mass frame. In this equation $\alpha \approx 1/137$ is the electromagnetic fine-structure constant, s is the invariant mass of the $\pi\gamma$ final-state and $z_{\pm} = 1 \pm \cos\theta_{\text{cm}}$ where θ_{cm} is the $\pi\gamma$ scattering angle. Using this formula for the cross-section one can perform the extraction of the polarizabilities by comparing the measured cross-section in the laboratory frame to the cross-section predicted for a point-like pion for which the cross-section is described by the born contribution. The analyzing quantity is the photon energy E_{γ} or rather the ratio of the photon-energy to the beam-energy $x_{\gamma} = E_{\gamma}/E_{\text{beam}}$. In terms of this energy the cross-section factorizes into

$$(1.13) \quad \frac{d\sigma}{dE_{\gamma}} = \left(\frac{d\sigma}{dE_{\gamma}} \right)_{\text{Born}} + \left(\frac{d\sigma}{dE_{\gamma}} \right)_{\text{Pola.}}$$

The born term is given by [38]

$$(1.14) \quad \left(\frac{d\sigma}{dE_{\gamma}} \right)_{\text{Born}} = \frac{4Z^2\alpha^3}{m_{\pi}^2} \frac{E_{\pi}}{E_{\gamma}E_{\text{beam}}} \left\{ \frac{2}{3} \ln \frac{Q_{\text{max}}^2}{Q_{\text{min}}^2} - \frac{19}{9} + 4\sqrt{\frac{Q_{\text{min}}^2}{Q_{\text{max}}^2}} \right\}$$

and the polarizability term by

$$(1.15) \quad \left(\frac{d\sigma}{dE_{\gamma}} \right)_{\text{Pola.}} = \frac{4Z^2\alpha^3\alpha_{\pi}E_{\gamma}}{E_{\text{beam}}^2} \left\{ \ln \frac{Q_{\text{max}}^2}{Q_{\text{min}}^2} - 3 + 4\sqrt{\frac{Q_{\text{min}}^2}{Q_{\text{max}}^2}} \right\}.$$

The smallness of $\alpha_{\pi} + \beta_{\pi} = 0$ is assumed in this case. Fundamentally this cross-section can be iteratively compared to simulation putting different values for the polarizability into the Monte Carlo generator. This is computationally quite expensive and so an approximation to the ratio

$$(1.16) \quad R(x_{\gamma}) = \frac{\frac{d\sigma_{\text{Born}}}{dE_{\gamma}} + \frac{d\sigma_{\text{pol.}}}{dE_{\gamma}}}{\frac{d\sigma_{\text{Born}}}{dE_{\gamma}}}$$

is made by calculating [38]

$$(1.17) \quad R(x_{\gamma}) = \frac{\frac{d\sigma_{\text{meas.}}}{dE_{\gamma}}}{\frac{d\sigma_{\text{MC}}}{dE_{\gamma}}} = 1 + \frac{3}{2} \frac{\alpha_{\pi}m_{\pi}^3x_{\gamma}}{\alpha_{\text{em.}}(1-x_{\gamma})}.$$

This function having only one free parameter α_{π} is then fitted to the measured data.

Chapter 2

COMPASS

2.1 The Beam Line

The beam extracted to the COMPASS experiment consists of secondary hadrons or tertiary muons stemming from the decay of these hadrons. The hadrons are produced by directing a beam of protons, accelerated by the SPS, with momenta of $400 \text{ GeV}/c$ onto the "T6" production target consisting of beryllium. Its length can be chosen to be 50 mm, 100 mm or 500 mm or completely removed. This given length is used in order to tune the intensity of the beam at the COMPASS target. For physics measurements a high beam intensity is required and therefore the maximum length of 500 mm is chosen. The extraction of the protons from the SPS is performed in so called spills of 9.6 s length, of constant intensity (as good as possible), repeating every 48 s. These values may change depending on the configuration of other experiments, which also extract protons from the SPS.

The produced particles are directed towards the COMPASS experiment via the "M2" beam-line providing a set of dipole magnets for momentum filtering as well as quadrupole magnets for focusing the beam. A sketch can be found in fig. 2.1. Depending on its configuration hadron beams, with momenta up to $285 \text{ GeV}/c$, and muon beams up to $200 \text{ GeV}/c$ can be produced. In case a muon beam is desired, a hadron-absorber is installed into the beam line, it consists of beryllium with a total length of 9.9 m.

Hadron beams may have a small contamination of electrons. In order to remove them from the beam an "Electron target" can be inserted into the beam-line. It is a 5 mm thick lead-disk in which the electrons may interact. Due to the loss of momentum and the immediately following dipole magnets most of the electrons are filtered from the beam.

For measuring the momentum of the muon beam a system of six detectors consisting of scintillating fibers, the BMS¹ is installed into the beam-line. This is needed because the muons have a quite significant momentum spread, c.f. fig. 4.11 (b). For the measurements using the hadron beam the BMS is removed because it adds material to the beam line

¹beam momentum station

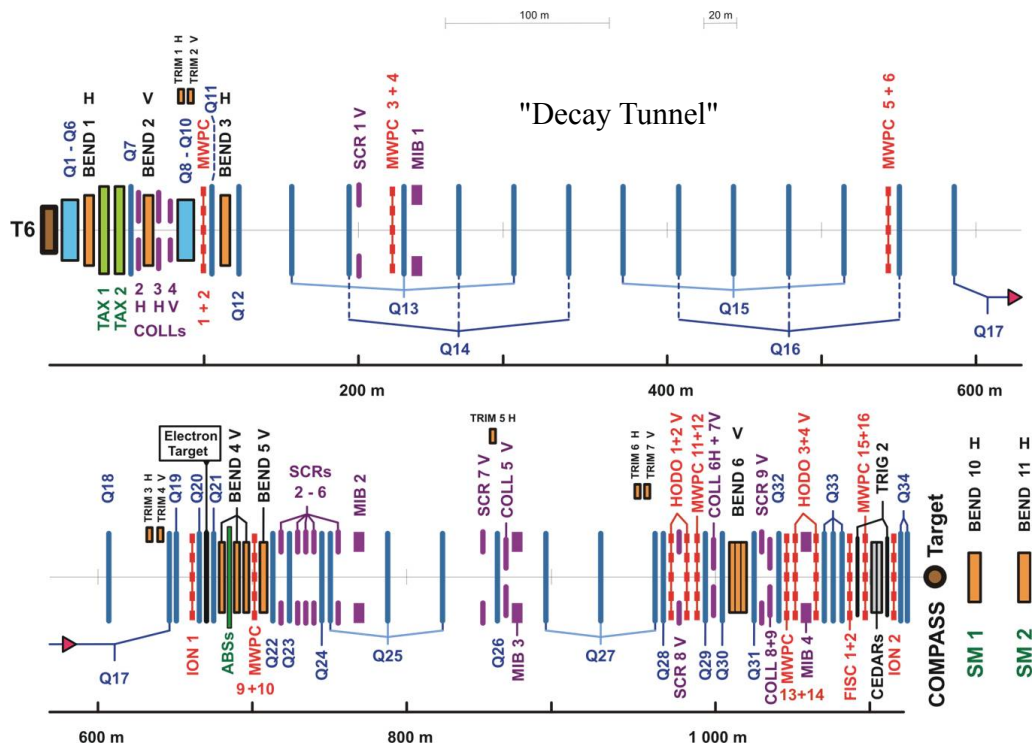


Figure 2.1 Sketch of the M2 beam-line. The focusing quadrupole magnets are indicated with "Q" while the dipole magnets are indicated by "BEND". In order to absorb electrons from the hadron beam the "Electron target" is installed. In case of muon beams the "ABSs"^a is installed absorbing remaining hadrons from the beam.

^aAbsorbers

which would degrade the beam quality. This means, in case of Primakoff data taking the detectors have to be taken in and out after every period which leads to a necessary re-alignment of the BMS because the detectors can only be installed with a limited precision of about a millimeter. The result of this alignment is shown in fig. 2.2.

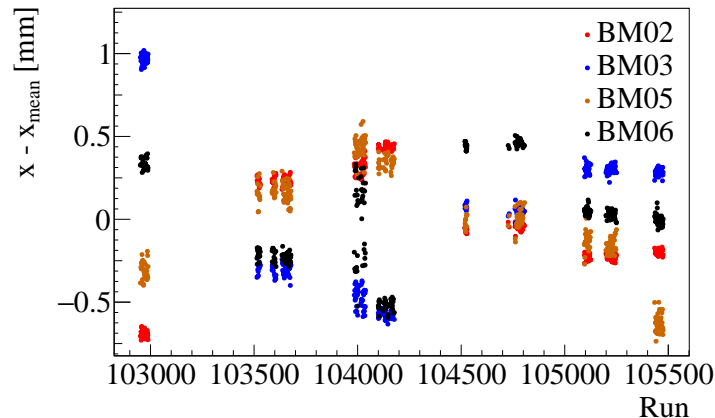


Figure 2.2 Measured position of the BMS detectors as a function of the run number. The detectors BM01 and BM04 are not shown in this plot because they act as reference detectors for the alignment. This means their position is not a free parameter in the alignment procedure but the other planes are aligned relatively in a way that the precision of the reconstructed momentum is optimized.

2.2 The target region

Depending on the investigated physics channels, different targets are installed in COMPASS. For measurements with muon beams usually solid targets at cryogenic temperatures of ammonia (NH_3) or deuterated lithium (${}^6\text{LiD}$) with a polarization system are used. In case of measurements with hadron beams either a target consisting of liquid hydrogen or different solid targets are installed. The materials which have been used so far are lead, carbon, copper, tungsten and nickel.

During the "Primakoff" measurements a setup consisting of a nickel disk with a thickness of 4 mm is used. Additional tungsten targets having a thickness of 25 μm and 50 μm are installed. These have been installed at two different positions 36.5 cm and 41.5 cm downstream of the main target in 2009 and 34 cm downstream in 2012. In that case they add up to one target which is separated approximately in the horizontal center. As it turned out after the beam time, the beam has not been centered on the separation line and most of the particles crossed the thicker disc, fig. 2.3 (c).

In fig. 2.3 (a) the setup used in 2009 is shown. The nickel target is installed at $Z = -72.5$ cm and the two tungsten disks at $Z = -36$ cm and $Z = -31$ cm, are visible.

In 2012 fig. 2.3 (a) the nickel disk is installed slightly further downstream at $Z = -68$ cm and the tungsten target at $Z = -34$ cm.

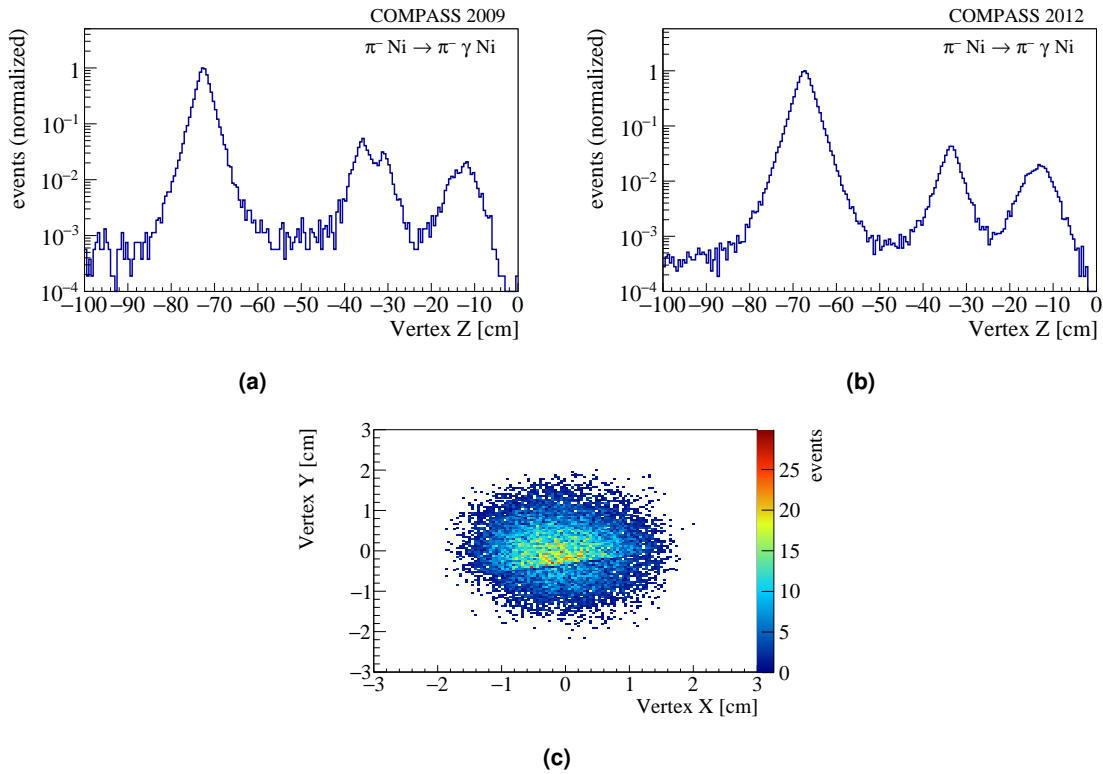


Figure 2.3 Target Z positions for 2009 (a) and 2012 (b) are shown. The peak structures indicate the nickel target around -70 cm and the tungsten targets around 35 cm. The peak around -12 cm corresponds to the silicon detectors and the increased width stems from the worse resolution when having a vertex close to the detector. In (c) the XY-distribution of the vertex in the region of the tungsten target is shown for 2012 data. The sharp edge corresponds to the border between the two target-segments.

In fig. 2.4 the geometry of the target used in 2012 is shown as it is implemented in simulation, the 2009 target looks similar.

2.3 Tracking

COMPASS offers a tracking covering the full range of momenta up to the momentum of the beam. This is achieved by segmenting the spectrometer into two stages. The first stage covers tracks with low momenta and scattering angles up to 180 mrad, the required bending power is achieved by the spectrometer magnet SM1 which operates at a field integral of 1 T m [39]. For tracks with momenta above 5 GeV/ c the second stage is required, where tracks with scattering angles below 30 mrad are measured. It is equipped with a second spectrometer magnet SM2 operated at 4.4 T m

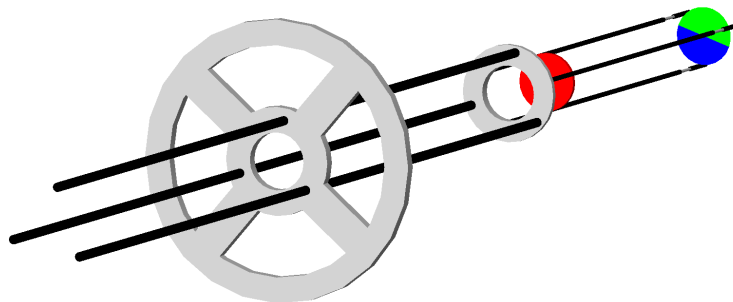


Figure 2.4 The target used for 2012 data-taking as it is implemented in Monte Carlo. The support structures consisting of stainless-steel are shown in grey, the carbon holding-rods are shown in black. The 4 mm nickel-target is indicated in red. The 25 μm tungsten target is shown in blue and the 50 μm one in green.

In order to cover a wide angular range several different detectors are used. Drift chambers and straw-tube detectors cover tracks at the largest angles. Intermediate angles are covered by MWPCs while the smallest angles are covered by scintillating fibers and GEM detectors. A novelty in the spectrometer are the pixelised Gas Electron Multiplier (Pixel-GEM) detectors [40], which allow tracking in the beam region.

Very crucial for the measurements at very low momentum transfers is a good vertex resolution. This is achieved by the silicon microstrip detectors[41, 42, 43] surrounding the target. Twelve planes are installed upstream of the target and eight planes are installed further downstream. These detectors are operated at a temperature of 200 K which increases the detector performance in terms of spacial and time resolution. Especially the spacial resolution of a few micrometers allows to have an angular resolution in the μrad range, fig. 2.5, which is necessary for this measurement.

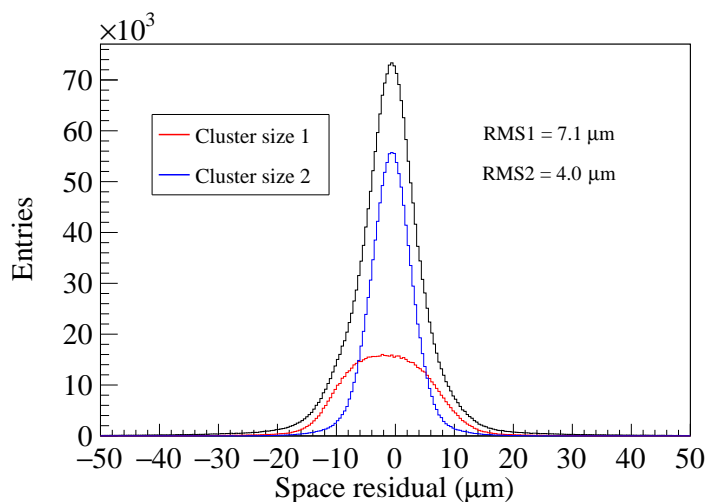


Figure 2.5 Spacial residual of one exemplary silicon plane [44]. The residual for hits spanning one detector strip and hits is shown individually as well as the integral which is shown in black.

2.4 Calorimeter

The COMPASS setup is equipped with two electromagnetic calorimeters since 2004. They are called ECAL1 and ECAL2 and are situated in the Large Angle Spectrometer and in the Small Angle Spectrometer, respectively. End of 2012 the installation of a new detector, called ECAL0, was started downstream the target region which was finalized in 2016. Two hadronic calorimeters are installed directly after ECAL1 and ECAL2. Due to their non-uniform acceptance they are not used in the analysis and not further described in this work, they only contribute by adding material for the muon identification. ECAL0 was not installed during the measurements described in this thesis.

2.4.1 ECAL2

ECAL2 is installed with the front planes at of $Z = 33.25$ m downstream of the target. Due to its acceptance for very forward kinematics (39×29) mrad², this calorimeter contributes most to the analysis performed with hadron beams. It has a transverse extension of (2.44×1.83) m² subdivided into a matrix of 64×48 cells with a squared surface of (3.83×3.83) cm², each. There are three types of detector cells which differ in their resolution as well as in their radiation hardness. In years of data taking with hadron beams the detector features a central hole of 2×2 cells at the place where non-interacting beam particles pass through the detector. In case of data taking with muon beam this hole is extended to 10×10 cells due to the bigger divergence of the beam. The arrangement of the different cell types can be seen in fig. 2.6.

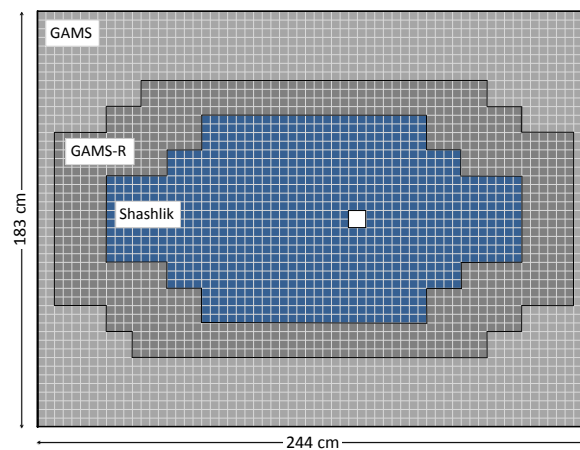


Figure 2.6 The structure of ECAL2 [44] with the different cell types indicated by different colors. The beam hole is shown as white square.

The outer parts of ECAL2 are equipped with cells taken over from the GAMS-2000 experiment [45]. They consist of type TF1 lead glass which has a radiation tolerance of only

400 rad [46]. This corresponds to about one full year of data taking with hadron beam. The intermediate cells are of a similar type but adding 0.2 % of cerium improves their radiation-hardness to 3 krad. Both module types add to a radiation length of $16 X/X_0$. The readout principle is based on Čerenkov light which is detected by PMTs².

The central part of ECAL2 which is closest to the beam-axis suffers strongest from the effects of radiation. In order to cope with this a module type called Shashlik is used here. It consists of alternating layers of lead with a thickness of 0.8 mm and plastic scintillator with a thickness of 1.55 mm which add up to a total module length of 39 cm. Thus, a total radiation-length of $22.5 X/X_0$ is achieved [46]. The tested radiation hardness without module degradation is 500 krad [46] this corresponds to about 20 years of operation in normal COMPASS conditions with hadron beam at the places which are strongest affected. The structure is kept together by steel rods with a diameter of 2 mm and the scintillating light is provided to a PMT read-out by wavelength shifting fibres of four different types which are placed in a spiral structure through the layers and thus limiting the areas of dead material. Inside the steel rods a part of the energy of the photons is absorbed leading to a non uniform energy resolution as a function of the position within a cell. This is compensated by an additional calibration, discussed in section 5.4.5.

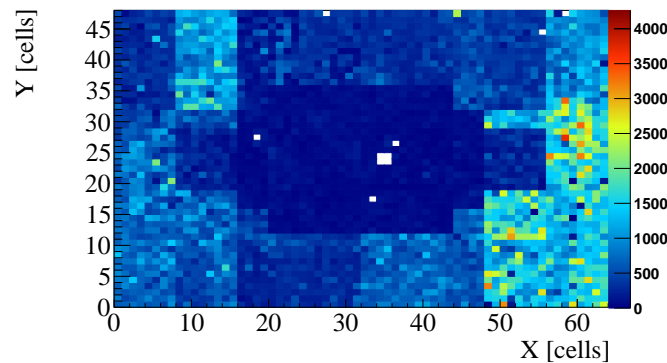


Figure 2.7 Distribution of LED amplitudes per cell for ECAL2. It can be seen that the inner part consisting of Shashlik cells has only little response on the LED amplitude. Additional rectangular structures in this plot stem from different LEDs used for different regions.

The analog signal of each PMT is transferred to a shaper module in which the signal is amplified and modified in a way, that its width is 120 ns FWHM. These signals are further transferred via flat-cables to the MSADC³-readout described in section 3.1.

In order to monitor time dependent fluctuations a system of LED pulsers is used which inject a signal with a fixed amplitude into the detector-cells. This signal is read out and calibrations are produced for every spill which compensate variations of the signal, e.g. due to thermal effects. As can be seen from fig. 2.7, the amplitude of the LED signal depends strongly on the cell to which it is connected. Especially the shashlik cells have

²photomultiplier tubes

³Mezzanine Sampling ADC

(due to their lead layers) a very bad coupling to the LED and the average amplitudes usually are below 100. The effect of these small amplitudes is discussed in section 5.4.2

The amplification and thus the dynamic range of each cell can be adjusted by changing the high voltage of each LED. This is configured in a way that the central most region can detect photons which deposit up to the full beam energy within one cell. Followed by a region where photons up to 160 GeV are covered which again is followed by a region reaching up to 60 GeV, fig. 2.8. The preliminary calibrations are adjusted using the known amplitude response to the LED system. A further, more precise, calibration is achieved by scanning the detector with an electron beam with a momentum of 60 GeV/c. The full surface is covered by moving the detector and thus centering each individual cell on the electron beam until a desired amount of events is collected. This calibration is further refined using reconstructed data and described in section 5.4.

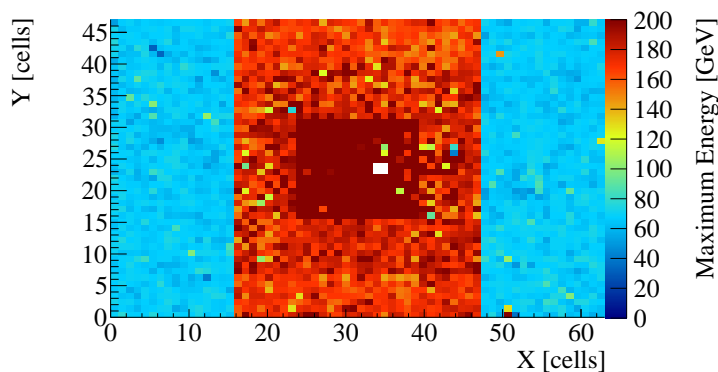


Figure 2.8 Maximum measurable energy per cell in ECAL2. The different regions are adopted to the different maximum photon energies which are expected.

2.4.2 ECAL1

ECAL1 extends the kinematic coverage of ECAL2 to larger angles, and is installed $Z = 13.99$ m downstream of the target region in 2008 and 2009 while it was moved closer to the target with a new position of 11.08 m in other years, mainly due a different position of the second spectrometer magnet SM2 which was shifted by 2.7 m. It has a size of (3.97×2.86) m² while a central hole with dimensions of (1.07×0.67) m² is kept free of material. It covers a range of photon-angles of 48–178 mrad in horizontal direction and 27–128 mrad vertically. The hole dimensions in horizontal direction together with ECAL2 does not provide a perfect coverage of angles, leaving a gap of 11 mrad. This gap has been closed before the beginning of the 2012 data-taking by adding 208 additional modules of the shashlik-type to the center of the detector, described above.

In general the detector is not as homogenous as ECAL2, as it consists of cells with different dimensions. The central part is covered using the same TF1 modules from the GAMS-2000 [45] experiment as in ECAL2 while the outer regions built-up with larger

cells. In vertical direction 572 "MAINZ" [47] modules consisting of SF57 lead glass with a surface of $(7.5 \times 7.5) \text{ cm}^2$ are installed while in horizontal direction 320 "OLGA" [48] modules consisting of SF5 lead glass and having an extension of $(14.1 \times 14.1) \text{ cm}^2$. The overall configuration can be seen in fig. 2.9.

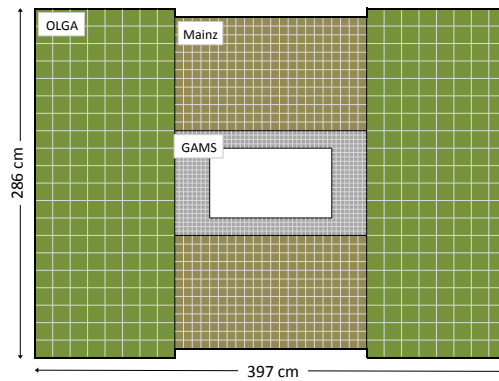


Figure 2.9 The structure of ECAL1 [44] with the different cell types indicated. The beam hole is shown as white square.

The monitoring of the long-term stability is performed with a laser-based system injecting pulses with a known amplitude into the detector. This laser is again monitored by a set of several thermally stabilized photodiodes, which provide normalization information for the amplitude.

The calibration procedure is identical to the one described for ECAL2 above. While the momentum of the electron-beam is only $15 \text{ GeV}/c$ in this case, due to the lower maximum energy which can be detected by ECAL1. It is configured to detect photons up to an energy of 50 GeV .

The signal from each module is passed through the same shaping modules which are used for ECAL2 while the ADC cards are different. They provide a sampling with 77.76 MS/s ⁴ with a reduced resolution of 10 bit, more details can be found in [49].

2.5 Particle identification

2.5.1 CEDAR

The two CEDAR⁵ [44, 50] detectors are installed 30 m upstream of the COMPASS target. A schematic view can be found in fig. 2.10. They are used to identify the beam particles.

⁴Mega samples per second

⁵Čerenkov Differential Counters with Achromatic Ring Focus

The operational principle of these detectors is that particles, passing through the detector, which is filled with gaseous Helium at about 10.5 bar, emit Čerenkov-light. This light is focused via a mirror and a system of lenses onto a ring of 8 PMTs which are behind a diaphragm. The angle of the emitted Čerenkov-light can be calculated by

$$(2.1) \quad \cos \Theta = \frac{p}{n \cdot m \cdot c}$$

where n is the refractive index of the medium the particle passes through, m the particle mass and p the momentum of the particle. In case of the COMPASS-beam in which the particles have a constant momentum of 191 GeV/ c with a spread of a few GeV/ c the Čerenkov-angle only depends on the mass of the particle and consequently on the particle type. By adjusting the pressure inside the detectors the operational mode can be set as the Čerenkov-photons of different particles types are now focused onto the diaphragm.

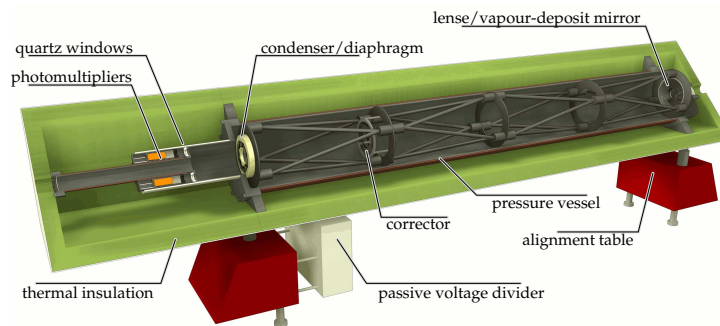


Figure 2.10 Cross section through one CEDAR detector. For more details about the various components c.f. [44].

2.5.2 RICH

Charged particles passing through the first spectrometer magnet are identified by a RICH⁶ detector. The tank of this detector is either filled with a radiator gas C₄F₁₀ or with N₂ in a volume of a length of 3 m. In order to limit the number of Čerenkov-photons from beam-particles a pipe with a radius of 5 cm filled with helium is installed and absorbs these photons. In the years before 2012 this pipe consisted of steel with a wall thickness of 150 μm and thus added a significant amount of material to the experimental setup. For instance a particle crossing the pipe at an angle of 6 mrad passes through 1.4 radiation lengths [51]. The setup has been improved prior to the 2012 data-taking period by replacing this pipe by a thin version consisting of a foil of aluminized mylar with a wall thickness of 27 μm [52]. With this setup the particle with the parameters described above has to pass through a radiation length of 1.4 X0 [51] only.

⁶Ring Imaging Čerenkov

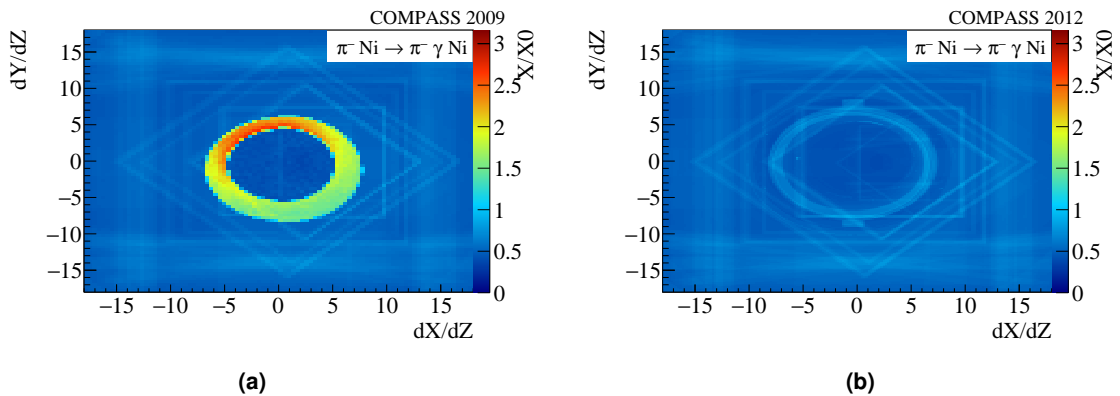


Figure 2.11 Distribution of the material budget expressed in radiation lengths seen by a neutral particle extrapolated from the target to the surface of ECAL2 as a function of the angle relative to the z-axis. The setup from 2009 (a) shows a prominent circular enhancement corresponding to the steel RICH-pipe. In the setup used in 2012 (b) this enhancement is significantly reduced.

The performance of the RICH detector vastly depends on the radiator gas, where for instance the lower threshold for detecting pions, kaons and protons is $2.5 \text{ GeV}/c$, $9 \text{ GeV}/c$ and $17 \text{ GeV}/c$ for C_4F_{10} while it is $5.6 \text{ GeV}/c$, $20 \text{ GeV}/c$ and $38 \text{ GeV}/c$ for N_2 respectively [44]. Although the momentum ranges are slightly different for these two gases the efficiency for pion-kaon separation for momenta below $45 \text{ GeV}/c$ is similar and has a value of 95%. For the study of the processes $\pi^- \text{Ni} \rightarrow \text{Ni} \pi^- \gamma$ and $\pi^- \text{Ni} \rightarrow \pi^- \pi^0 \text{Ni}$ the RICH detector is of limited use, as due to the small scattering angles most of the charged particles pass through the RICH detector only within the beam-pipe c.f. fig. 2.12. For the physics stemming from $\pi^- \text{Ni} \rightarrow \pi^- \pi^0 \pi^0 \text{Ni}$ the RICH detector can be used for certain kinematics which is described in section 5.1.2.

Due to the consideration of material in terms of radiation length, the RICH is operated with nitrogen filling during the Primakoff data-taking periods. In this case the average number of photons per ring for pions gets reduced from 56 to 11.6. This limits the efficiency for tracks, which do not have their full path length in the sensitive region of the RICH.

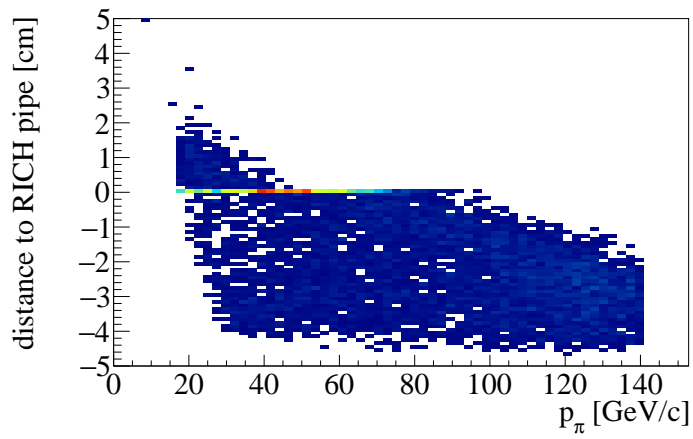


Figure 2.12 Minimum distance of the scattered π^- from the RICH pipe as function of the pion momentum. A negative value indicates that the track fully lies within the gas-volume of the RICH pipe, while a value of zero indicates that the track crosses the RICH pipe. Only about 25 % of the tracks travel a distance outside of the RICH pipe and thus may get a useful RICH information.

Chapter 3

The calorimeter readout and the trigger system

For the measurement of the pion polarizability in 2009 the assumption $\alpha_\pi = -\beta_\pi$ was used. In this case the value of α_π can be studied by considering only backward-scattering hence high photon energies. This led to the development of a trigger based on the total energy deposited in the central region of ECAL2 [53, 54, 55]. This trigger with a threshold value of about 63 GeV was used for the extraction of the pion-polarizability [1], where photon energies above 76 GeV have been considered. Further it yields a high efficiency for channels with the final-state $\pi^- \text{Ni} \rightarrow \pi^- \pi^0 \text{Ni}$. Finally, it has been used to study the Primakoff-production of $\pi^- \text{Ni} \rightarrow \pi^- \pi^0 \pi^0 \text{Ni}$ [56], where a threshold on the energy deposited in the trigger region of 67 GeV has been applied on software level. This trigger strategy has been kept for the 2012 data-taking campaign and was extended in order to have a bigger kinematic coverage for the $\pi^- \text{Ni} \rightarrow \text{Ni} \pi^- \gamma$ channel.

3.1 The MSADC readout system

Up to three calorimeters are installed in COMPASS with ECAL1 read out with the SADC¹ system [49]. ECAL0 and ECAL2 are read out by the MSADC [57].

3.1.1 Mezzanine card

The MSADC (**M**ezzanine **S**ampling **A**DC) is an electronics board which houses four ADC chips of the type ADS5270 [58], which allow digitizing eight analog inputs with a sampling rate of up to 40 MS/s, each. 32 detector channels can be read out per module in this configuration. The module is designed as a mezzanine card, up to four of these cards

¹Sampling ADC

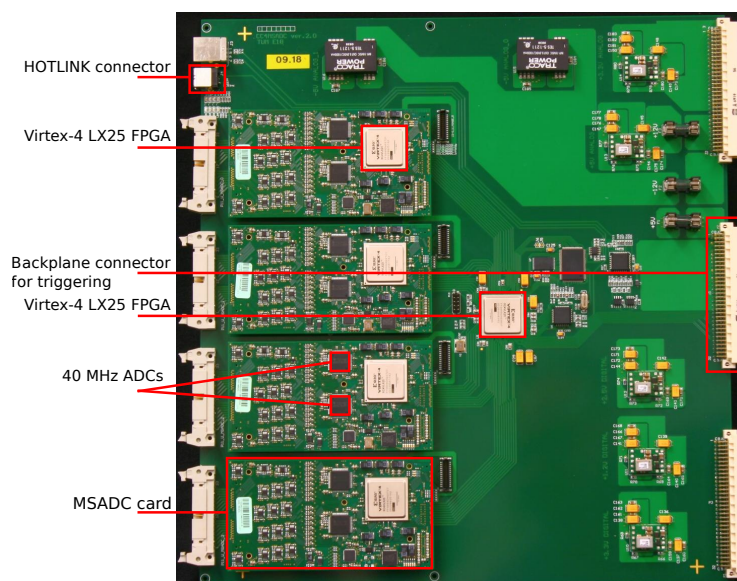


Figure 3.1 Carrier-card with four mezzanine cards, important components are marked in the picture. The module is interfaced to the detector by the four broad connectors on the left.

can be mounted onto one carrier-card designed as a 9U VME board. A photo of the assembled module can be found in fig. 3.1. The carrier-card provides an interface to USB for programming new firmware, to a custom VME backplane as well as to a HOTLink[®] port [59]. This interface is transmitted via an RJ45-cable and provides the TCS¹ information, is used for slow-control and data transfer to the GeSiCA module which connects up to eight carrier-cards. A higher sampling rate is achieved in COMPASS by reading the ADCs in pairs of two, where the clock phase for one chip is shifted by a half clock cycle. This so-called interleaved mode allows a readout with an effective sampling rate of about 80 MS/s. The actual clock frequencies used in COMPASS are not precisely an integer multiple of 40 MHz but are derived from the global clock used in COMPASS of 155.52 MHz [60]. The frequency of this clock is derived from the distances of the particle bunches in the SPS. This leads to frequencies of 155.52 MHz, 77.76 MHz and 38.88 MHz used on the detector. The resolution of each ADC is 12 bit allowing a very precise determination of the signal amplitude.

Because each eight-channel ADC is a physically independent device the baselines are slightly different, having values between 50 and 300 ADC counts. These values can be shifted by setting the operational point of the ADC. This setting is controlled by one digital to analog converter which is common for all ADCs. Shifting the baseline allows covering different ranges of input voltage and thus allows reading signals with different polarities. This feature is not used in COMPASS.

The analog section of the card connects to the detector by pseudo-differential signaling. This means that for each channel the input provides one signal line and a line connected

¹Trigger Control System

to the ground-potential of the signal source. A parallel termination provides an input impedance of $100\ \Omega$ for ECAL0 and $50\ \Omega$ for ECAL2, respectively. The input is then fed into a differential operational amplifier providing the signal for the ADC. In a case when a change from 16-channel readout to 32-channel readout is desired the connection to the ADCs has to be modified using jumper resistors.

The digitized information of the ADCs is further transmitted to a Virtex-4¹ FPGA [61]. The interface is serial for each channel and the data are transmitted over a differential line to the FPGA with a bit rate of 466.56 Mbit/s, the data recovery operates with a serial clock of 233.28 MHz double data rate. The alignment of the bits is done using a frame clock of 38.88 MHz covering one 12 bit data word.

Inside the FPGA, the data is processed for readout. In addition a second processing chain analyzes the data to be further used for triggering, this will be discussed in the next section. The first steps are in common for both chains, here the interleaving of the signal is done by reading the data from the ADCs with 77.76 MHz alternating the readout source in every clock cycle. At this stage one has to be careful that the order of reading is guaranteed. This is done by starting the sequence synchronously with a 38.88 MHz reset signal. If this is not ensured, the timing of the signals may change by one clock cycle of 77.76 MHz every time the readout is restarted depending on the readout source, which is used at start-up, [53].

The second common step is the determination of the baseline which is done taking advantage of the SPS spill cycle which ensures that after a global reset signal no signals arrive for about 1 s. During this time a period of about 12 ms is used to average the signals and thus determine the pedestal values. After determining these numbers they are subtracted from the signal and the average pedestal value is set to a configurable value of 50 ADC counts for readout and to zero for triggering. In case the minimum value of zero is undershot or the maximum value of 4095 ADC counts would be exceeded the sample is fixed to these values. For the data going to the readout the baseline correction can be deactivated and the raw baseline values checked in this way.

After the data are prepared, they are put into a FIFO²-memory which delays the data in order to compensate the latency of the trigger. Typical values for this delay with purely analog triggers are 110 clockcycles corresponding to about $1.4\ \mu\text{s}$ while after introduction of the digital trigger described in this chapter the latency had to be increased to 225 clockcycles corresponding to about $2.9\ \mu\text{s}$.

In the case when a trigger arrives, a configurable number of samples (usually 32) is copied into a second memory. This memory is addressable and is read out sequentially for each detector channel and sample. Taking into account the processing frequency of 77.76 MHz, 16 detector channels and 32 samples per channel, the time which is needed to read out this memory is about $6.51\ \mu\text{s}$, c.f. eq. 3.1. This puts an upper limit to the trigger rate of

¹XC4VLX25-10FF668

²First In – First Out

Table 3.1 ADC Header word

| | | | | | | | | | | | | | | | | | | | | | | | | | | | | | | | |
|----|-----|---------|-----------|-----|----------|------------------|----|----|----|----|----|----|----|----|----|----|----|----|----|----|----|---|---|---|---|---|---|---|---|---|---|
| 1 | EXT | PORT(3) | ADC ID(2) | ERR | Size(12) | Event number(12) | | | | | | | | | | | | | | | | | | | | | | | | | |
| 31 | 30 | 29 | 28 | 27 | 26 | 25 | 24 | 23 | 22 | 21 | 20 | 19 | 18 | 17 | 16 | 15 | 14 | 13 | 12 | 11 | 10 | 9 | 8 | 7 | 6 | 5 | 4 | 3 | 2 | 1 | 0 |

about $151 \times 10^3/s$.

$$(3.1) \quad T_{\text{readout}} = N_{\text{samples}} \cdot N_{\text{channels}} / f_{\text{readout}} = 32 \cdot 16 / 77.76 \text{ MHz} = 6.51 \mu\text{s}$$

Each channel is formatted into 32-bit data words and is read out only if it passes the zero-suppression algorithm. This is done by comparing the maximum and minimum value of all samples, a channel is accepted if this difference is bigger than a configurable threshold.

For each event one header word as well as one start-of-event and one end-of-event word are sent in addition to the data. For each channel one additional header and a number of data words corresponding to half of the number of samples per channel are sent out. Adding up these numbers the number of bytes per event is calculated by

$$(3.2) \quad N_{\text{bytes}} = 4 \cdot (3 + (N_{\text{samples}}/2 + 1) \cdot N_{\text{channels}}).$$

Here N_{channels} corresponds to the number of channels which pass the zero-suppression.

This means for the standard COMPASS configuration 1100 bytes are transmitted per event at most. The interface between mezzanine-card and carrier-card is transmitting one byte per clock cycle of 38.88 MHz. In case of an occupancy of 100% corresponds to a transmission time of $T_{\text{trans}} = 1100 / 38.88 \text{ MHz} = 28.3 \mu\text{s}$ which limits the trigger-rate to $35.4 \times 10^3/s$ in this case.

3.2 The data format

The data are formatted into 32-bit words, most-significant bit first. For one trigger, a header being 32 bit of zeros, precedes the actual information. For each MSADC card the "ADC header" stores global information about the event number as well as the number of 32 bit data words. One special error bit "ERR" indicates problems in the data-processing and thus unreliable data. While the "EXT" bit indicates a different data format which currently is not used and thus this bit is always set to zero. The "ADC ID" is a number from zero to three indicating the mezzanine card where the data originates while the three-bit port number indicates the index of one of the up to eight carrier-cards.

The "Channel header" is transmitted for every channel which passes the zero suppression. It starts with an identifier "01" followed by the four-bit channel number. It continues with one bit set to zero and nine bits which indicate the number of samples recorded

Table 3.2 Channel Header word

| | | | | |
|-------|-------------|----|----------------------------|---------------------------------------|
| 01 | Channel(4) | 0 | Samples(9) | Sum(16) |
| 31 30 | 29 28 27 26 | 25 | 24 23 22 21 20 19 18 17 16 | 15 14 13 12 11 10 9 8 7 6 5 4 3 2 1 0 |

Table 3.3 Data word

| | | | |
|-------|-------------------|-------------------------------------|---------------------------|
| CTRL | SPECIAL(6) | DATA1(12) | DATA0(12) |
| 31 30 | 29 28 27 26 25 24 | 23 22 21 20 19 18 17 16 15 14 13 12 | 11 10 9 8 7 6 5 4 3 2 1 0 |

for this channel. This value is usually set to 32. The last word contains the sum of the amplitudes of all samples.

The actual data start with a two bit control flag which is set to "01" for the first word and to "10" for all following words. The six bits marked as special are not used in the actual data-taking but may contain information for debugging purposes. The last two blocks of 12 bit contain part of actual data consisting of two samples, where the first data word always corresponds to the odd-numbered samples and the second to the even-numbered samples, the first sample has the index zero. Sixteen of these data words are sent out per channel and event.

3.3 The new data format

As calculated in ref. [62] the electromagnetic calorimeters are responsible for about 28% of the data recorded at COMPASS. In order to reduce this, a new data format has been introduced. The format makes use of the fact that most of the channels which are read-out have amplitudes below 63 corresponding to 6 bit. The MSADC FPGA detects these channels and reduces the number of transmitted bits from twelve to six. The values which are stored are the values of each sample where the minimum amplitude is subtracted. This minimal value is stored in the channel header. Reducing the number of transmitted bits allows storing five samples instead of two into each data word which leads to a reduction of stored data-words from 17 to 8. Depending on the amplitude distribution the maximum compression by this approach is a factor 2.125.

The new data format keeps the "ADC header" unchanged while the "Channel header" changes to the following form:

Table 3.4 Channel Header word

| | | | | | | | |
|-------|-------------|----|----|-------------------------|----|----------|---------------------------|
| 01 | Channel(4) | 0 | 1 | Samples(8) | C | 000 | Minimum amplitude(12) |
| 31 30 | 29 28 27 26 | 25 | 24 | 23 22 21 20 19 18 17 16 | 15 | 14 13 12 | 11 10 9 8 7 6 5 4 3 2 1 0 |

Table 3.5 Data word

| CTRL | | DATA4(6) | | | | | | DATA3(6) | | | | | | DATA2(6) | | | | | | DATA1(6) | | | | | | DATA0(6) | | | | | |
|------|----|----------|----|----|----|----|----|----------|----|----|----|----|----|----------|----|----|----|----|----|----------|----|---|---|---|---|----------|---|---|---|---|---|
| 31 | 30 | 29 | 28 | 27 | 26 | 25 | 24 | 23 | 22 | 21 | 20 | 19 | 18 | 17 | 16 | 15 | 14 | 13 | 12 | 11 | 10 | 9 | 8 | 7 | 6 | 5 | 4 | 3 | 2 | 1 | 0 |

Here the maximum number of samples is reduced from 511 to 255 where the now freed bit 24 indicates the new data format. The sum information is removed from the data and its bits are reused. Bit 15 set to one indicates that the data block is read-out in reduced format, while the twelve least-significant bits indicate the minimum amplitude. In case the data is not read-out in reduced format all these bits are set to zero.

The data are stored in the same format as in the old format while only the number of samples in one word increases.

3.4 Trigger strategy

The trigger strategy has to be chosen in a way that the efficiency for the physics, which will be extracted, is optimal. The biggest constraint on the algorithms which can be used in order to make the trigger decision, comes from the fact that in COMPASS a trigger latency of $2\ \mu\text{s}$ should not be exceeded. Due to that, direct triggering on channels containing π^0 s in the final-state is not possible because clustering algorithms would need too much processing time. For that reason, channels which contain more than one neutral particle in the final-state are triggered by calculating the sum of the energy deposited in the central region of ECAL2. The region which is defined as the center is shown in fig. 3.2. The energy of the 12×12 cells, shown in blue, is summed up and compared with a threshold of about 63 GeV. Cells shown in white are not considered, the cells highlighted in orange are excluded because they are close to the beam-hole and consequently suffer from very high background.

In order to be sensitive to the spectrum of single-photon events $\pi^- \text{Ni} \rightarrow \text{Ni} \pi^- \gamma$ down to lower photon energies to extract α_π and β_π separately another trigger is implemented. For that the signal from all 3068 detector cells is transferred to in total 6 trigger-backplane modules. The final trigger decision is made on the central module. In a region, shown in fig. 3.3 in blue, the cell with the highest energy deposition is determined. The region has been chosen in a way that the scattered charged pion is not expected to hit that area while most of the photons end up in this region. This is due to the fact that the track of the scattered pion is bent in the spectrometer magnets. The energy of the photon is estimated by summing a region of 5×5 cells around this cell. The summation region also covers cells, which are not connected to the central module and are close to the boundary. These cells are treated specially. In case the cell with the highest amplitude needs to sum cells from another backplane, the whole adjacent columns are added to the cluster. The cluster energy, determined in this way, is compared to a threshold of 30 GeV. Because the desired

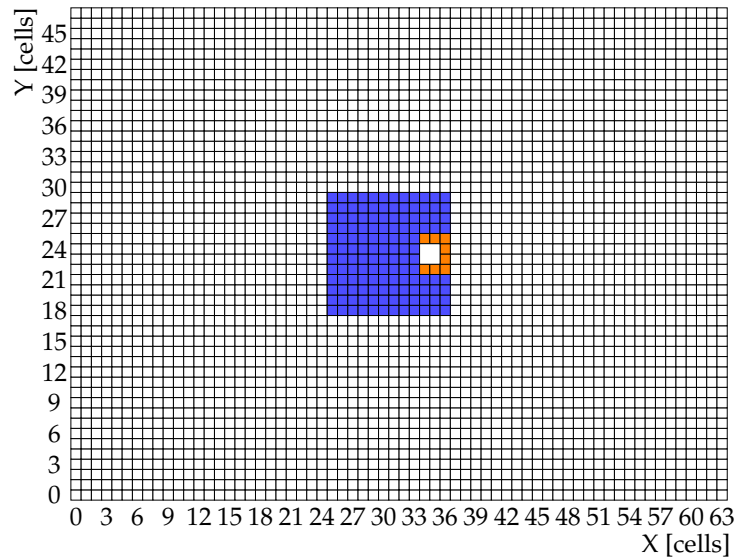


Figure 3.2 Map of selected cells for the summation trigger. The cells depicted in blue are chosen while the cells shown in orange are excluded in order to be less sensitive to elastically scattered beam-particles.

physics-channel has only one photon in the final-state, an additional veto is calculated by summing up all channels, marked blue in fig. 3.4. Cells where charged pions are expected to end up are excluded, again. Further, the energy of the maximum cluster is subtracted from this veto sum. The trigger is vetoed in case the energy in the veto-sum exceeds 18 GeV. This veto threshold is chosen rather high in order to keep some background processes whose contribution needs to be studied.

3.5 Signal detection and feature extraction

In order to perform a trigger decision, the digitized signals have to be analyzed and the important parameters have to be extracted. This is done by means of a digital implementation of a constant-fraction discriminator (CFD). It allows to detect a detector pulse due to the fast rising edge of a signal by comparing the signal to a delayed and scaled copy of itself.

Because all the information, which can be extracted, depends on the signal amplitude, its baseline value has to be extracted beforehand as described in section 3.1.1. For a precise determination of the signal time, it then is subtracted from each sample and thus the signal always starts from zero. This approach has the disadvantage that some samples may be below this calculated baseline. In that case the amplitude of the sample is set to zero and its information can not be used. Mainly this effect happens at the level of noise fluctuations of about 2 ADCcounts and the effect is negligible.

As a next step, the signal is delayed by two clock cycles and amplified by a factor two.

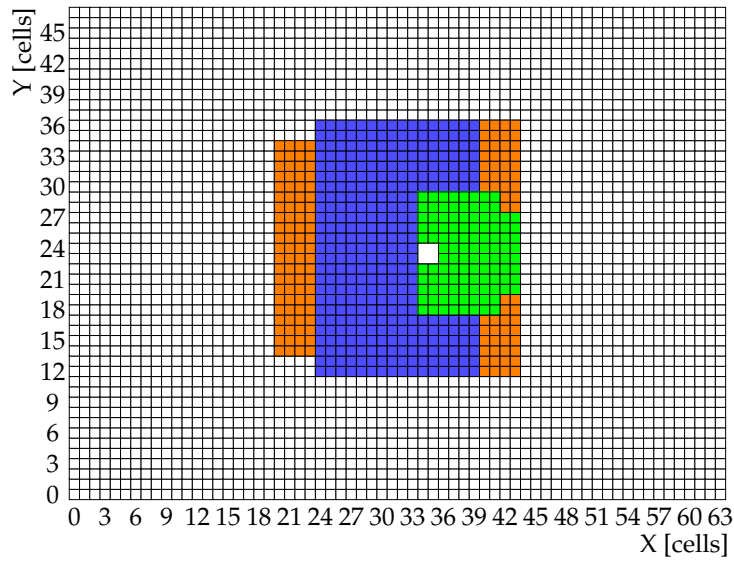


Figure 3.3 Map of selected cells for the maximum cluster trigger. The cells depicted in blue are chosen while the cells shown in orange are used as one combined cell in case the maximum cluster is close to those regions. The cells shown in white and green are not included into the trigger

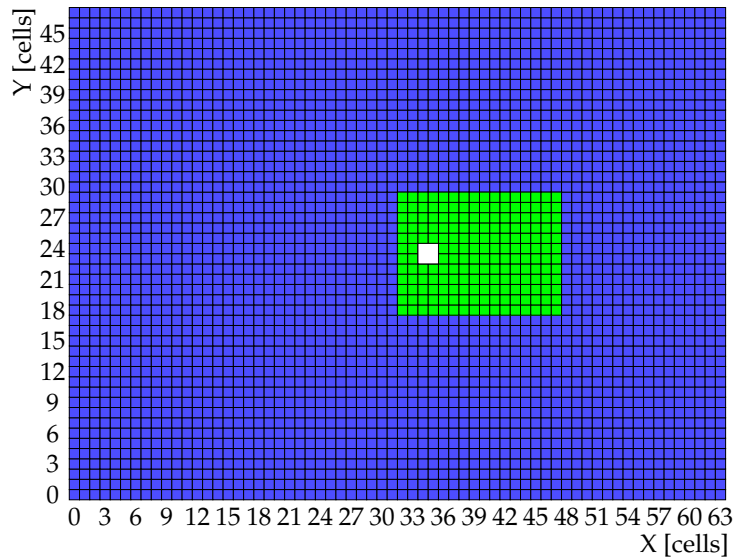


Figure 3.4 Veto region for the single cluster trigger. Events are not triggered if the sum in the blue region is bigger than a given threshold plus the energy of the found cluster.

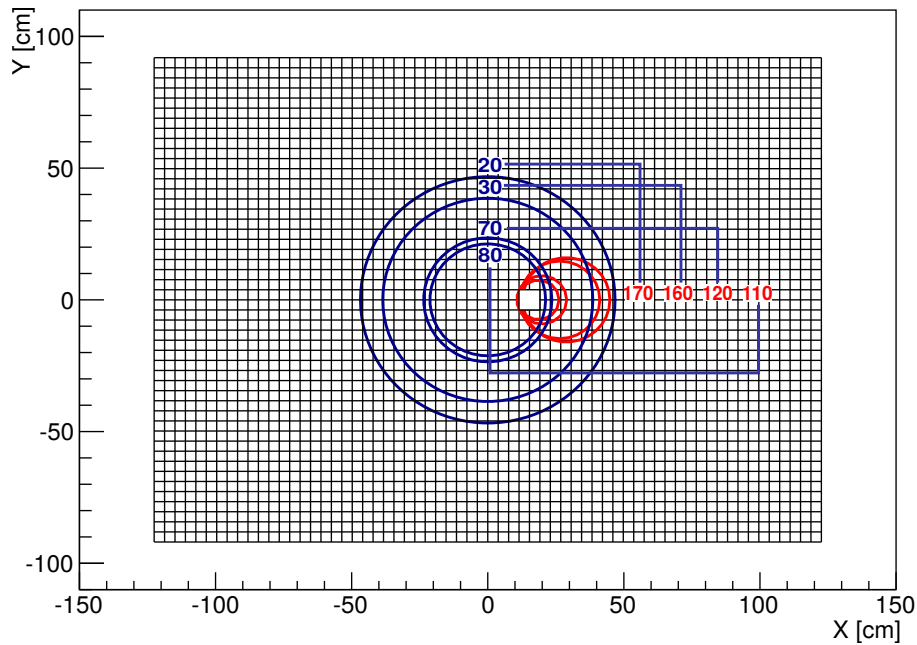


Figure 3.5 Distribution of the positions the final-state particle hits ECAL2 as a function of energy [63]. The photons are shown in blue and the pions in red.

These parameters have been studied in [56] and are optimized for the given signal shape. Further the amplification by two has been chosen because it can be performed efficiently in FPGA by bit shifting. Important here is the length of the rising edge, which is of the order of four to five samples. This corresponds to a time of 50 ns to 65 ns. This delayed amplitude is then subtracted from the original one and its behavior is analyzed. A signal is detected in case this difference is higher than zero in one sample and lower than zero in the next sample. As this behavior may also be induced by noise, a threshold to the difference of these two consecutive values of about 1 GeV is applied. This corresponds to about 20 ADCcounts for the central modules. In fig. 3.6 the algorithm is sketched for an exemplary event.

In order to extract the amplitude of the signal the maximum of the pulse has to be determined. In fig. 3.7(a) can be seen that the amplitude at the sampling point of the CFD does not correspond to the maximum of the pulse which gets even more obvious in fig. 3.7(b) where the amplitude is shown as a function of the relative difference to the maximum. One can see that the error ranges up to 16 % for high amplitudes while it is even stronger for amplitudes below 100 ADCcounts, originating in the general loss of precision in this range. In order to compensate this effect, the algorithm extracts the amplitude of the signal by scanning the next three samples, after the detection of the signal, for the maximum value. The amplitude corresponds to the uncalibrated energy deposited within one detector cell.

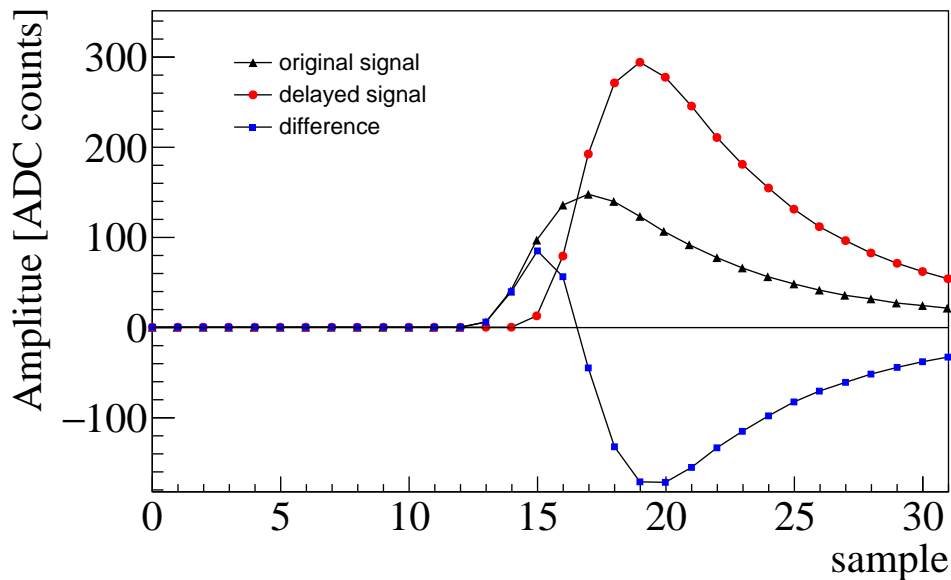


Figure 3.6 Illustration of the implementation of the CFD algorithm. The signal coming from the detector (black triangles) is delayed by two clock cycles and amplified by a factor two (red circles). The difference between these two signals shown as blue squares is used to detect the signal.

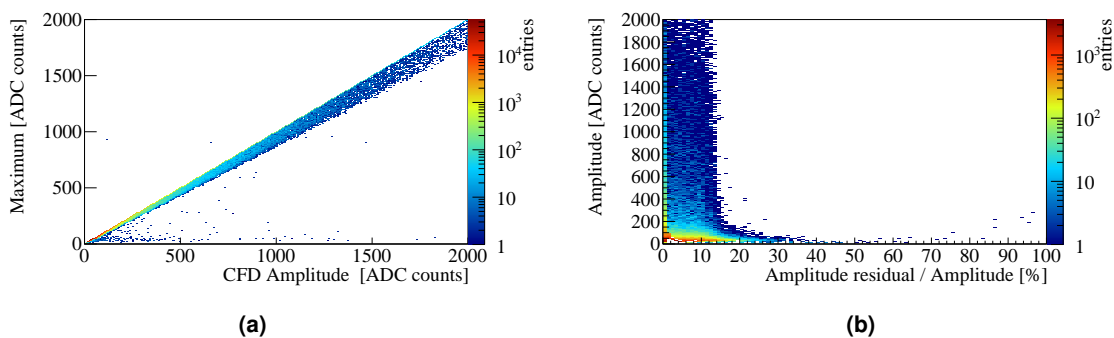


Figure 3.7 Maximum value of one pulse as a function of the amplitude determined at the CFD sampling point (a). It can be seen that the amplitude determined with the second approach is in the range of 84% to 100% of the maximum. In (b) a similar picture can be seen, here the amplitude is plotted as a function of the relative distance to the maximum. Again a maximum deviation of 16% can be seen. For small amplitudes the deviation is larger.

The time of the signal is roughly determined by the last sample before the signal is detected. Looking at the shape in fig. 3.6 it can be assumed to be linear at the point where the signal is detected. Moreover, one may extract the exact time when the zero-crossing occurs. This is done by linear interpolation to this point by taking into account the difference before and after the zero-crossing point

$$(3.3) \quad t = \frac{T}{A_i - A_{i+1}} \cdot A_i$$

where T is the distance between two samples corresponding to one clock cycle of 12.86 ns and A_i is the amplitude of the corresponding sample. Using this approach a time resolution of 1.1 ns is achieved [56]. This can be seen in fig. 3.8 (a) where a fit to the distribution, using a double-gaussian, yields this resolution.

In hardware, it is impossible to implement the division required in eq. 3.3 with a good resolution and a fast processing speed by means of logic. Thus, the division is approximated by implementing it using a lookup-table for every channel. Because this further means to store many numbers, the range of input numbers is reduced by only considering the six most-significant bits on the input. This reflects in the finally achieved time-resolution as can be seen from fig. 3.8 (b), where the difference between the time calculated with full precision and the implementation using the lookup-table can be seen.

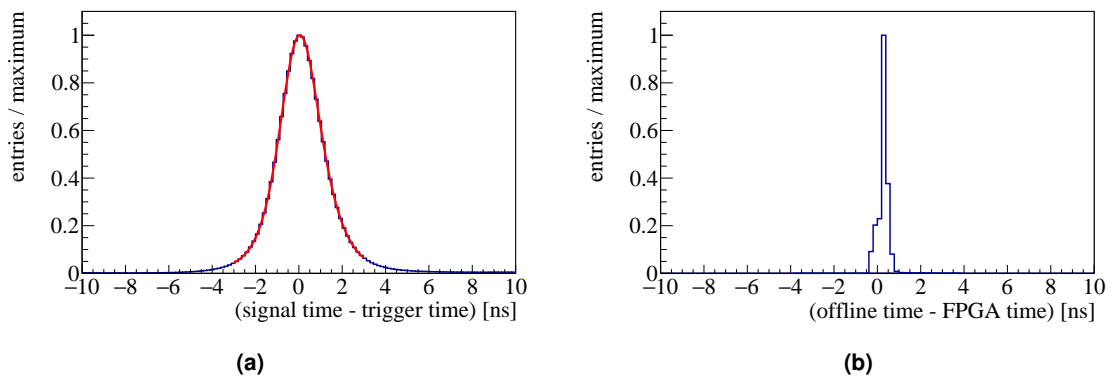


Figure 3.8 Time resolution of the CFD algorithm. In (a) the full resolution achieved by the CFD is shown by plotting the difference between trigger time and the time given by the CFD. The time is extracted by linear interpolation and the full amplitude information is used. A resolution of 1.1 ns is extracted using a fit of a double-gaussian to the distribution and taking the weighted mean of both resolutions. The fit is parametrized by $0.51 \cdot \exp \left[\left(\frac{x - 0.17}{1.26} \right)^2 \right] + 0.49 \cdot \exp \left[\left(\frac{x - 0.01}{0.73} \right)^2 \right]$. In (b) the difference between the time extracted using the full information and the time determined by using the lookup-table for the division is shown. As can be seen, the effect of using a lookup-table is much smaller than the actual width of the time-resolution.

3.6 Time and energy calibration

After having extracted the time and amplitude of a detector pulse, this information has to be calibrated in order to do further calculations. Both calibration constants are stored in a database and are loaded to the MSADC-FPGA, the process is described in section 3.12.

The time calibration is stored as a 12 bit value where the six most-significant bits represent the offset in units of one clock cycle, also referred as coarse-time. The time covered by this value is $64 \cdot 12.86 \text{ ns} = 823.04 \text{ ns}$ this is more than required by the maximum deviation between individual cells, which is less than 100 ns. The six least-significant bits represent the offset in fractions of $1/64$ of one clock cycle, also referred as fine-time. The fine-time is added to the measured time and in case this sum adds up to more than one clock cycle the signal is delayed by one clock cycle. In addition to that a FIFO-like memory is used to further delay the signal by the coarse-time value.

The energy calibration is a 10 bit value representing the calibration coefficient obtained by the calibration with an electron beam, described in section 2.4.1 and thus does not reflect the π^0 -calibration constants or time dependent calibrations which are not yet available at this time. Its range is chosen in a way that the trigger operates at the best resolution and thus has a dynamic range only up to 100 GeV, because all thresholds are smaller than this value. These coefficients are multiplied to the measured amplitude and the result is further processed as a 12 bit value.

3.7 Interface to the carrier-card

In total 8 data lanes are available between each mezzanine-card and the carrier-card, these have to be shared with the readout. For the readout 1 byte has to be transferred in one clock cycle of 38.88 MHz, this means that the interface speed has to be increased for the use of the trigger.

3.7.1 2009 setup

For the year 2009 a simple trigger scheme was used where only the total energy sum of selected channels is considered. In this case it is sufficient to transmit the energy sum of all channels of one MSADC, already available at this point, to the further stages. In order to get a good overlap of all signals, each value added to the sum is used in two consecutive clock cycles. This is needed in case the time determination, which determines the corresponding clock cycle, is close to the next clock cycle. After summing all 16 channels on one MSADC, the result has a maximum width of 16 bit which then have to be transferred to the carrier-card. A value with more than the 12 least-significant bits unequal to zero indicates a summed amplitude exceeding the dynamic range. This allows transferring only the 12 least-significant bits, but setting them all to one in this case. During the

Table 3.6 Idle data

| | |
|---|---------------|
| 01 | Timestamp(26) |
| 27 26 25 24 23 22 21 20 19 18 17 16 15 14 13 12 11 10 9 8 7 6 5 4 3 2 1 0 | |

preparation for data taking in the year 2009 an interface speed of 155.52 MHz has been achieved. This allowed using 2 data lanes for data-taking and 6 data lanes for the trigger interface. Thus, the required information was transferred with 6 bit in each clock cycle of 155.52 MHz.

3.7.2 2012 setup

The upgraded trigger for 2012 makes it necessary to transfer more information than just the sum. By switching the interface to double data-rate it is possible to transfer data with 311.04 MHz. This allows using only one data lane for data-taking and having 7 data lanes available for the trigger interface and transferring 28 bits with each clock cycle of 77.76 MHz which is used to transfer the information for one channel with a detected signal.

The delay, which would result from this sequential data transmission, is up to 16 clock cycles and thus would already add more than 200 ns to the total latency. In order to reduce this delay not all 16 channels are handled independently but pairs of channels are considered as meta-channels, for which only the combined information is transferred. This combined data is determined by setting the amplitude to the sum of both channels while the time slice is always determined by the channel with the higher amplitude.

These data are multiplexed in order to be transferred further, sequentially. This is done by storing the energy parallel for all channels into a dual-ported memory which has a data width for reading which is eight times smaller than for writing. Now, each channel which has a non-zero amplitude is read out sequentially, starting from the earliest hit which has been detected. In addition, the time stamp is stored for every hit. This time stamp is compared with a global time stamp and in case the difference exceeds 9 clock cycles a truncate bit (T) is set. This bit indicates that not all data can be transferred within the desired latency budget. In case this happens the algorithm starts to send data belonging to the next clock cycle. Further it is desired to trigger every event where this happens because the trigger decision is not clear in this case.

In case no hit is found in the card at a given time, an idle word consisting of the two most-significant bits set to "01" is sent where the remaining bits are set to the current time stamp. This is used in order to check that all cards operate synchronously up to the backplanes.

When a hit is found, the most-significant bit is "1". The second most-significant bit is used to indicate truncation happening in this time-slice. Further, for each channel its ID

Table 3.7 Hit data from the MSADC

| | | | | | | | | | | | | | | | | | | | | | | | | | | | |
|----|----|----------|----|------------|----|----|----|----|----|----|----|----|----|----|----|---------------|----|---|---|---|---|---|---|---|---|---|---|
| 1 | T | Chan.(3) | 0 | Energy(12) | | | | | | | | | | | | Timestamp(10) | | | | | | | | | | | |
| 27 | 26 | 25 | 24 | 23 | 22 | 21 | 20 | 19 | 18 | 17 | 16 | 15 | 14 | 13 | 12 | 11 | 10 | 9 | 8 | 7 | 6 | 5 | 4 | 3 | 2 | 1 | 0 |

is transferred followed by its amplitude and the time stamp to which this hit belongs. The data format is shown in table 3.6 and table 3.7.

3.8 Interface to the backplane

The interface to the backplane card is sending its data via P2¹ with connector through the VME backplane. As this connection is not designed for high speed data transmission, a maximum frequency is limited to 77.76 MHz.

3.8.1 2009 setup

As only the total energy sum is relevant for the trigger concept, on the carrier-card the summation of the already summed signals of each of the four mezzanine cards is performed. Out of this information the nine most-significant bits are used and sent to the backplane. Here, the signals from all eight connected carrier-cards is calculated and compared with a configurable threshold. If the signal amplitude is higher than the threshold, a trigger signal is sent out.

3.8.2 2012 setup

To include the full detector into the trigger, six backplane modules are used, the arrangement is shown in fig. 3.9.

The extended information from the mezzanine cards also requires a more complex handling of these data. The new backplane card can be interfaced by 35 bit where one of these bits is required to transfer the synchronous reference clock. The data is transferred in two streams with a width of 34 bit, each. Both streams contain the multiplexed data from two out of the four mezzanine cards. In the multiplexing step it is ensured that no data signals which are older than 11 clockcycles are transferred to the backplane. The 11 clockcycles are chosen, because they account for one event where the two neighboring MSADCs have a combined occupancy of 75 %. In case the 11 clockcycles are reached, the next signal will be marked as truncated and all further signals belonging to this time-slice will be skipped. Because the amount of data belonging to one time-slice for one mezzanine card is random, the time-ordering of the data is not predictable. In order to

¹A 9U VME backplane has three connectors with 96 pins each, they are labeled P1, P2, P3.

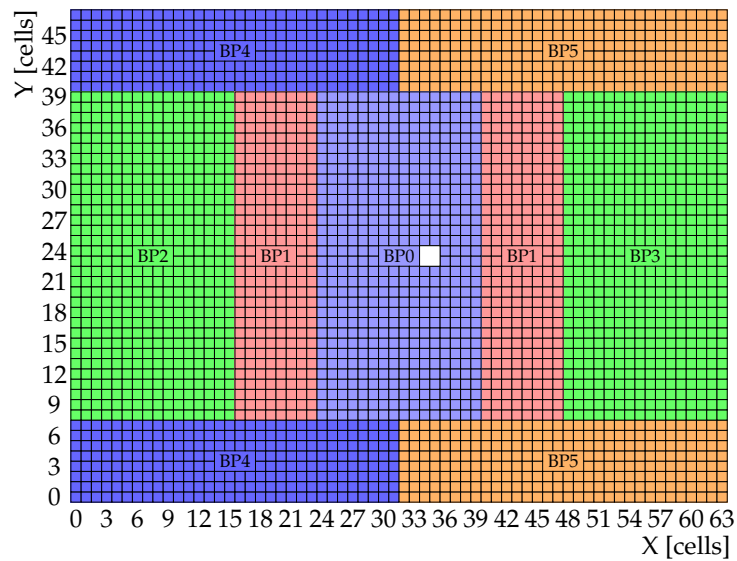


Figure 3.9 Map of how the backplane modules are connected to ECAL2. BP0 is the most central module on which the trigger decision is taken.

Table 3.8 Hit data from the carrier-card

| Energy(9) | | | | | | | | | MS | Chan.(3) | | | Timestamp(4) | | | |
|-----------|----|----|----|----|----|----|---|---|----|----------|---|---|--------------|---|---|---|
| 16 | 15 | 14 | 13 | 12 | 11 | 10 | 9 | 8 | 7 | 6 | 5 | 4 | 3 | 2 | 1 | 0 |

circumvent this, the carrier-card FPGA is ordering the data in time. The data format is given in table 3.8.

The energy used here is selected from the most-significant bits of the MSADC and the data-source is indicated by the "MS"-bit, c.f. table 3.8. The channel number and the time stamp have the same meaning as before, c.f. table 3.7. In case no data is provided by the mezzanine card all data except the time stamp is set to zero while truncation is indicated by setting the channel number to one.

3.9 The 2012 backplane card

The backplane used in 2012 is shown in fig. 3.10 is based on a Virtex-6¹ FPGA. This chip was selected because it is the smallest and most modern FPGA at the development time, which provides enough IO-pins for interfacing to all carrier-cards, and because it offers eight high-speed transceivers of which up to six are used. The backplane was designed together with Igor Konorov.

One carrier-card is directly connected to the VME backplane. For the remaining seven cards an interface via flat-cables and an adapter PCB is set up. This is a more desirable

¹XC6VLX125T-2FF1156

way of connecting the card because a direct connection per VME connector requires an installation force corresponding to 200 N, parallel to the direction of installation, per connection. This puts a lot of stress to the PCB during the installation.

The binary trigger decision is sent via LEMO cables to the crate in which the coincidence with the other trigger signals is made. Four of these connectors are available, this puts a limit to the number of different triggers which can be provided. The further transmission is then performed by coaxial cables of 30 m length. In order to reduce the signal-loss over this distance the cables are chosen to have a diameter of 2 cm which is thick compared to a LEMO cable with a diameter of 2.8 mm.

The connection to the slow-control readout process, c.f. section 3.12, is done via Ethernet. For this an RJ-45 connector with a separate physical-layer chip is installed. Because the development of Ethernet logic for the Belle II readout [?] showed that it is more convenient to use an Ethernet adapter which can be plugged into an SFP¹ cage, the development of the interface to this chip has not been continued.

One single SFP-cage is installed, which is used for connection to the TCS system. This data is provided by an optical fiber, layed to the calorimeter. Because all six backplane modules would need an individual optical fiber, a local fan-out module based on the GeSiCA provides the data to all FPGAs. Data and clock provided by the TCS are decoded by an additional chip and then provided to the FPGA.

The 4x2 SFP cage is used to connect five backplane cards to one central module by five optical fibers, described in section 3.10. One additional slot is used by the GLC-T-C [64] SFP to Ethernet adapter providing slow-control information. Two ports are currently not used.

3.10 High speed interface between the backplane cards

For the transmission of data between the different backplane cards a 4 Gbit/s serial interface is used, the cards are interconnected by optical fibers. In order to fix the link latency to a predetermined value, the buffers inside the Virtex-6 high-speed transceivers have been bypassed [65]. This requires special care in selecting the logic elements inside the FPGA, because there are not sufficient clock buffers² available which are needed to implement six transceivers in this mode, so in addition more complex clock-managing modules need to be used.

All data which have to be transfered via the optical link are synchronous to 77.76 MHz, half of the COMPASS TCS clock [60], while the interface clock is asynchronously running at 250 MHz. In order to achieve synchronous data the data words with a length of 48 bit is written to two different registers in an alternating way and the update of the registers is indicated by a toggling bit. In case one word is changing the other word is read by

¹Small Form-factor Pluggable

²A clock buffer is required to distribute the clock inside the FPGA.

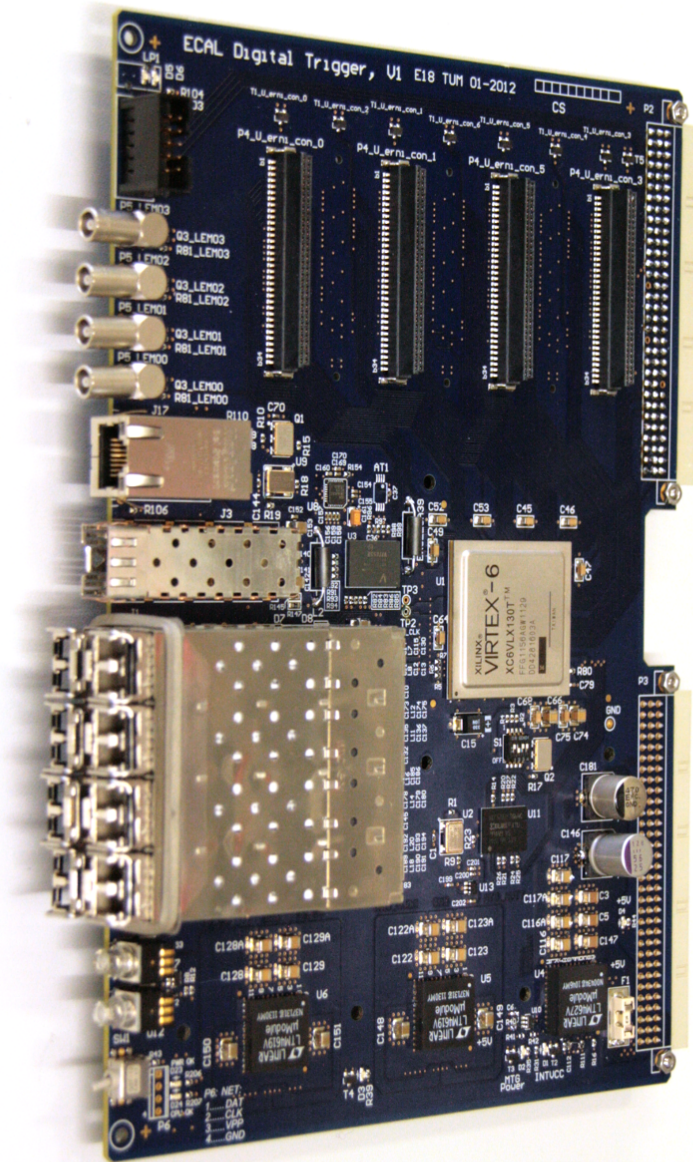


Figure 3.10 The backplane card used in 2009. On top the connectors to the carrier-cards are shown. On the left top the LEMO outputs providing the trigger signals are placed. Below the not used Ethernet connector is placed above the TCS receiver. On the bottom the 2x4 SFP cage provides the high-speed serial links. All data are processed by the Virtex-6 FPGA in the center.

the 250 MHz clock and further transferred to the optical interface, split into three words of 16 bit, each. Since the difference between the two clocks is not a factor of three, two control bytes "0x7CBC" are inserted into the data stream in case it is needed. A data flow of this transmission can be found in fig. 3.11. On the receiver side the control words are ignored and the remaining received words are reassembled to a length of 48 bit. Then the same as on the transmitter side is applied in order to go back to the 77.76 MHz clock domain. This manual procedure of clock domain crossing is needed because synchronizing with a FIFO for instance would result in a non-deterministic latency.

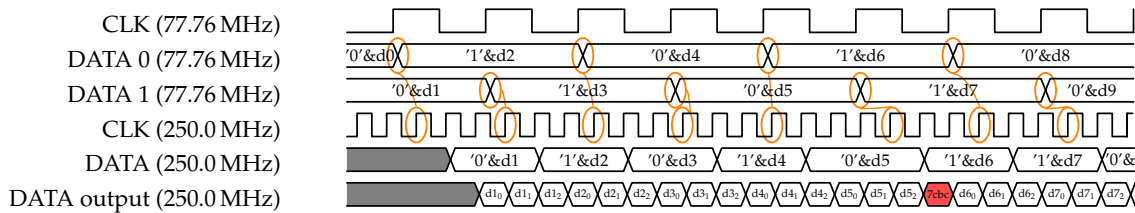


Figure 3.11 Transition from the 77.76 MHz clock domain to the 250 MHz clock domain. The transitions are detected on the rising edge of the faster clock (orange symbols) which trigger a transmission of the other data word. In case an expected transition is not found, a dummy word 0x"7cbc" is inserted (highlighted in red). The data words d0 to are 48 bit wide while the words which have an additional index have a reduced width of 16 bit.

In order to monitor the stability of the interface, pseudo-random numbers are generated by a linear-feedback shift-register described by the equations [66]

$$(3.4) \quad D(0) = D(46) \text{ xor } D(45) \text{ xor } D(26) \text{ xor } D(25)$$

$$(3.5) \quad D(1 \dots 46) = D(0 \dots 45)$$

and checked on the receiver side, as initial value all bits are set to one. This is done at the end of every spill. In case an error occurs it is counted and the number of errors is sent to the slow-control interface of the backplane.

3.11 Implementation on the backplane

Summing in selected region is performed using the following algorithm. The algorithm takes advantage of the fact that the data from each carrier-card comes sequentially for each detector-channel. First it is checked if the channel containing the data is included in the channel mask for the selected operation, only then the channel is considered. The next step is to check the bit of the data, which indicates if truncation happened. This is always the case, when the data of one carrier-card could not be transmitted due to a transmission time bigger than 187.5 ns for all hits corresponding to one event. In this case

the trigger is always giving a signal independent of result of the calculation. This is done to avoid inefficiency.

The main algorithm is based on a dual-ported memory where the final output is read from port B. Here the reading is done in a circular way with some delay. Port A is used for reading and writing, the address is calculated from the difference of a given local timestamp and the timestamp of the incoming signal. In case the address does not change from one signal to another, the entry in the memory belongs to the same event and the sum of both is stored. In case the address changes, the information from the data stream is taken. The value which is read from port B is valid for all eight connected carrier-cards at the same time with a fixed latency. The information is processed further, in a tree-like procedure. The algorithm is sketched in fig. 3.12.

The result of the summation is compared with a programmable threshold and gives a trigger signal in case the threshold is exceeded.

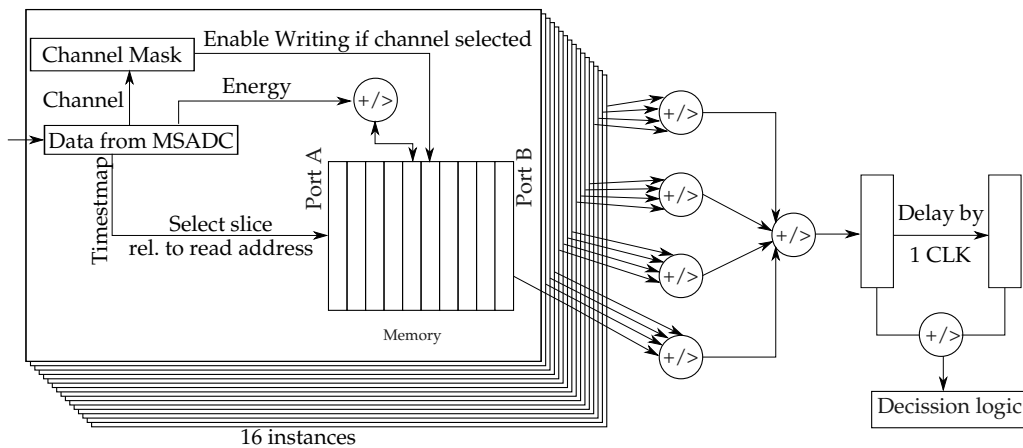


Figure 3.12 Data flow for the processing on the backplane card.

The search for the maximum cluster is performed using a similar algorithm as for the summation. The only difference is that mathematical operation "+" is replaced with the comparison ">" and the found maximum is stored in all steps instead of the sum.

The sum around the calculated cell has to be calculated in an additional step. In order to do so the data for all channels belonging to one event are timed in and stored into a matrix, where the two indices correspond to the cell position. As a next step a mask is applied to the channels which have a distance bigger than two in y-direction to the maximum cell, setting their amplitudes to zero. After this, a column-wise summation is performed. As a last step a mask is applied again, now in x-direction, and a row-wise summation is performed.

In order to increase the size of the trigger area, two bands on the left and on the right of the central module are taken into account. In case the maximum cell is close to the border of the central module or the energy of one of these bands is bigger than the energy of the maximum cluster the cell of the side-band is added to the maximum cluster. The trigger

gives a signal in case this sum is bigger than a given threshold and in case the sum inside the veto region is smaller than a given veto threshold.

3.12 Slow-control

The slow-control is split into two parts, part one is the control of the MSADC cards. This is done via the config-server [67], a software running on computers connected to the VME interface. It allows to set the threshold for the amplitude detection as well as parameters for time and energy calibration for each individual detector channel. Since this interface automatically sends a reset signal¹ to the FPGA, it was not possible to monitor any parameters on the MSADCs.

The second part is the interface to the backplane card, this was implemented using a direct Ethernet connection to the backplane. For this a MicroBlaze soft-core CPU [68] was implemented in the FPGA and a TCP/IP client was implemented in this soft processor. The implementation such a CPU requires a significant amount of the FPGA-resources, especially memory. It can not be recommended for future use for this kind of applications because it limits the remaining logic. Via this interface the thresholds for every trigger type and every veto can be set as well as the corresponding trigger regions. For the monitoring, a TCS receiver is connected to the backplane card which provides information about the end of each spill. As soon as the end-of-spill signal is received the TCP/IP client connects to a server running on a computer and provides monitoring information. These values are further stored into a MySQL-database. The monitoring parameters are:

- Error counters for the interface to each carrier-card
- Error counters for each high-speed interface
- Hit counters for every channel
- Hit counters for every trigger, how often the threshold was exceeded.

For monitoring, the COMPASS Detector Control System(DCS) [44] is used fig. 3.13 and provides graphical access to all the parameters. For better visualization the hit counters are normalized to the beam intensity. An alarm is raised when the hit counters exceed a threshold which is set to 50 % around a defined nominal value or the error counters are not zero.

3.13 Commissioning of the trigger

After all modules of the trigger are installed and all calibrations are prepared, the setup has to be verified for functionality.

¹This is an unavoidable feature of the implementation



Figure 3.13 The DCS window for the ECAL2 trigger monitoring. On top a map of all cells is shown where green cells mean the hit counters are within the limits. Cells marked in orange exceed the limits by more than 20% and red cells by more than 50%. The vertical red band indicates a problem with one of the carrier-cards. On the right the statistics of all cells is shown. On the bottom the rates for each trigger are shown and on the very bottom the error counters for each interface. Here the value for module 617 is not zero and indicates an error.

The first step in this procedure is to check that the energy calibration is correctly applied and its coefficients correspond to the desired values in energy. In order to do this the electron beam which is also used for calibration is directed to one cell of the detector at three different energies: 15 GeV, 30 GeV and 40 GeV. For these energies the trigger threshold is varied in steps of 1 GeV and the number of events which are triggered within one spill are measured. Fig. 3.14 shows that the number of recorded events drops when the threshold exceeds the average energy of the beam. It has to be stated that the width of the falling edge does not indicate the resolution of the trigger because it is convoluted with the energy spread of the beam. For electrons this width is not known but expected to be in the order of several GeV due to Bremsstrahlung losses.

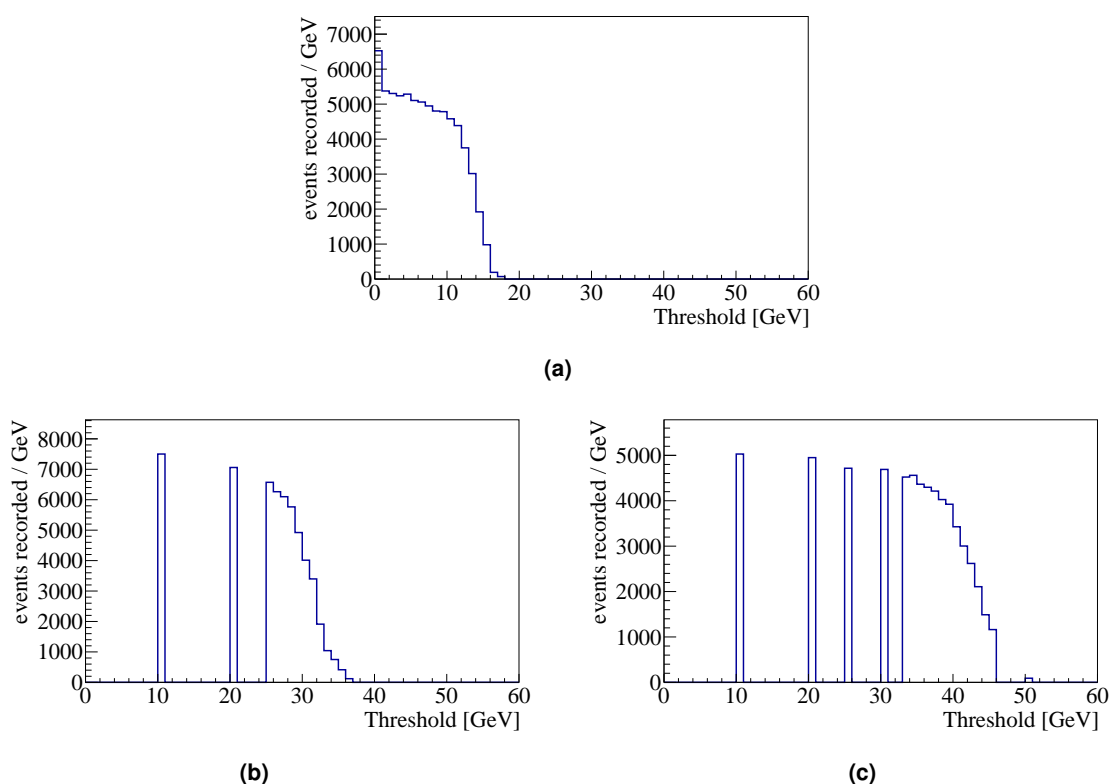


Figure 3.14 Threshold scan of the ECAL-trigger with an electron beam of three different energies: 15 GeV (a), 30 GeV (b) and 40 GeV (c). For each threshold the number of triggered events in one spill is shown which decreases as soon as the threshold exceeds the average beam energy. In case the plots indicate zero events the measurement was not performed at that threshold.

As a next step, the mapping of the channels in the trigger to the physical cells has to be verified. This is done by using an electron beam with an energy of 30 GeV is used while the threshold is set to a significantly smaller value of 20 GeV. The detector is moved in a way that the beam is focused on a certain cell of the detector and only this cell is activated in the trigger. A scan in two lines, one horizontal and one vertical, showed that the mapping is correct except the vertical numbering had to be mirrored, see fig. 3.15.

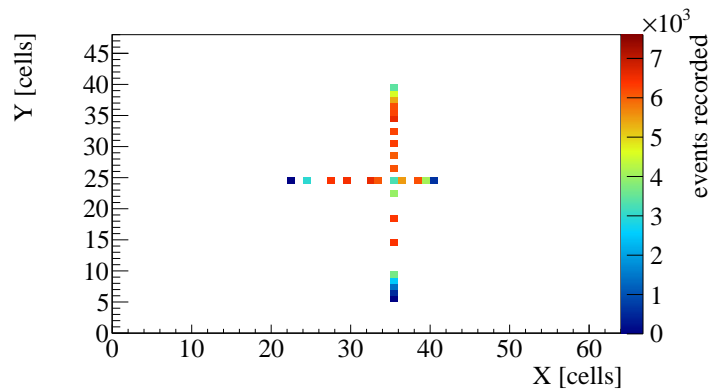


Figure 3.15 Scan of the mapping of the ECAL trigger. An electron-beam is focused on one cell of ECAL2 and only this cell is activated in the trigger. Enabling only this cell in the trigger is used for verifying the mapping by showing the pattern of the detector movement. The variation in intensity is due to a different movement speed of the detector.

As the last step, the time calibration has been checked by comparing the relative position of the beam trigger to the pulse from the calorimeter when changing the time calibration values. This has been done manually by checking the signals with an oscilloscope. The required cabling has been performed by [69]. Further the pulse from the calorimeter has to be timed in, such that it provides a coincidence window for the beam trigger. Due to the fact that the trigger comes asynchronous to the physical event, but synchronous to a clock with a frequency of 38.88 MHz, the time gate has to be chosen with a width of at least twice the period length of the clock being 25.72 ns. Looking at the trigger time relative to the trigger clock (referred as TCS phase) as a function of the trigger time, fig. 3.16. for different widths of the gate shows the influence of the width of the gate. The red, vertical band corresponds to events where the calorimeter signal coincides to the time of the beam trigger while the triangular structures stem from pile-up. In case the time-gate is chosen to be too narrow, fig. 3.16 (a), part of the correct events are removed from the event leading to a drop in efficiency, while a gate being too wide allows for more pile-up fig. 3.16 (b). The optimum time gate is found with 42 ns fig. 3.16 (c).

3.14 Elements in the trigger

In addition to the calorimeter trigger several other detectors contribute to the trigger decision. They are either put in coincidence with other elements or may be contribute independently.

The basic element for all physics triggers is the so-called alternative beam-trigger. It is a coincidence between the signals of FI01X and the beam counter which is a 32 mm diameter scintillator disc located downstream of FI01. This element defines the beam and gives a fast pulse in case a beam-particle is detected.

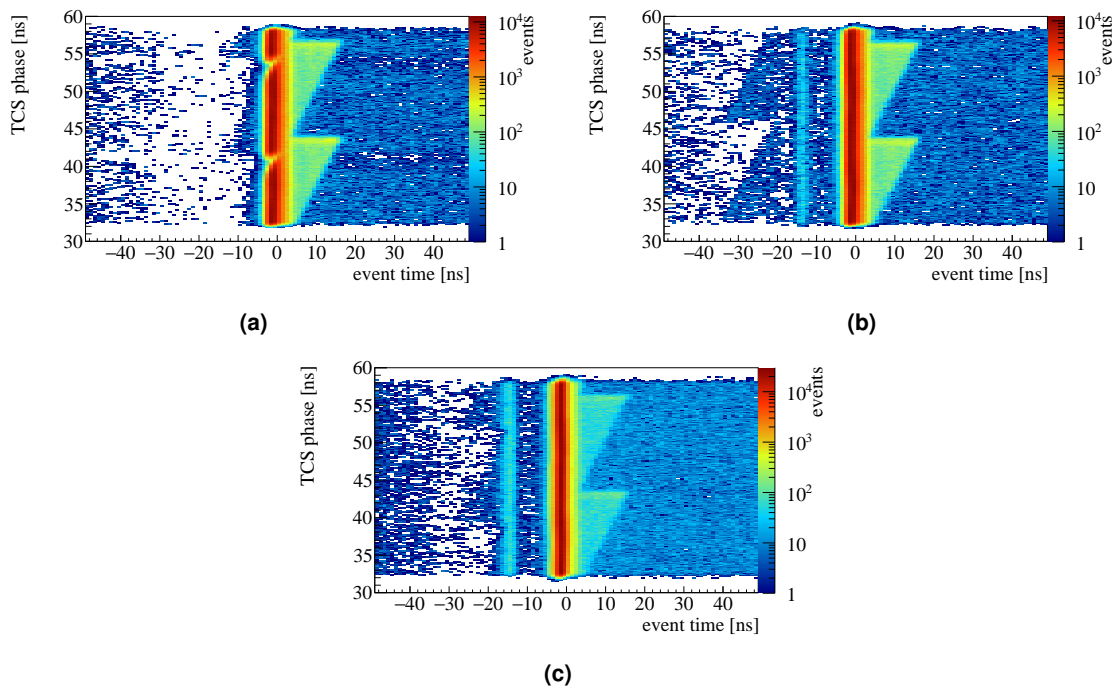


Figure 3.16 Trigger time as a function of the TCS phase for different trigger time gates. The events where the calorimeter-trigger matches the beam-trigger are indicated by a vertical, red band while the triangular shapes indicate pile-up. A gate of 26 ns is too narrow and part of the interesting events are cut away (a). A gate of 48 ns is too big and allows for too much pile-up (b). A time gate of 42 ns is chosen to allow a relatively low amount of pile-up (c).

In addition, a veto system is used. A system of hodoscopes is used to veto particles stemming from the beam halo not pointing to the target. Further the sandwich veto is installed downstream of the target, it is a calorimeter-like detector which vetoes events which contain particles outside of the spectrometer acceptance. The last veto element are the beam killers which are two scintillator discs in the region between SM2 and ECAL2 which veto non-interacting beam particles. The combination of beam trigger and veto system is called the minimum-bias trigger.

The Primakoff triggers are set up as a coincidence between the signals from the ECAL2 trigger and the minimum bias trigger. In contrast to other triggers the beam killers are not included in this trigger, because they only lead to a small reduction of the trigger rate [69] while they might have systematic effects [70] depending on the momentum of the charged particle in the selected data. The final setting in 2012 is:

- "Primakoff 1" (P1): Total energy deposit of more than 63 GeV in the central region
- "Primakoff 2" (P2): A single cluster with more than 30 GeV, veto threshold 18 GeV
- "Primakoff 3" (P3): Varying settings, for debugging only

An additional trigger which was used in 2012 is a so-called low-t trigger, which triggers on the number of charged particles in the final state. It consists of a square scintillator with a base length of 6 cm with plastic light guides and two PMTs, fig. 3.17, and is installed about one meter downstream of the target. The charged-particle multiplicity is determined by selecting events where the measured energy loss is higher than the one of two minimum-ionizing particles. This detector was not installed during the whole period of data-taking. Its impact has to be studied.

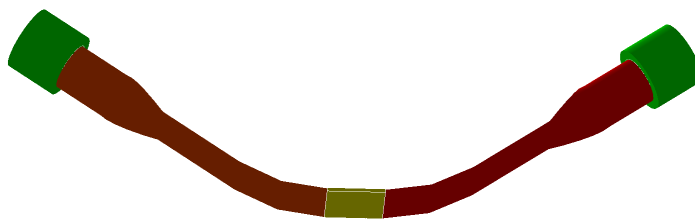


Figure 3.17 Drawing of the multiplicity counter as it is implemented in Monte Carlo description of the 2012 setup. The scintillator is shown in yellow, the light-guides in red and the PMTs in green.

The kaon trigger is a modified version of the minimum bias trigger where in addition the beam PID is determined, this is done by requiring that at least one of the two CEDAR detectors has a signal in more than 6 PMTs. This trigger may be used to study reactions induced by kaons in case these reactions are not triggered by any other element. In case

Table 3.9 Trigger rates for all triggers for one exemplary run taken with a hadron beam. The prescaling gives the fraction of trigger attempts which will be propagated to the DAQ. It corresponds to the ratio of trigger attempts to accepted triggers. The numbers are given as number of triggers within one spill.

| Trigger name | prescaling | trigger attempts | accepted triggers |
|--------------------------|------------|------------------|-------------------|
| Low-t trigger | 14 | 923097 | 65936 |
| Primakoff 1 | 1 | 216729 | 216729 |
| Primakoff 2 | 2 | 417135 | 208568 |
| Primakoff 3 | 20 | 661270 | 33064 |
| Minimum Bias Trigger | 160 | 5403032 | 33769 |
| Inner Veto | 500 | 1564387 | 3129 |
| Halo Trigger | 150 | 607591 | 4051 |
| Beam Trigger | 2800 | 26209313 | 9361 |
| alternative Beam Trigger | 2800 | 23505500 | 8395 |
| Kaon Trigger | 1 | 76488 | 76488 |
| True Random | 1 | 22311 | 22311 |

this trigger is used, the phase space of the Kaons in the beam is reduced as described in section 5.1.

The inner veto trigger as well as the halo trigger consist of the veto elements in the trigger and may be used to study systematic effects. In addition, they cover beam particles with a huge kinematic spread and thus are used for the alignment of the spectrometer components.

The true random trigger is based on the decay of a radioactive source. In case a particle from the decay is detected a trigger is issued to the experiment. This trigger is also used for systematic studies.

An exemplary list with rates of all triggers as they occurred during the running can be found in table 3.9 for data collected with hadron beam and in table 3.10 for data collected with muon beam.

3.15 Tuning the thresholds

The maximum trigger rate which can be accepted by the COMPASS DAQ and front-ends is in the order of 30×10^3 persecond corresponding to 300×10^3 perspill. In order to fulfil this requirement the trigger setting has to be tuned. This can be done by only accepting a certain fraction of the attempted triggers (prescaling factor) or by tuning the parameters of the individual triggers.

In the case of the Primakoff triggers, this tuning can be performed by changing the thresh-

Table 3.10 Trigger rates for all triggers for one exemplary run taken using a muon beam. As in table 3.9.

| Trigger name | prescaling | trigger attempts | accepted triggers |
|--------------------------|------------|------------------|-------------------|
| Low-t trigger | 14 | 0 | 0 |
| Primakoff 1 | 1 | 775 | 775 |
| Primakoff 2 | 2 | 2095 | 1048 |
| Primakoff 3 | 20 | 2744 | 138 |
| Minimum Bias Trigger | 160 | 21164120 | 132276 |
| Inner Veto | 500 | 5567702 | 11136 |
| Halo Trigger | 150 | 1193424 | 7957 |
| Beam Trigger | 2800 | 40604183 | 10971 |
| alternative Beam Trigger | 2800 | 30717481 | 8395 |
| Kaon Trigger | 1 | 17794 | 17794 |
| True Random | 1 | 22648 | 22648 |

olds as well as the selected regions. One has to take care that the physics is not affected by this selection. An overview of the tuning analysis can be found in fig. 3.18. For the summation trigger P1 a region of 12x12 cells and a region of 16x16 cells have been studied where the bigger area has an improved acceptance for final states containing π^0 or η particles. For the P2 trigger, the area which has to be selected, can be calculated from the cross-section and depends on the threshold, which is used, fig. 3.5. The trigger threshold as well as the veto threshold can be tuned while the veto-threshold has no significant impact on the trigger rate in case values above 10 GeV are considered.

As a final configuration, a summation area of 12x12 cells is selected with a threshold of 63 GeV. Further, a trigger threshold for the single-cluster trigger P2 of 25 GeV with a veto of 18 GeV is chosen. Combining these two triggers a trigger-rate of 30×10^3 /s is reached when taking into account the overlap of both triggers.

In order to allow some triggers to be collected by the low-t trigger, P2 has been prescaled by a factor of two, in case this trigger is active.

3.16 Performance

The performance of a trigger is given by two parameters, efficiency and purity. In order to calculate the purity, the ratio of recorded events with the desired properties have to be divided by all events. In terms of this quantity both Primakoff triggers perform rather non-selective. This is obvious because they do not identify the point where the reaction takes place and the signature of energy deposit in the calorimeter is rather rough. Because any kind of reaction having hadrons or photons in the final state may mimic this signature, this background is dominant for the measurement with hadron beams.

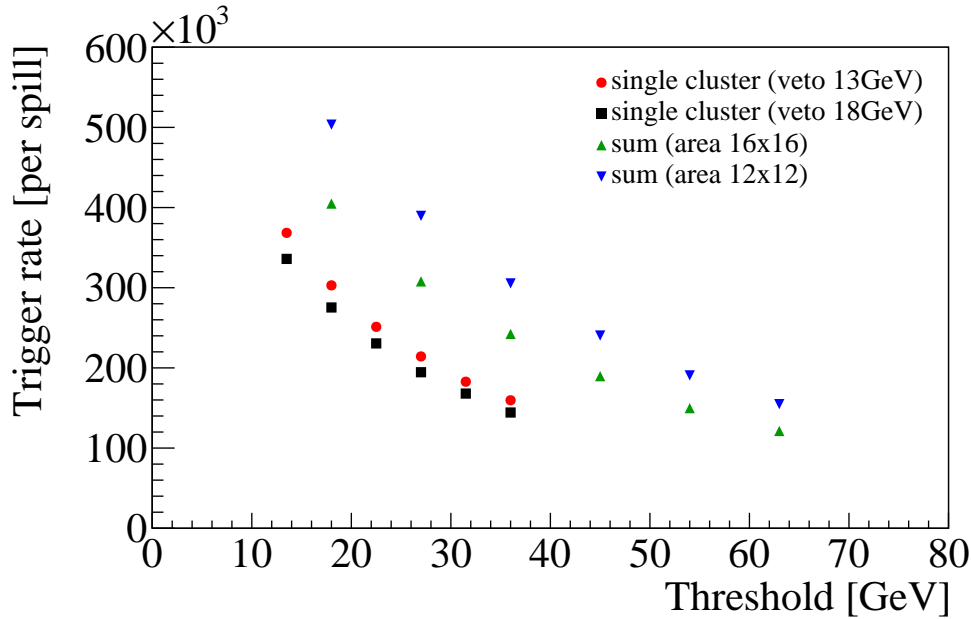


Figure 3.18 Threshold scan for the Primakoff triggers. The individual trigger rates are shown as a function of the threshold. For the summation triggers two different areas are scanned. For the single cluster trigger also the veto threshold is changed.

The selection of a single cluster increases slightly the purity, but still both triggers have an overlap of 75% in the region where P1 is sensitive. This leads to the fact that for the reaction $\pi^- \text{Ni} \rightarrow \text{Ni} \pi^- \gamma$ the purity is at sub-per-mille level. In case of the reaction $\mu^- \text{Ni} \rightarrow \text{Ni} \mu^- \gamma$ the situation is much better, the measured ratio of triggered events and reconstructed events is about 3%. Taking into account a reconstruction efficiency of about 18% the purity for this reaction can be estimated to $3\%/18\% = 17\%$. This indicates the loss of purity due to the unknown vertex position.

Further it is important to check that the regions in which the trigger is active correspond to the regions which have been selected during preparation. For this purpose, events containing exactly one ECAL2 cluster are used. In addition they have to be above the threshold of the trigger under study. This can be seen in fig. 3.19 for both trigger schemes. It can be seen that for most of the events the reconstructed clusters are within the desired regions.

The same approach can be made by allowing additional clusters to be reconstructed in ECAL2. These additional clusters may have the highest energy and thus plotting the distribution of the cluster with the highest energy provides insight to the region which was excluded from the veto for P2, fig. 3.20 (a). Comparing this to fig. 3.19 (b) the region where the beam-particle ends up gets visible on the right-hand side of the detector. In fig. 3.20 (b) the distribution of the reconstructed, good $\pi^- \text{Ni} \rightarrow \text{Ni} \pi^- \gamma$ tracks extrapolated to the surface of the detector is shown. All tracks end up in the region excluded from the veto. Another area which is not used for the veto can be seen on the left-hand side of the

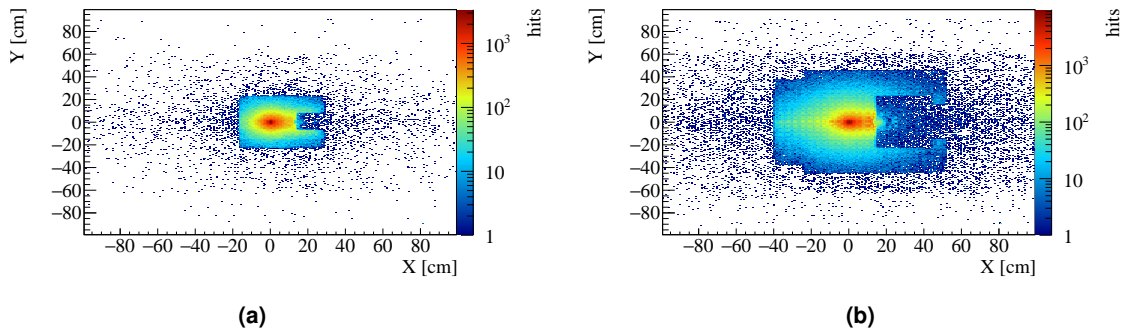


Figure 3.19 Distribution of the reconstructed clusters for the two different triggers, P1 in (a) and P2 in (b). Only events with exactly one cluster which is above the trigger threshold are used.

detector. This region is deactivated by mistake however this only affects the purity.

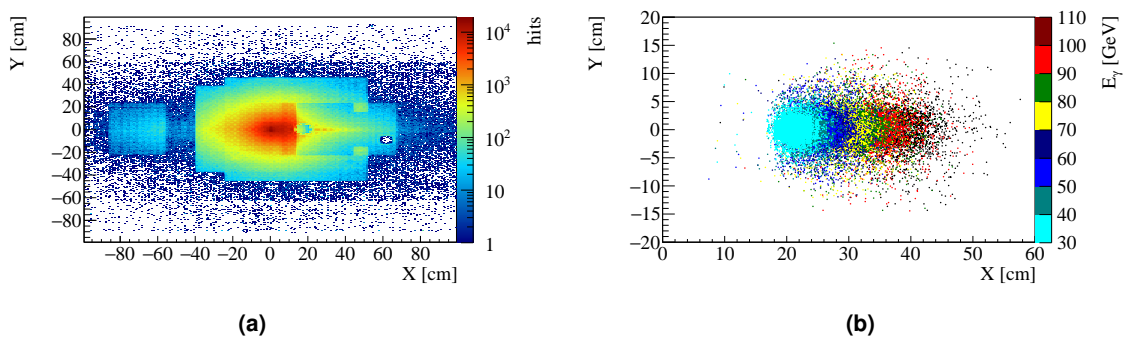


Figure 3.20 Distribution of the maximum cluster for the P2 trigger (a). Events with one cluster above the trigger threshold have been selected. This is the same picture than fig. 3.19 (b) but the requirement of exactly one cluster is skipped. In (b) the reconstructed distribution of outgoing tracks from the reaction $\pi^- \text{Ni} \rightarrow \text{Ni} \pi^- \gamma$ are shown. The color-scale gives a binning in track momenta.

The efficiency of the trigger is determined using the minimum-bias trigger as a reference. Because this trigger is scaled down by a factor 160, a lot of data have to be analyzed in order to get an overlap between one of the Primakoff triggers and this reference. In the end the efficiency is determined by dividing the number of events which are selected by the trigger under study and the minimum-bias trigger by the number of events selected by the minimum-bias trigger. This is shown for P1 in fig. 3.21 (a) and for P2 in fig. 3.21 (b). The efficiency starts to rise close to the region which is defined as the threshold and settles at a stable efficiency above 99% at energies above 70 GeV for P1 and above 32 GeV for P2.

The slope of the onset of the trigger is rather wide with a full-width between 10 GeV and 20 GeV depending on the trigger. This effect is unavoidable because the calibration coefficients used in the trigger are not as precise as those used during the reconstruction. These are only obtained from the data after the end of data-taking.

3 THE CALORIMETER READOUT AND THE TRIGGER SYSTEM

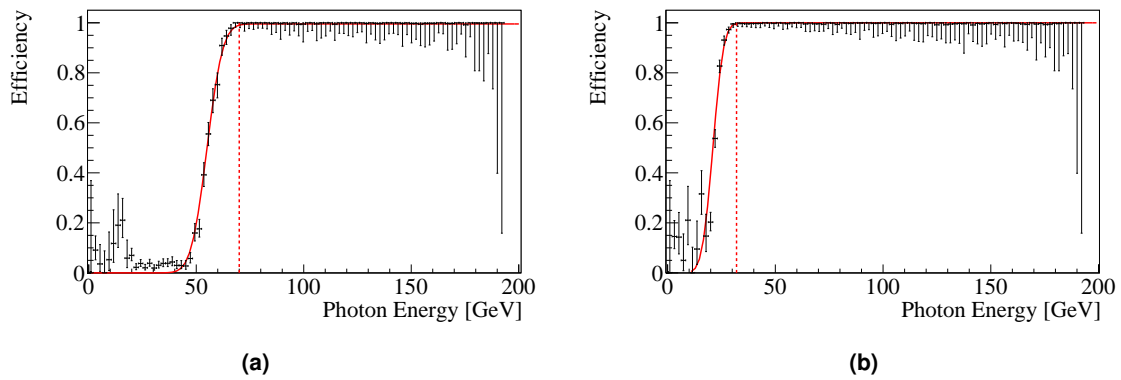


Figure 3.21 Efficiency of the Primakoff triggers as function of the energy of the cluster with the highest energy inside the trigger region. A fit with an integrated Gaussian gives a width for the rising edge of P1 of $\sigma=5.7$ GeV (a) the efficiency plateau of 99 % is reached at 70 GeV in this case and is indicated as dashed line. P2 has a slightly smaller width of $\sigma=3.9$ GeV and reaches its plateau at 32 GeV.

The calculated efficiency does not reach 100 % for both triggers. This effect is studied in great detail during the commissioning of the system. Changing the coincidence window between calorimeter-trigger and beam-trigger for instance has only a negative impact in extreme cases when the gate is too short like shown in fig.3.16 (a). It is found that in case of very low beam intensity, for which the minimum-bias trigger can be used without scaling the efficiency settles at 100 %. This leads to the conclusion that the effect, which reduces the efficiency, comes from the fact that the different triggers are affected differently by the dead-time of the experiment.

Chapter 4

Extraction of the charged-pion polarizability from 2009 data

The analysis described in this chapter was started in the preceding thesis by T. Nagel at the chair of S. Paul at Technische Universität München [29, 71]. During the cross-check procedure and the preparation for the publication it was found that the analysis still had to be improved. After performing all necessary analysis steps the work was submitted to the journal Physical Review Letters and accepted for publication [1] after an extensive reviewing process. In this chapter all relevant analysis steps are discussed as needed for achieving the final result, and the treatment of systematic errors is explained.

4.1 Target

The target selected for this measurement is a thin nickel disk with a length of 4.2 mm which corresponds to 28.5 % of one radiation length. The material has been chosen because of its relatively high atomic number of 28 in addition to its relatively simple nuclear structure: The most abundant Nickel isotopes ^{58}Ni and ^{60}Ni [72] have zero spin and are nuclei with the even number of protons and neutrons. This was judged to simplify the treatment of radiative corrections [73].

4.2 Trigger

The trigger used for this measurement is sensitive to the energy sum of the signals in the central part of ECAL2. It is sensitive to events from energies around 50 GeV and the triggered data can be used starting from photon energies around 76 GeV, c.f. fig. 4.1. The implementation is discussed in section 3 and more details can be found in [53].

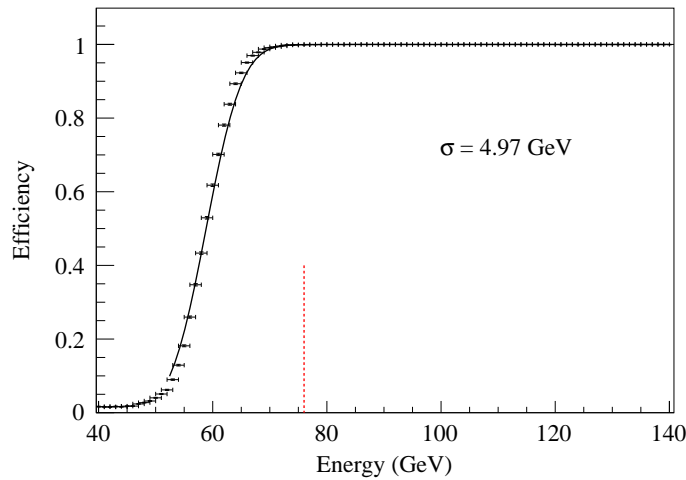


Figure 4.1 Efficiency of the ECAL2 trigger in 2009. The Distribution is fitted with an integrated Gaussian. The red dashed line corresponds to the applied threshold of $E_\gamma = 76$ GeV used in the analysis. The value quoted as sigma is the width of this fit[44].

4.3 Event selection

4.3.1 Reconstruction of photons

The reconstruction of the photons in the electromagnetic calorimeters is of central importance. A photon is reconstructed from clusters in the electromagnetic calorimeters. These clusters are fitted to the time/energy distribution over the cells and the analysis makes use of the measured time and energy. The resolution of the reconstructed time is better than 1 ns with tails extending up to about eight ns fig. 4.2 (a) which is used as a maximum time where a cluster is considered as belonging to the event. The time resolution improves with growing signal amplitude [44].

As can be seen from fig. 4.3, the distance of the track to a cluster depends on the cluster energy. This can be explained by the fact that hadronic showers are treated identical to electromagnetic showers by the reconstruction algorithm. It may happen that energy deposited in the calorimeter cells with small energies are not associated to the main cluster and thus their distance to the impact point of the track is wrongly calculated. Clusters are disregarded in case they are associated to the track of the scattered pion, where the maximum distance for association to the track is given by

$$(4.1) \quad dR_{\max.} = 3 \text{ cm} + \frac{16 \text{ cm/GeV}}{E_{\text{clus}}}.$$

For real data the clusterization algorithm works well while for Monte Carlo data there is a probability of about 4.5% that a cluster gets split into two clusters having a small distance, c.f. fig. 4.2 (b). This is compensated by assuming that clusters with a distance

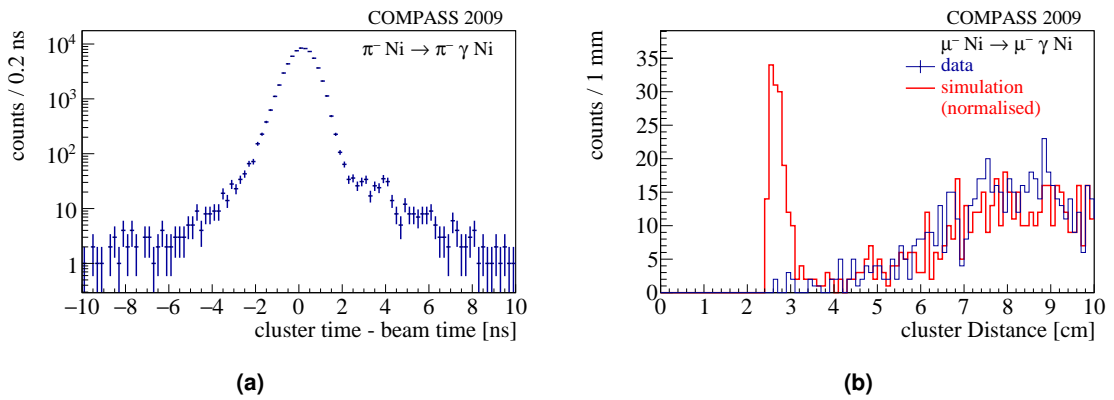


Figure 4.2 In (a) the time distribution relative to the beam time for all clusters matching the selection criteria for the reaction $\pi^- \text{Ni} \rightarrow \pi^- \gamma \text{Ni}$ is shown. Only clusters in a time-window of ± 8 ns are used. In (b) the radial distance between all reconstructed clusters is shown for data in blue and for the simulation in red. It can be seen that an artificial peak at cluster distances around 3 cm is created in simulation.

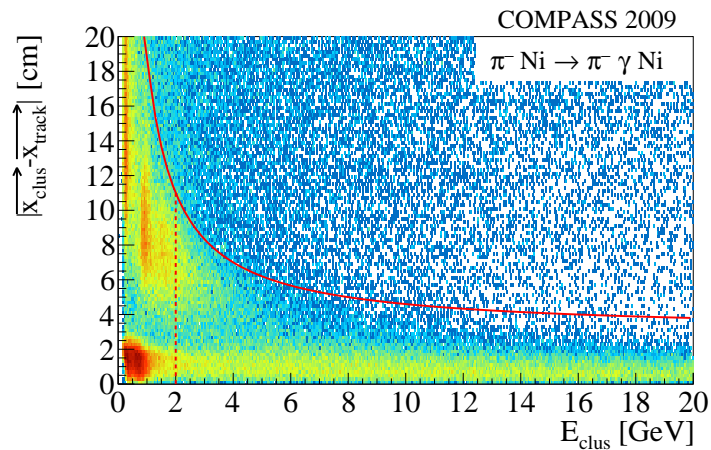


Figure 4.3 Distance of the track, extrapolated to ECAL2, to the cluster position versus the cluster energy for all clusters. All tracks with momenta above $76 \text{ GeV}/c$ are considered. The distance of correlated tracks depends on the cluster energy, the cut is indicated as a red line. The vertical, dashed line indicated the threshold below the clusters are not considered at all.

of less than 5 cm to the cluster with the highest energy originate from the same incident particle. In this case the energy is calculated as the sum of all contributing energies and the position is calculated as the weighted mean.

The Lorentz vectors of the photons are calculated with the direction given by the cluster position and the position of the primary vertex with the modulus given by the measured energy in the calorimeter.

4.3.2 Preselection

Events are considered in the analysis when they have exactly one primary vertex consisting of an incoming beam-particle and exactly one outgoing, charged particle. Further it is required that at least one cluster is found in the electromagnetic calorimeter, ECAL2, with an energy of more than 30 GeV. This selection results in about 124 million events which are further analyzed.

4.3.3 Excluded data

Data are considered only in case they fulfill the following quality requirements, evaluated for each spill:

- The mean energy balance $\Delta E = E_{\text{beam}} - E_{\gamma} - E_{\pi^-}$ is close to its average value within a limit of 1 GeV
- The beam position is close to its average value with an offset of less than 2 mm
- There are no known problems with the beam-line (taken from logbook entries)
- All time-dependent calibrations of the calorimeter are available
- The global time reference (TCS phase) is plausible (It may happen that the distribution is shifted by multiples of one clock cycle)

In case the data is not conform with these criteria it is put to a list of bad spills and ignored for further analysis. In total about 3.5 % of the data are excluded by these criteria.

4.3.4 Quality cuts on the scattered particle

In order to exclude cases in which the scattered charged particle may be ill-reconstructed in order to avoid this several cuts are applied in order to ensure the track quality:

- There are no other vertices attached to the track
- The reconstructed charge of the track is $-1 e$

- There are two well-defined space points in the downstream silicon detectors this means at least one hit in each of the combinations SI04X/U, SI04Y/V, SI05X/U, SI05Y/V
- The track does not cross the yoke of one of the spectrometer magnets

4.3.5 Cut on the trigger mask

It is required that the event is triggered by one of the two Primakoff triggers and these triggers determine the time of the event. Because of the high trigger efficiency and the reduced rate of the other triggers, this cut has practically no impact on the final number of events.

4.3.6 Cuts on the beam parameters

The event is triggered some beam particle in case this particle is detected by the beam-counter disk. In order to ensure that only events are considered where the detected track has triggered the read-out, it is required that the beam-track passes through this disk within a radius of 1.5 cm. Further it is insured that the incoming particle is not part of the beam-halo where the momentum and particle type is not well known. This is done by selecting $\sqrt{(dX/dZ - 4.6 \times 10^{-5})^2 / (2.7 \times 10^{-4})^2 + (dY/dZ - 2.2 \times 10^{-4})^2 / (3.3 \times 10^{-4})^2} \lesssim 1$ which corresponds to an average cut on the divergence of $dR \lesssim 0.3$ mrad for the hadron beam. For the muon beam the cut is widened to $dR \lesssim 0.6$ mrad due to the larger beam spread. The cut which is applied at the end does not follow exactly this formula as it is slightly elliptic due to the shape of the beam-profile, c.f. fig. 4.4. The central value of the cut is chosen identically for pions and muons in order to describe similar kinematics.

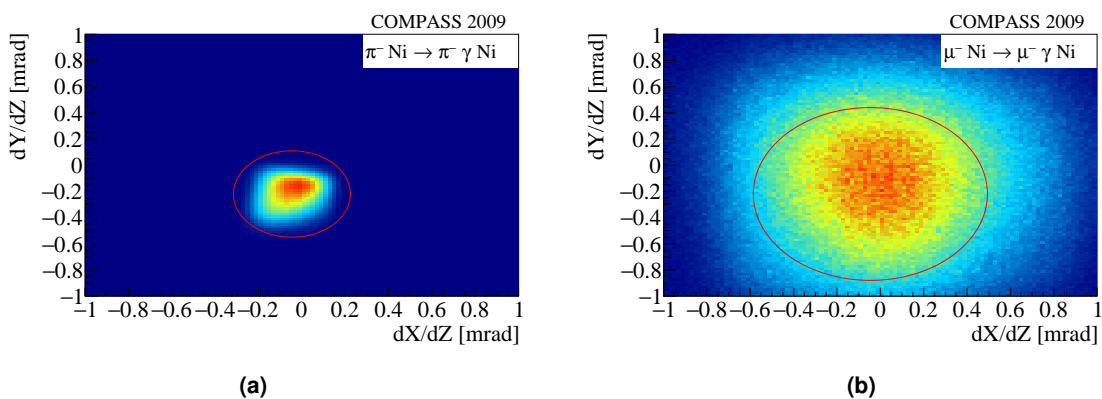


Figure 4.4 Beam divergence in 2009 for pions (a) and muons (b). The applied cut is indicated as a red ellipse.

4.3.7 Vertex position

As only reactions in the nickel target are of interest, the position of the vertex is checked to be consistent with a reaction within the target. While the cut on the beam-counter described above already confines the position in XY -direction to the nickel disk, c.f. fig. 4.5(a), the Z -position has to be selected explicitly. In case of one outgoing track the resolution in Z -direction significantly depends on the scattering angle and thus a corresponding empirical selection is given by

$$(4.2) \quad |Z - Z_{\text{mean}}| \leq 2.5 \cdot \left(0.5 \text{ cm} + \frac{6.5 \text{ cm/mrad}}{\theta} \right).$$

Here $Z_{\text{mean}} = -72.6 \text{ cm}$ describes the nominal target position and θ the scattering angle. At very small scattering angles the resolution does not allow to distinguish events from the nickel target from those produced in the tungsten discs, so an additional angle-independent cut on $Z \leq -50 \text{ cm}$ is applied.

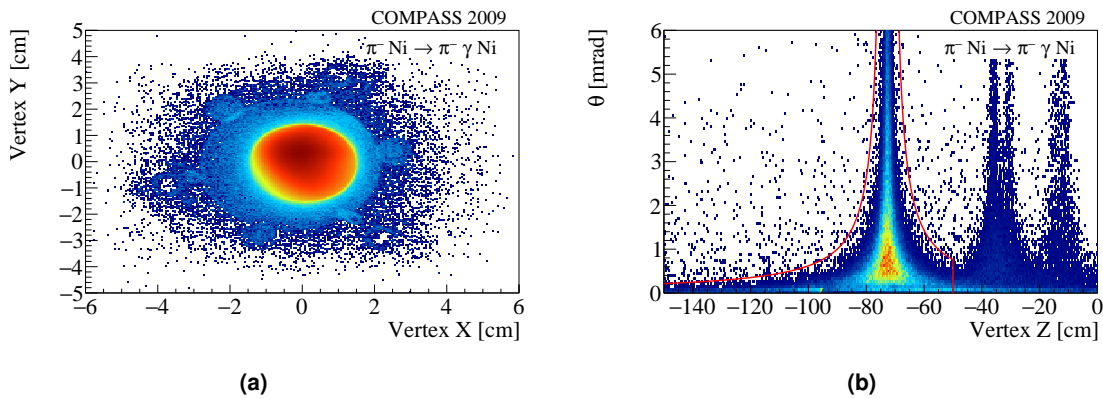


Figure 4.5 Vertex position measured in 2009, in (a) the XY position with only the cut on the vertex Z to lie in $\pm 1 \text{ m}$ position and the cut on the transverse momentum p_T applied is shown. The enhancement from the beam-counter constrains the vertex inside the Nickel disk. Additional round structures are visible at the positions of the holding rods of the target. In (b) The vertex scattering angle as a function of the vertex Z -position is shown without a cut on $m_{\pi\gamma}$ and the transverse momentum. The Nickel and the Tungsten targets are visible as well as the downstream silicon detectors. The applied cut is indicated as red lines. Background visible at very low scattering angles where the target position cannot be determined accurately anymore will be rejected by the cut on p_T , section 4.3.13.

4.3.8 Four-momentum transfer

The main identification criterion for the photon exchange is the so-called Primakoff peak, c.f. [74]. Due to experimental resolution, it is significantly wider, c.f. fig. 4.6, than in simulation, c.f. fig. 1.4. In order to separate strong interaction from the Compton scattering, a cut on $Q^2 < 1.5 \times 10^{-3} (\text{GeV}/c)^2$ is applied, which is close to the point where the two

processes have similar strength if the experimental resolution is taken into account. This corresponds to $\sqrt{Q^2} < 3.8 \times 10^{-2} \text{ GeV}/c$.

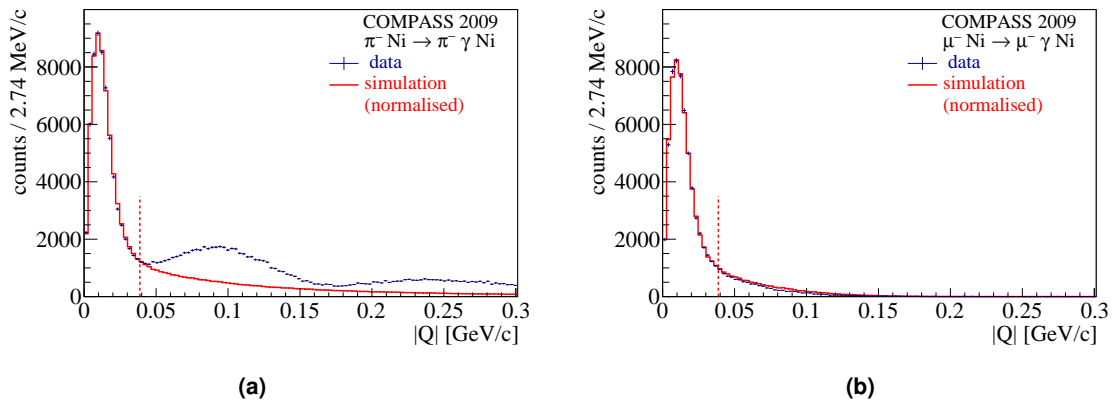


Figure 4.6 (a) Distribution of the four-momentum transfer [1] in 2009 for pions. For better visualization the square-root of the distribution is taken. Slight deviations between the simulated events in red and the reconstructed data in blue stem from the structure of the calorimeter cells which is not reproduced in simulation. The cut is indicated as a dashed line. In (b) the same plot is shown for muon data.

4.3.9 Cut on additional tracks in the spectrometer

In order to remove background stemming from π^- -electron scattering, as will be described in section 4.5.2, a cut on the number of reconstructed tracks is used. Events are rejected in case more than one track with measured momentum and time are found where the first measurement point is upstream of ECAL2. These tracks are only taken into account when their time corresponds to the time of the beam-particle within 4σ resolution and if their momentum is less than $170 \text{ GeV}/c$ which ignores the unscattered beam and elastically scattered pions.

4.3.10 Cut on the recoil proton detector

The RPD is used to detect the recoiling protons [75] in case of measurements with liquid hydrogen target. In that case the lower limit for detecting the recoiling proton in the detector is given by a minimal four-momentum transfer $Q^2 = 0.1 (\text{GeV}/c)^2$. In case of the very low four-momentum transfer of the Primakoff reaction these conditions are not fulfilled. Further the protons would get absorbed within the Nickel disk.

The detector is used as a veto to the events in case a in time track is reconstructed. This may reduce some backgrounds e.g. by electron tracks which would not enter the spectrometer acceptance. No detailed studies about the final improvements by this cut were performed.

4.3.11 Exclusivity cut

In order to enrich exclusive $\pi^- \text{Ni} \rightarrow \text{Ni} \pi^- \gamma$ reactions at lowest Q^2 , events are only kept for in the analysis in case the energy balance $\Delta E = E_{\text{beam}} - E_\gamma - E_\pi$ is fulfilled on the level of the resolution of $|\Delta| < 15 \text{ GeV}$. The distribution and its comparison to simulation can be found in fig. 4.7 for pion and muon data. The substructure around the peak position is not perfectly reproduced due the limited calibrations of ECAL2. The width is similar and the physics producing the shape e.g. given by the radiative tail towards lower energies is reproduced by Monte Carlo in which the radiation of additional photons is explicitly contained.

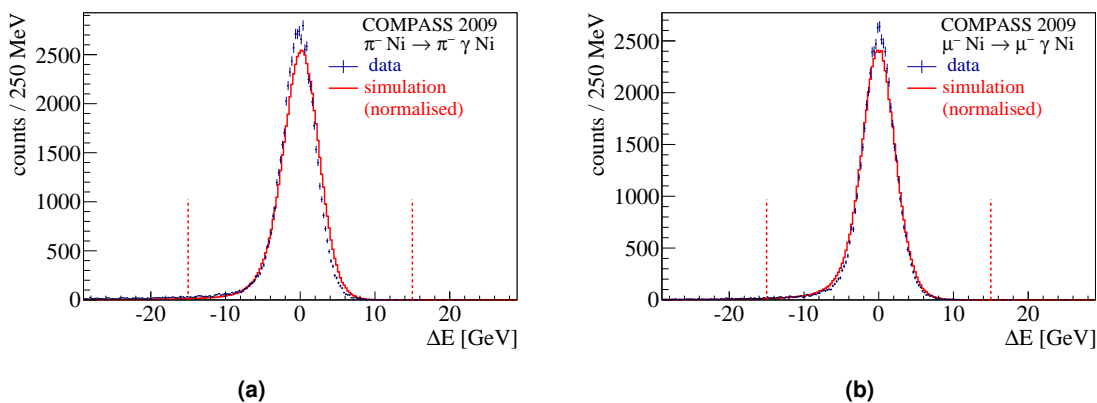


Figure 4.7 Distribution of the energy balance[1] in 2009 for pions (a). Slight deviations between the simulated events in red and the reconstructed data in blue stem from the structure of the calorimeter cells which is not reproduced in simulation. The cut values are indicated as dashed lines. The same plot for muon data is shown in (b).

4.3.12 Cut on the invariant mass of the $\pi\gamma$ -system

The cross-section is correctly described by the Monte Carlo in terms of the mass distribution of the $\pi\gamma$ -system. It starts with a peak at masses slightly above the π^- -mass, depending on the photon energy, and quickly falls off towards higher masses. The strength is almost vanishing at $m_{\pi\gamma}=1 \text{ GeV}/c^2$, fig. 4.8. In case of the reconstructed data a peak around $m_{\pi\gamma}=770 \text{ MeV}/c^2$ is visible, which can be understood by considering the reaction $\pi^- \text{Ni} \rightarrow \pi^- \pi^0 \text{Ni}$ which is resonating around the mass of the $\rho(770)$. One of the final-state photons may not be detected and thus the reaction. This can happen if it is not detected by the electromagnetic calorimeter because it has a too small energy or is lost by absorption in the spectrometer. For very high energetic π^0 s the two photons may impact at similar positions in the detector and only one common cluster is reconstructed. In these cases an event is miss-identified as stemming from the reaction $\pi^- \text{Ni} \rightarrow \text{Ni} \pi^- \gamma$. A cut on $m_{\pi\gamma} = 3.5 m_\pi$ is applied in order to remove this background. In addition, this cut limits the analysis to a range where the chiral expansion is valid, c.f. section 4.6.4.

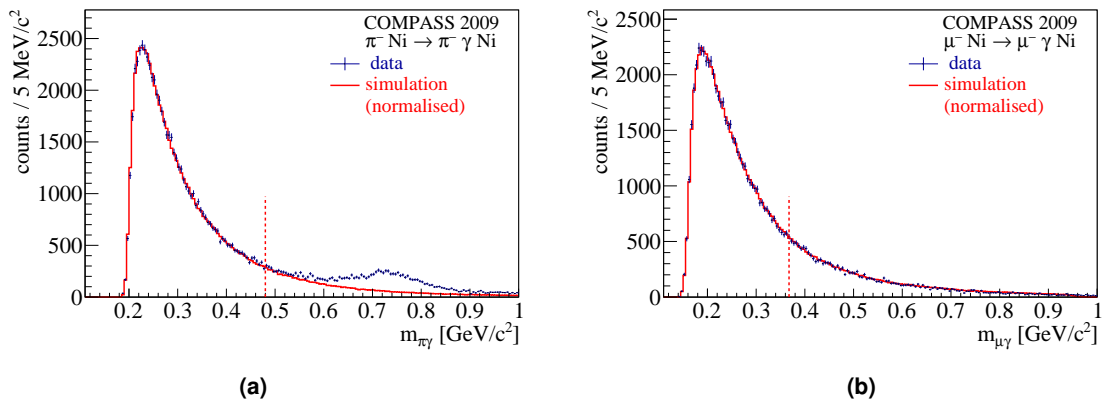


Figure 4.8 Invariant mass distribution of the $\pi\gamma$ -system[1] (a) in 2009. The red line describing the simulated data follows well the measurement points in blue up to the cut value of $m_{\pi\gamma} > 3.5 m_{\pi^-}$. This cut is indicated as dashed line. For higher values the data start to deviate from the simulation due to background from produced π^0 s which are miss-identified due to one lost photon. The same plot for muon data is shown in (b).

4.3.13 Cut on the transverse momentum of the scattered pion (p_T)

The transverse momentum of the scattered particle, fig. 4.9, is proportional to the scattering angle at a given momentum of the scattered pion. It is expected that the quality of the reconstructed vertex improves with higher transverse momenta, section 4.3.7. In order to remove events where the vertex cannot be reconstructed with a precision better than 6.7 GeV a cut on the transverse momentum of $p_T > 40 \text{ MeV}/c$ is applied.

For values of p_T bigger than this cut the distribution between simulation and measured data looks identical while for lower values a slight discrepancy can be seen. At very low values a peaking structure is visible. This originates from electrons contained in the beam which scatter at very low angles.

4.3.14 Cut on the number of photons in the final state

Despite of the cut on the energy balance as described above the selected events are not perfectly exclusive as can be seen in fig. 4.10 (a). Here the prominent peak from the reaction $\pi^- \text{Ni} \rightarrow \pi^- \rho(770) \text{Ni} \rightarrow \pi^- \pi^0 \text{Ni} \rightarrow \pi^- \gamma \gamma \text{Ni}$ indicates background from events with more than one photon in the final-state. With the goal of reducing this kind of background it is required that not more than one photon with an energy above $2 \text{ GeV}/c^2$ is found in the electromagnetic calorimeter ECAL2. Applying this cut reduces the background approximately by a factor five in the ρ -region, fig. 4.10 (b). The treatment of the remaining background is described in section 4.5.2.

4 EXTRACTION OF THE CHARGED-PION POLARIZABILITY FROM 2009 DATA

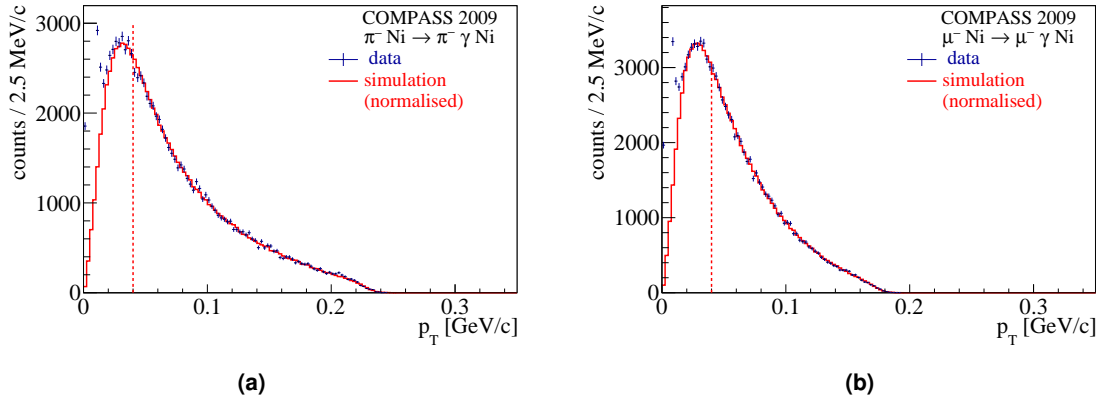


Figure 4.9 (a) Distribution of the transverse momentum p_T [1] of the scattered π^- in 2009 data. The measured data points in blue are well described by the simulated values in red for values of $p_T > 40$ MeV/c, indicated as dashed line. Smaller values are less well described. At very small p_T a peak from the electron induced reaction is visible. The same plot for muon data is shown in (b).

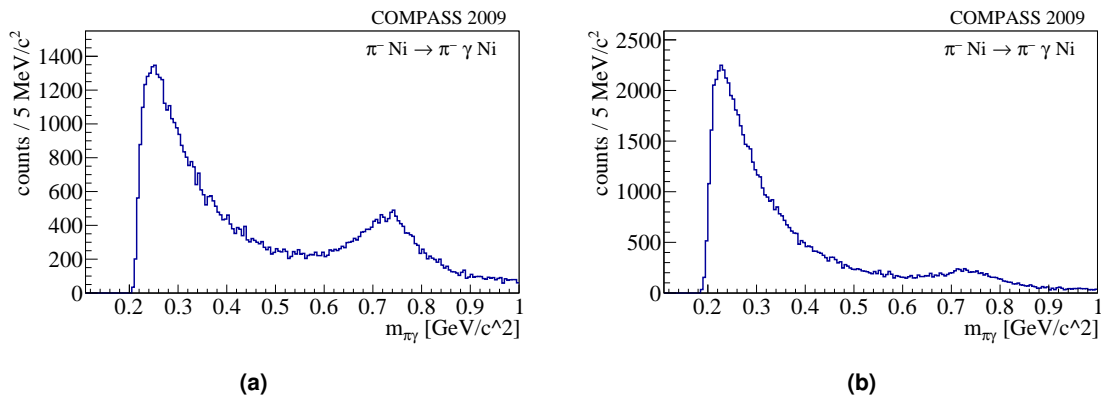


Figure 4.10 Invariant mass distribution distribution of the $\pi\gamma$ system. In (a) the cut on the number of photons in ECAL2 is not applied while it is applied in (b). A significant reduction of the $\rho(770)$ contribution can be seen. Be aware that the selection in (a) was not performed with the final selection criteria.

4.3.15 Identification of the beam particle

The beam contains a small fraction of kaons. These are identified using the CEDAR detectors as described in section 5.1. During the measurement in 2009 a problem with the TDCs which are used for these detectors was found along this analysis. The time measurement had jumps by 12.86 ns randomly during the spill. This problem is solved by applying a calibration taking into account these fluctuations.

4.3.16 Beam momentum measurement by the BMS

In case of the measurement with the muon beam the momentum of the beam is measured by the beam momentum station(BMS). It has to be ensured that this measurement is correct and thus only beam tracks which have at least two detector planes contributing to the measurement by the BMS are accepted. Further, it is required that the fit of the trajectory has a likelihood of more than 0.02 for lower values the measured momentum is fixed to a default value of 190 GeV/c due to the missing precision.

4.4 Monte Carlo Simulation

For a complex apparatus like COMPASS the study of any physical process requires a detailed simulation of the experiment. Especially for the determination of the pion polarizability it is crucial because the result is extracted from the ratio between simulation and measured data, relying on a realistic simulation of at least the relevant distributions as shown in the previous sections of this chapter.

4.4.1 Beam and vertex generation

Realistic events are only generated when the full kinematics of the beam is used. This is done by choosing the momentum of the beam, its gradients $dx/dz, dy/dz$ and the position in x and y direction on a fixed position along the beam direction, including all correlations between these five variables, according to a distribution extracted from real data. In the case of a pion beam this distribution is extracted from exclusive events selected from the reaction $\pi^- \text{Ni} \rightarrow \pi^- \pi^- \pi^+ \text{Ni}$ at four-momentum transfers $Q^2 < 1.5 \times 10^{-3} (\text{GeV}/c)^2$. In order to remove background, events are rejected in case the momentum reconstructed from the final-state differs by more than 4 GeV/c from the momentum estimated according to the parametrization described in section 5.3 [76]. The resulting momentum spectrum can be found in fig. 4.11 (a). In case of the muon exclusive $\mu\gamma$ events have been chosen according to the criteria described within this chapter, the momentum is given by the BMS measurement fig. 4.11 (b). The position of the vertex along the beam direction is generated as a uniform distribution over the target region, this is a safe assumption for thin targets, e.g the 4 mm Nickel disk. For longer targets absorption of the beam inside the target has to be taken into account.

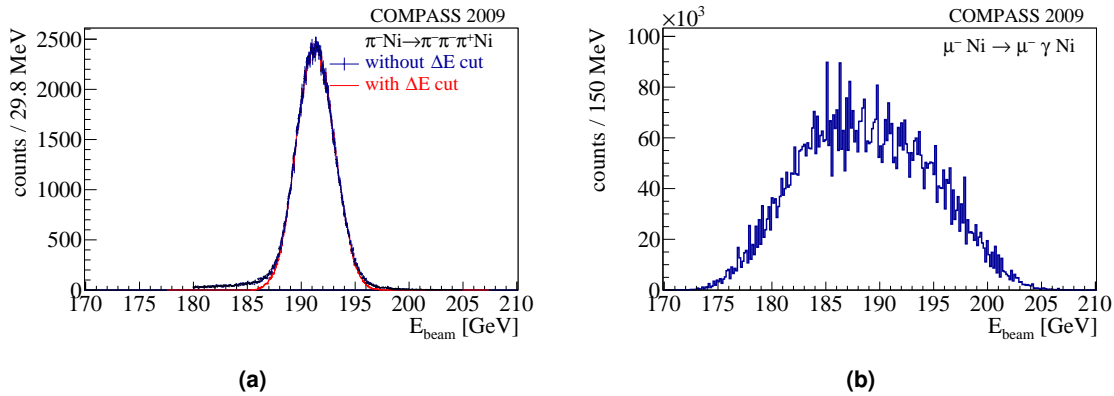


Figure 4.11 Distribution of the beam energy in 2009 for a pion beam (a) and a muon beam (b). In (a) the distribution of all 3π -events is shown in blue and with the cut on the beam energy given by the parametrization is shown in red. In (b) the distribution measured by the BMS is shown.

4.4.2 Event generators

In order to study the exact shape of the cross-section, the event distributions have to be generated accordingly. Two event generators have been studied in context of this analysis.

The first one called Polaris[77] is based on a code written in Fortran, it uses a fixed beam momentum and a sample-and-reject method based on the cross-section limited by the fixed kinematics of the beam. The momentum transfer spectrum is described by the assumption of a fixed energy transfer to the nucleus being exactly zero. In a next state the actual distribution of beam momenta is used to transform the Lorentz vectors of all particles according to a realistic distribution in real data. This transformation is only an estimate because also the cross-section depends on the incoming beam energy and especially for muons the momentum spread has a range from about $170 \text{ GeV}/c^2$ to $205 \text{ GeV}/c^2$.

The second "TUM" generator has been developed in the framework of [78] and written at Technische Universität München and is based on the calculations in [79, 73]. It features a calculation based on the cross-section where the full beam kinematics is used. It further allows taking into account all features of the influence of equivalent photon density to the momentum transfer spectrum. Further it includes electromagnetic corrections to the Compton vertex and soft photon emission as well as contributions from next-to-leading order calculations from χ PT[80]. It is possible to simulate the cross-section under the assumption of different values of pion polarizability c.f. fig. 4.12, where a simulated value of pion polarizability $\alpha_\pi = -\beta_\pi = 2.70 \times 10^{-4} \text{ fm}^3$ has been extracted after applying the full analysis chain.

Comparing the analysis based on the two different event generators using tree-level calculation in both cases leads to different values of polarizability. In order to study the influence of the two different approaches data has been simulated with a fixed beam mo-

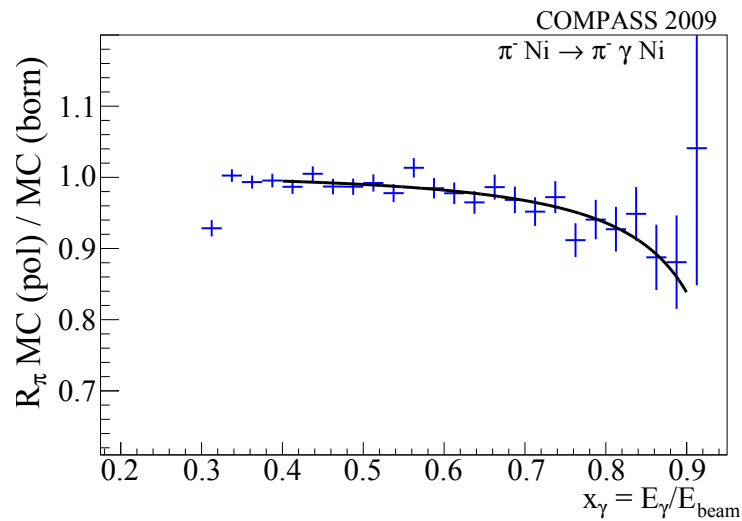


Figure 4.12 x_γ ratio for two MC simulations, a simulation with $\alpha_\pi = -\beta_\pi$ set to $2.70 \times 10^{-4} \text{ fm}^3$ is divided by a simulation with both polarizabilities set to zero. Fitting the distribution leads to a value of $\alpha_\pi = (2.70 \pm 0.54) \times 10^{-4} \text{ fm}^3$.

momentum of $190 \text{ GeV}/c$ where a difference in the result of $\Delta\alpha_\pi = (0.1 - 0.2) \times 10^{-4} \text{ fm}^3$ is extracted. Detailed analysis of the generators shows that in the polaris generator the angular dependencies are not correctly reproduced. This can be seen from fig. 4.13 where the ϕ -angle between the production plane (spanned by the beam and the virtual photon) and the decay plane (spanned by the outgoing pion and photon) is shown as a function of the invariant mass of the $\pi\gamma$ -system. The data shown in fig. 4.13 (a) show a two-bump structure which is reproduced by the simulation using the "TUM" generator fig. 4.13 (b) while the distribution generated by Polaris cannot reproduce this structure fig. 4.13 (c). This leads to the decision that only the generator described in [78] is used for the extraction of the pion polarizability at COMPASS.

4.4.3 Simulating the COMPASS experiment

The simulation of all physical processes taking place after the generation of the primary interaction is simulated using the COMGEANT [39] a framework based on Geant 3.21 [81]. It simulates events provided by the event generators and propagates all particles through the spectrometer taking into account interactions with the material and particle decays.

During the preparation of the analysis by T. Nagel [29] the material distribution which is used in the simulation was compared in detail with the spectrometer and several discrepancies were found. Most prominent is the RICH beam pipe, a tube consisting of stainless steel inside the RICH detector. It is filled with Helium and is used in order to reduce the occupancy of the RICH detector by high-momentum tracks. It was found that this element was described as aluminum in the simulation framework and hence provided

4.5 Backgrounds

The backgrounds for the reaction $\pi^- \text{Ni} \rightarrow \text{Ni} \pi^- \gamma$ can be split into three groups. These are processes with a different particle in the initial state, reactions creating additional particles in the final state which are lost due to a limited reconstruction efficiency and the process where the reaction does not take place electromagnetically but via strong interaction in the pion-nucleus exchange.

4.5.1 Different particles in the initial state

Besides pions 96.9% there is a contribution of about 2.4% kaons and 0.7% anti-protons in the beam at the target position [44], an attempt to get more precise parameters is described in section 5.2.2. In these values, the contributions from muons and electrons is neglected. A more detailed analysis of these parameters is currently ongoing by M. Krämer [67].

All these particles may mimic the pion Compton-scattering process by performing exactly the same reaction but being misinterpreted as pions. In case of anti-protons the contribution is neglected as their fraction in the beam is very small and the cross-section is, according to equation 1.13 and the mass ratio, by a factor of about 50 smaller than for pions.

For kaons, a similar argument holds on the Compton scattering but the cross-section is smaller by about 87.7%. In addition to this reaction, kaons which decay with a decay length of $c\tau = 3.712 \text{ m}$ have a significant branching to decay into the $\pi^- \pi^0$ final-state. In case the π^0 decays into two photons, of which one photon is not reconstructed or both photons are merged in the reconstruction this mimics the $\pi^- \gamma$ final-state. In order to reduce these contributions the beam particle is identified using two CEDAR detectors [84] which identify the beam particles. Using the algorithm described in section 5.1 kaons are rejected with an efficiency of 94% [85] leaving only a marginal background contribution. The effect can be seen in fig. 4.14 where the peak in the invariant mass spectrum of the final state close to the kaon mass disappears when applying the cut on the beam PID.

Scattering of electrons in a bremsstrahlung processes is, due to the small mass of the electron of $511 \text{ keV}/c^2$, characterized by extremely small angles. According to [35] the mean emission-angle is given by $\theta_{\text{emis.}} = m_e c^2 / E_{\text{beam}} = 2.7 \mu\text{rad}$. That means this kind of background can be removed by requiring a minimum transverse momentum of the outgoing pion to be $p_T > 40 \text{ MeV}/c^2$ which corresponds to a cut on the scattering angle of about $\theta > 200 \mu\text{rad}$.

Muons are an inevitable background in every pion beam experiment as they are created in the decay $\pi^- \rightarrow \mu^- \bar{\nu}_\mu$. In case they are created upstream in the beam-line, only muons with a similar momentum distribution as the pions are transported towards the target by the bending magnets. In case they are created close to the target they have a uniform momentum distribution in the range $[m_\mu/m_\pi \cdot p_\pi, p_\pi]$. In a study using the Drell-Yan

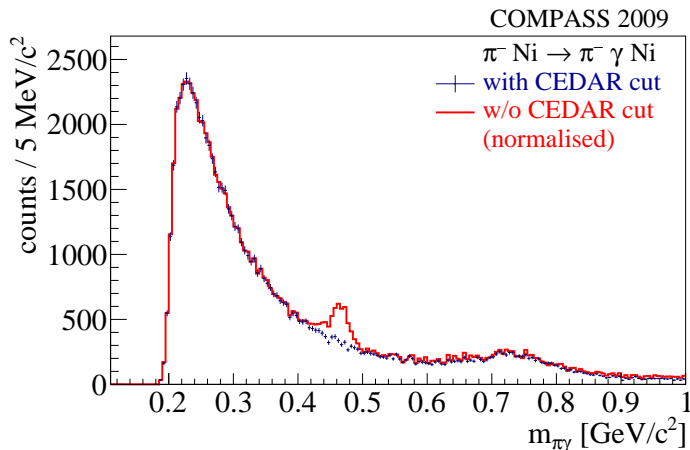


Figure 4.14 Invariant mass distribution 2009, the selection without CEDAR cut is shown in red, the selection with CEDAR cut in blue. The histograms are normalized to the integral over masses smaller than $0.4 \text{ GeV}/c^2$.

data taken in 2009 where a concrete block of hadronic interaction lengths was installed downstream of the target, the muon contamination has been estimated to be 1.2% [86] in the full kinematic range. In order to reject these events the COMPASS muon-system is used, it consists of a large amount of material stemming from the calorimeters and from concrete walls with detectors downstream of the absorbers to detect muons which passed through this material. It was found [29] that not all detectors in the muon system had been treated correctly by the reconstruction software and thus manual association of tracks is performed. Due to this material, a cut on the amount of traversed material in terms of radiation lengths of $X/X_0 < 15$ removes most of the muons, reducing the systematic contributions of muons to the pion polarizability to less than $0.05 \times 10^{-4} \text{ fm}^3$ [86]. This cut also rejects events where the scattered pion decays downstream of the target and thus the momentum reconstruction gets inaccurate.

4.5.2 Processes with more than two final state particles

In addition to the pure QED leading order contribution of pion Compton scattering, also higher-order electromagnetic terms contribute. These contributions contain corrections to the Compton vertex as well as the emission of soft photons and are calculated in [73]. While events with photons having an energy above 2 GeV , hitting the electromagnetic calorimeter ECAL2, are rejected due to the cut on the cluster multiplicity, the influence of low-energetic photons has to be taken into account. This is done on the simulation level by including these contributions in the event-generator [78]. The effect of these corrections can be quantified by dividing the measured data by a simulation taking into account only tree level calculations fig. 4.15(a) on the one hand and by a simulation also taking into account radiative corrections fig. 4.15(a) on the other hand. Fitting this ratio by equation 1.16, polarizability values of $\alpha_\pi = (1.4 \pm 0.6) \times 10^{-4} \text{ fm}^3$ and

$\alpha_\pi = (1.0 \pm 0.6) \times 10^{-4} \text{ fm}^3$ are extracted respectively. In addition to this quantitative statement on the result the quality of the fit improves by adding electromagnetic corrections as can be seen from the reduced χ^2 value which changes from $\chi^2 = 29.7/18$ to $\chi^2 = 22.0/18$.

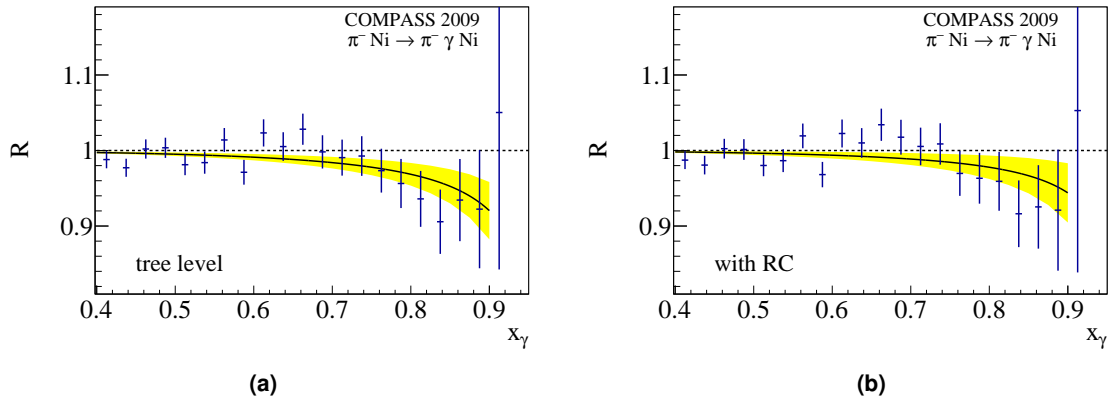


Figure 4.15 Fit to the x_γ -ratio R where in the simulation only tree level contributions (a) and radiative corrections (b) are considered. The extracted values are $\alpha_\pi = (1.4 \pm 0.6) \times 10^{-4} \text{ fm}^3$ with $\chi^2 = 29.7/18$ (a) and $\alpha_\pi = (1.0 \pm 0.6) \times 10^{-4} \text{ fm}^3$ with $\chi^2 = 22.0/18$ (b).

Ultra-peripheral scattering on a nickel target means not only scattering on the quasi-real photons surrounding the nucleus but also allows for scattering on the electron shell. In case of the pion-electron interaction (the momentum of the pion is 190 GeV/c and the electron is at rest) the invariant mass of the $\pi^- e^-$ -system is $0.46 \text{ GeV}/c^2$ while for muons (the momentum of the muon is 190 GeV/c and the electron is at rest) it is slightly smaller at $0.45 \text{ GeV}/c^2$, c.f. fig. 4.16. While the scattered pion or muon is detected in a certain relation of scattering angle and momentum, c.f. fig. 4.17(a) the electron may lose most of its energy into bremsstrahlung. In this case the bremsstrahlung photons sometimes create a cluster in the electromagnetic calorimeter which is within the exclusivity cut and thus wrongly interpreted as the final-state photon from a $\pi^- \gamma$ -process. In case the electron is still reconstructed as a particle stemming from the interaction in the primary vertex, these events are automatically removed from the sample by requiring only one outgoing charged track. Events in which the electron track is reconstructed but not attached to the primary vertex are rejected by requiring that no additional tracks are reconstructed in the spectrometer, c.f. section 4.3.9. Fig. 4.17(b) shows the relation between muon momentum and scattering after this cut is applied. It can be seen that the remaining contribution of this background is maximum at high muon momenta, corresponding to low values of x_γ . This cut obviously does not take into account tracks which are not reconstructed by the spectrometer. The systematic contribution to the pion polarizability is determined from the remaining effect of events of this cut, and is set to a value of $\pm 0.2 \times 10^{-4} \text{ fm}^3$ effect.

The most significant background in terms of a different final state is stemming from pro-

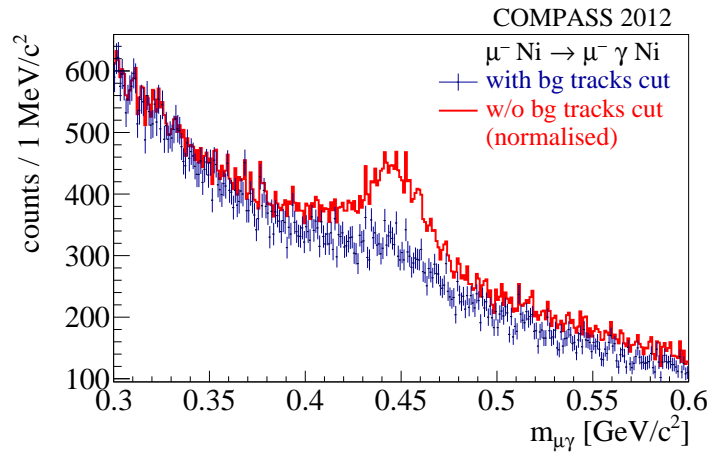


Figure 4.16 Invariant mass of the $\mu^- \gamma$ system, zoomed around the calculated mass for muon-electron scattering. The blue curve shows the effect of the cut on the number of background tracks compared to the red curve where this cut is not applied.

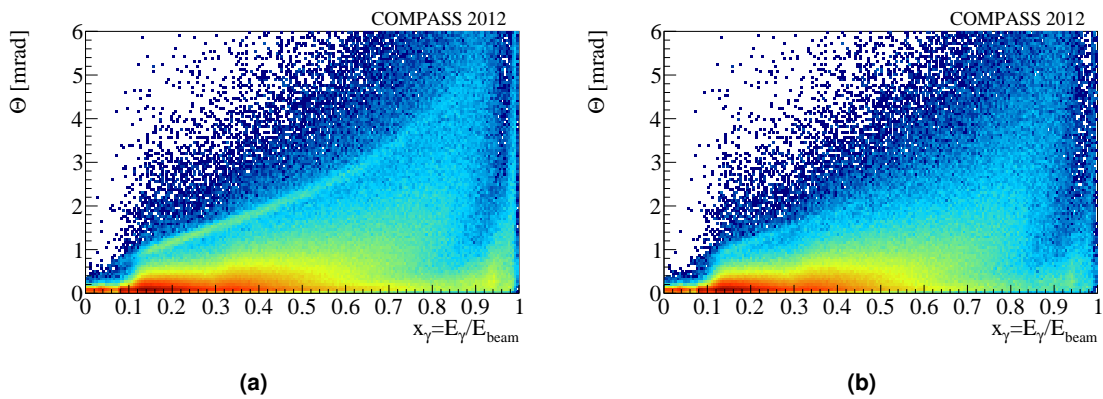


Figure 4.17 Scattering angle vs. the momentum of the scattered muon. In order to have a larger kinematic range, it is visualized from 2012 data. The picture is shown with no cuts applied (a) where an enhancement is seen at large scattering angles forming a band along the upper limit. This band is created by $\mu^- e^-$ -scattering. Cutting on the number of additional tracks in the spectrometer (b) significantly reduces this background where contributions only remain at high muon momenta.

cesses where one or more π^0 s are produced, mainly

$$(4.3) \quad \pi^- \text{Ni} \rightarrow \pi^- \pi^0 \text{Ni},$$

$$(4.4) \quad \pi^- \text{Ni} \rightarrow \pi^- \pi^0 \pi^0 \text{Ni}.$$

The decay of the π^0 s mainly into $\gamma\gamma$ with a branching ratio 98.8% [4] gives a background in case only one photon reconstructed, c.f. section 4.3.12. Cutting on the number of photons in the final-state is already very effective in reducing this background, c.f. section 4.3.14 but is still not sufficient as can be seen in fig. 4.8 (a) where a peak is visible around $0.77 \text{ GeV}/c^2$ stemming from the decay $\rho^- \rightarrow \pi^- \pi^0$. For studying this background we use the decay of kaons in the beam into $\pi^- \pi^0$ to correct for this background. A clean sample of these decays can be obtained by selecting events where the vertex is not inside of the target, in this case a region with a length of two meters upstream of the target has been selected fig. 4.18.

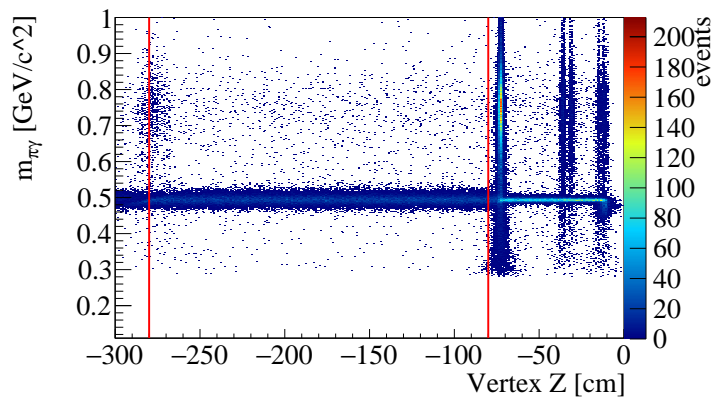


Figure 4.18

The influence of the π^0 -background is assumed to be dependent only on the π^0 energy. So using beam kaon decays one can calculate the ratio $r(x_\gamma) = N(x_\gamma)_{\text{K} \rightarrow \pi^- \gamma} / N(x_\gamma)_{\text{K} \rightarrow \pi^- \pi^0}$ of kaons decaying into π^0 , c.f. fig. 4.19, identified as events where one photon is lost. The quantity x_γ is calculated as $x_\gamma = 1 - E_{\pi^-} / E_{\text{beam}}$. This gives the probability for the misidentification. Measuring the number of correctly identified $\pi^- \pi^0$ events produced inside of the target $N(x_\gamma)_{\pi^- \text{Ni} \rightarrow \pi^- \gamma \text{Ni}}$ gives a measure of how many events are expected within one bin of x_γ . The number of background events can be calculated as

$$(4.5) \quad B_{\pi^0}(x_\gamma) = K \times r(x_\gamma) \times N(x_\gamma)_{\pi^- \text{Ni} \rightarrow \pi^- \gamma \text{Ni}}$$

where $K = 0.90$ is a factor taking into account the difference in acceptance between events in the target and upstream due to absorption in the target determined from simulation by [70]. The background fraction can be found in the lower panel of fig. 4.20. The effect of applying this correction is $\Delta\alpha_\pi = (0.5 \pm 0.2) \times 10^{-4} \text{ fm}^3$ where the error indicates the statistical uncertainty as well as systematics stemming from not explicitly taking into

account the $\pi^- \pi^0 \pi^0$ final-state.

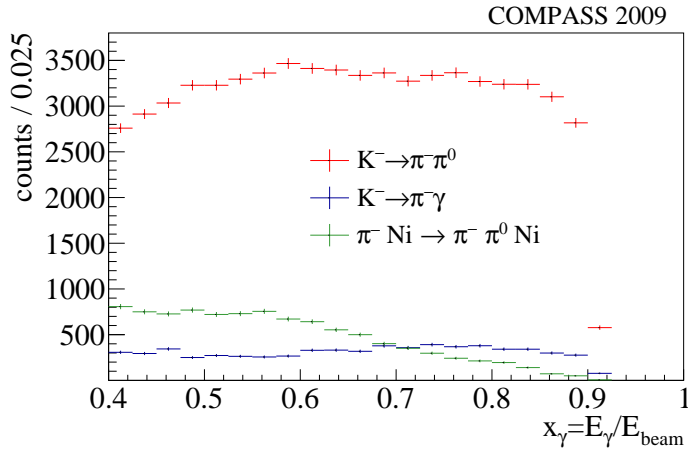


Figure 4.19 Plot from which the π^0 -background is extracted, yields as a function of x_γ are shown. The number of kaons decaying in the selected volume and which are detected in the final-state $\pi^- \pi^0$ (red) the events where one photon is missed are shown in blue. In green the number of π^0 's produced in the target are shown, this quantity is used for normalization.

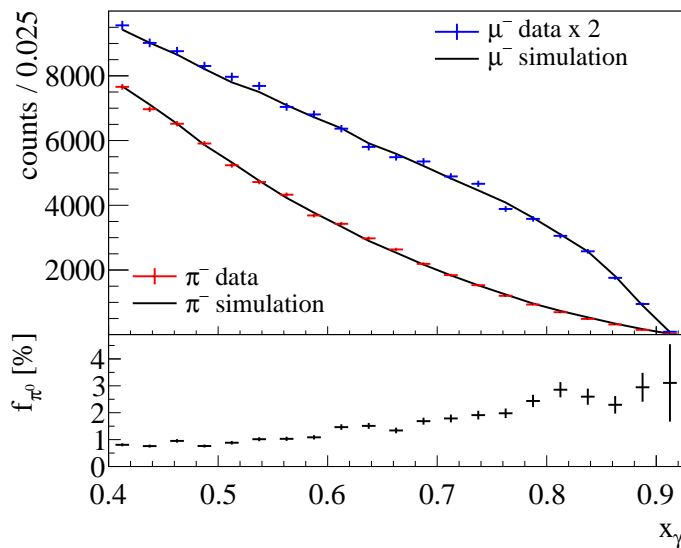


Figure 4.20 The top panel shows the measured cross-section shape as a function of x_γ . The measured data for pions (red) and muons (blue) are overlaid with continuous lines depicting the simulation. The bottom panel shows the corresponding π^0 -fraction.

4.5.3 Background from strong interaction

At very small momentum transfers the cross-section is dominated by the photon-exchange mechanism, at values of $Q^2 \approx 2 \times 10^{-3} (\text{GeV}/c)^2$, fig. 4.6 (a) the contribution from strong-interaction leading to the same final-state has approximately the same strength and is dominating at higher values fig. 4.21. The contribution from strong interact can be described by the dependence of the intensity on Q^2

$$(4.6) \quad I_{\text{strong}}(Q^2) = I_0 \cdot Q^2 \exp(-b \cdot Q^2)$$

where the slope parameter b is related to the strong-interaction radius of the Nickel nucleus. As the contribution from Primakoff and strong interaction have to be added coherently [87] the total intensity may be written as

$$(4.7) \quad I(Q^2)_{\text{tot}} = I(Q^2)_{\text{primakoff}} + I(Q^2)_{\text{strong}} + I(Q^2)_{\text{Interf.}}$$

where the interference term is given by

$$(4.8) \quad I(Q^2)_{\text{Interf.}} = 2\sqrt{I(Q^2)_{\text{primakoff}} \cdot I(Q^2)_{\text{strong}}} \cdot \cos \phi.$$

In order to determine the contribution from strong interaction to the polarizability measurement fits to the Q^2 -spectrum have been tried in several approaches. A simple fit to the data using the formulas given above leads to a very inconclusive result which can be seen from values of χ^2/NdF around 20. The reason is that the experimentally observed spectrum is not only described by these equations, but features in addition contributions stemming from e.g. resolution, acceptance and the e.m. form-factor of the Nickel nucleus. These studies have been performed using two slightly different approaches which mainly differ in the way of describing the resolution. While one approach [88] uses a full formulation based on equations where the resolutions are smeared by according Gaussian functions, the other approach [89] gets the shape of the Primakoff distribution and the resolution from the MC simulation. As these studies are statistically limited with this data-set, the number of bins in x_γ is reduced from 24 to 5 and fits are performed in these bins. A fit to the total spectrum can be seen in fig. 4.21 where a slope parameter of $b = 179 \pm 11 (\text{GeV}/c)^{-2}$ and an interference with $\cos \phi = 0.37 \pm 0.07$ are extracted. Performing the fit in bins of x_γ results in a correction term of $\Delta\alpha_\pi = (0.27 \pm 1.45) \times 10^{-4} \text{ fm}^3$ when the fit may determine all parameters and $\Delta\alpha_\pi = (-0.06 \pm 0.11) \times 10^{-4} \text{ fm}^3$ when the slope parameter b is fixed to its central value. In these studies it has been assumed that the phase of interference is constant over the full Q^2 range. Having these uncertainties, the contribution of the strong background is only considered as part of the systematic error with a value of $\pm 0.2 \times 10^{-4} \text{ fm}^3$.

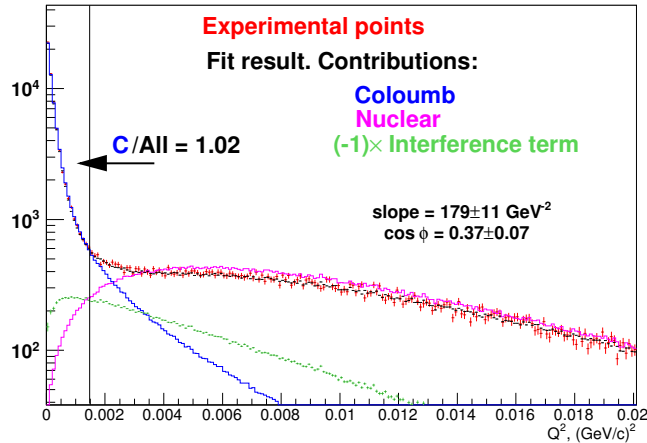


Figure 4.21 Fit to the Q^2 -spectrum over the total x_γ -range[89]. The data is fitted with a component stemming from strong interaction given by eq. 4.6 (magenta) smeared with the experimental resolutions, a component from the Primakoff process extracted from simulation (blue) and an interference term (green).

4.6 Systematic effects

Systematic effects on the measurement have been studied by varying different cuts, and by considering the different background contributing to the measurements, these are discussed in this section. Further the questions which appeared during the refereeing process are described.

4.6.1 Muon measurement

A key feature of the measurement at COMPASS is the use of a muon-beam to check systematic effects of the apparatus. After performing the same analysis as for pions, except some cuts which are necessarily different due to the different beam characteristics as discussed above, can be used to extract a fake polarizability value for the muon. For the simulation, the QED radiative corrections for the lepton scattering case are enabled, while chiral loop contributions are obviously not present in case of a lepton. The muon is a point-like particle and thus not polarizable. The magnitude of this "false" polarizability $\alpha_\mu^{\text{false}}$ therefore is a measure for apparatus effects having an influence to the determination of the pion polarizability. The ratio of reconstruct data events by reconstructed Monte Carlo events as a function of x_γ is shown in fig. 4.22. The resulting fit gives a value of $\alpha_\mu^{\text{false}} = (0.5 \pm 0.5) \times 10^{-4} \text{ fm}^3$. This value is added to the systematic uncertainties under the name "Determination of tracking detector efficiency", since it is assumed that the largest uncertainty is linked to this, such as the position dependent efficiencies as observed in section 5.7.2.

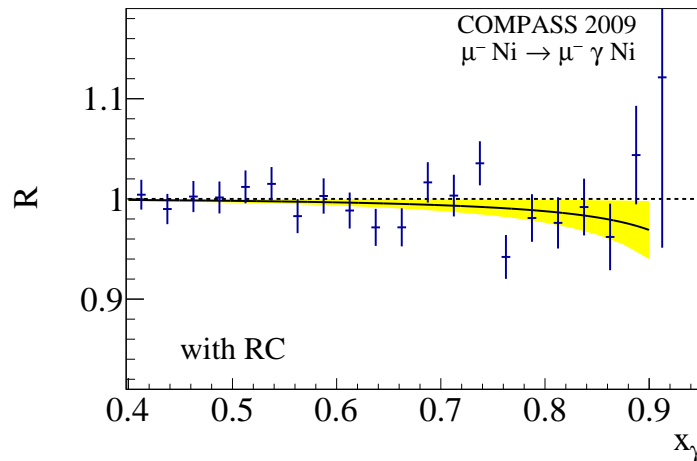


Figure 4.22 x_γ ratio for muons with radiative corrections enabled in the simulation [1]. The fit to the data is shown as a black line with its error indicated in yellow.

4.6.2 Uncertainty on the radiative corrections

In the event-generator QED radiative corrections are considered by simulating soft photon emission and corrections to the Compton vertex [73, 79, 78]. These corrections have a slight dependence on the assumed polarizability and thus a second iteration on Monte Carlo level putting in the already-extracted value of the polarizability, which is not performed so far. Higher order radiative corrections like multiple-photon exchange or the emission of more than one photon are not considered yet. Anyhow they are suppressed by orders of $\alpha \approx 1/137$ and thus considered only a tiny contribution. Further corrections like the screening of the nuclear charge by the electrons have been studied, but they had no visible effect. The current estimate on the uncertainty is based on the effect of the radiative corrections applied, thus $\Delta\alpha_\pi = \pm 0.3 \times 10^{-4} \text{ fm}^3$.

4.6.3 Influence of the background subtraction

The subtraction of the π^0 background is discussed in section 4.5.2 and its magnitude estimated to $\Delta\alpha_\pi^{\pi^0} = \pm 0.2 \times 10^{-4} \text{ fm}^3$. The same magnitude is assumed for the contribution from the background from strong interaction section 4.5.3 and the scattering on electrons surrounding the nucleus, section 4.5.1. An overview over all systematic error can be found in table 4.1. They are assumed to be independent and non-directional, so they are to be summed in quadrature. They add up to $\Delta\alpha_\pi = \pm 0.7 \times 10^{-4} \text{ fm}^3$.

4.6.4 Correctness of the chiral expansion

During the peer-review of the publication [1] the question was brought up if the leading-order chiral expansion is sufficient. In order to prove that we were provided by

Table 4.1 Estimated systematic uncertainties at 68 % confidence level.

| Source of uncertainty | Estimated magnitude [10^{-4} fm^3] |
|---|---|
| Determination of tracking detector efficiency | 0.5 |
| Treatment of radiative corrections | 0.3 |
| Subtraction of π^0 background | 0.2 |
| Strong interaction background | 0.2 |
| Pion-electron elastic scattering | 0.2 |
| Contribution of muons in the beam | 0.05 |
| Quadratic sum | 0.7 |

formulas extracted from dispersion relations [90] based on the calculations given in [11, 12]. Two expressions were calculated for values of $\alpha_\pi - \beta_\pi = 2.00 \times 10^{-4} \text{ fm}^3$ and $\alpha_\pi - \beta_\pi = 2.85 \times 10^{-4} \text{ fm}^3$. As shown in fig. 4.23 the discrepancy between the two approaches is much smaller than the effect given by polarizability or by the chiral loop contributions alone. Thus, up to the cut-value of $m_{\pi\gamma} = 3.5m_\pi$, the chiral approach is in very good agreement with the alternative approach of dispersion relations. This reconfirms that the application of this correction is justified and no alternative approach exists.

4.6.5 Effect of the cut on the invariant mass

It is expected that the polarizability may change up to 30 % [37] depending on the range in the invariant $\pi\gamma$ -mass chosen in the analysis. These effects are expected to contribute significantly at high values $m_{\pi\gamma}$. In the analysis only masses below $3.5m_\pi$ are considered and the effect is expected to be small. In fig. 4.24 the extracted polarizability is shown, applying different cuts on the invariant mass. It turns out that no significant deviation from the "central" value at $3.5m_\pi$ can be seen with the current statistical precision.

4.7 The result in context with other experiments and theory

The result obtained by 2009 data analysis is $\alpha_\pi = (2.0 \pm 0.6_{\text{stat.}} \pm 0.7_{\text{syst.}}) \times 10^{-4} \text{ fm}^3$ [1] under the assumption $\alpha_\pi = -\beta_\pi$. Comparing to previous measurements, this result is the most precise one which has been obtained for this quantity so far, c.f. fig. 4.26.

While the measurements depicted in blue, which are the dedicated experiments for pion polarizability, agree among each other within their quite large uncertainties, they are in conflict with the theoretical prediction by χPT [6], indicated as horizontal line. Including

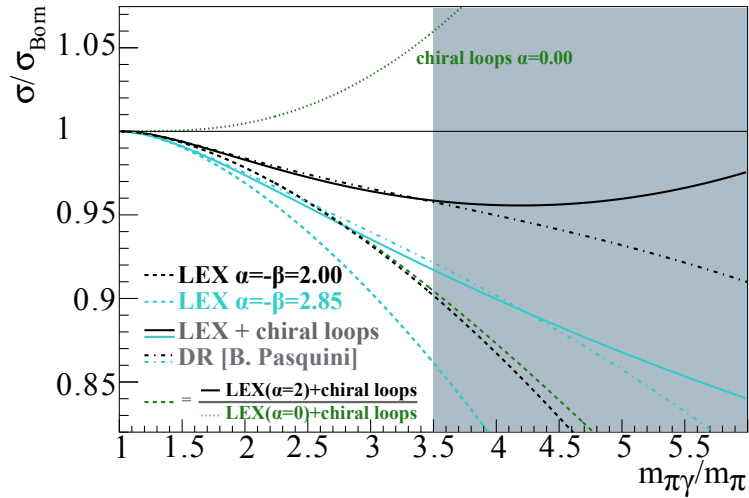


Figure 4.23 Ratio between several different cross-sections and the born cross-section for $\pi^- \text{Ni} \rightarrow \text{Ni} \pi^- \gamma$ [63]. Dashed lines show the leading order chiral expansion for two different values of α_π . The dotted green line shows the effect of chiral loops alone and the dashed green line shows the effect on the cross-section with $\alpha_\pi = 2 \times 10^{-4} \text{ fm}^3$ in case chiral loops are contributing. The solid lines show the polarizability effect for the same two polarizability values, used before in case chiral loops are included into the calculation. These have to be compared with the dotted-dashed lines which show the same quantity in a dispersive calculation given by [90].

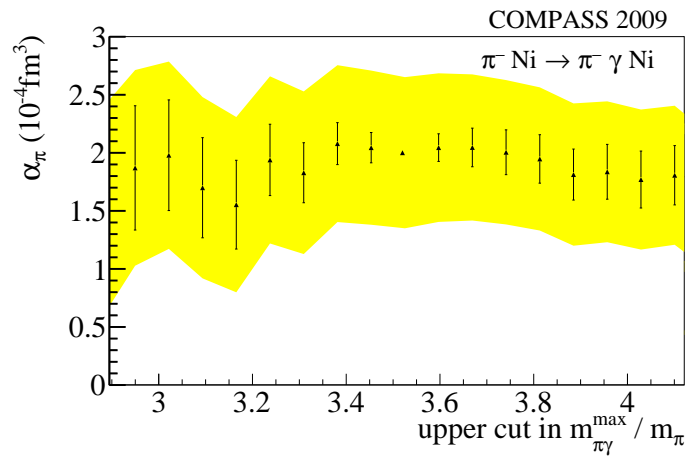


Figure 4.24 Extracted value of α_π as a function of the upper cut on the invariant mass. The absolute errors on each data-point are shown as yellow band. The error-bars are defined as the errors relative to the error on the data-point used for extracting the final result:

$$\Delta(m_{\pi\gamma}^{\text{max}}) = \sqrt{|\sigma(m_{\pi\gamma}^{\text{max}})^2 - \sigma(m_{\pi\gamma}^{\text{max}} = 3.5m_\pi)^2|}$$

4 EXTRACTION OF THE CHARGED-PION POLARIZABILITY FROM 2009 DATA

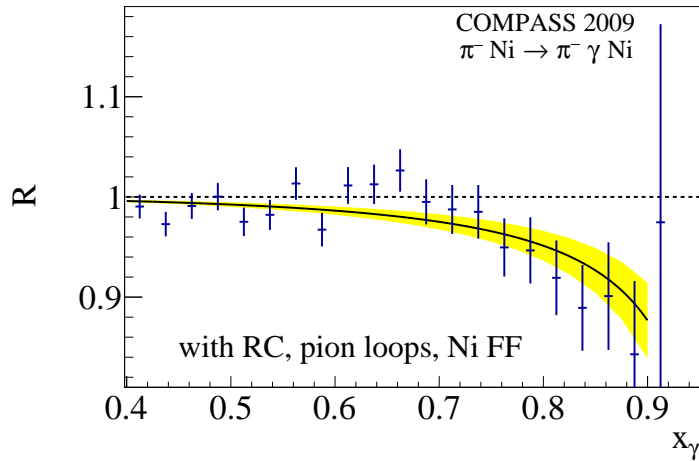


Figure 4.25 Ratio plot between data and simulation including radiative corrections, chiral loops and the contribution from the Nickel form-factor. The yellow band indicates the error on the fitted curve from which the polarizability value $\alpha_\pi = (2.0 \pm 0.6_{\text{stat.}} \pm 0.7_{\text{syst.}}) \times 10^{-4} \text{ fm}^3$ is extracted.

the measurement performed within the 2009 data analysis which is in agreement with the predicted value, also puts the world average in agreement, c.f. fig. 4.27. Having this new measurement point at hand, there is now some inconsistency with the old measurements.

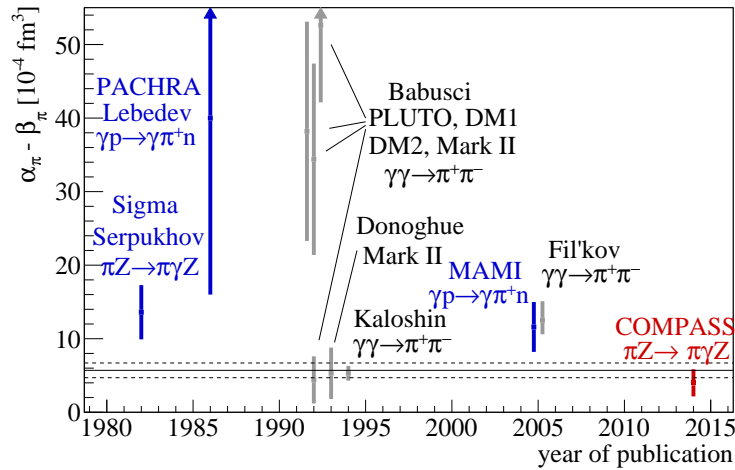


Figure 4.26 Overview over all measurements as a function of the year they were published, including COMPASS indicated in red. Other measurements used for the world average are indicated in blue and the values not used in gray. The value predicted by $\chi\text{PT}[6]$ is shown as a horizontal line.

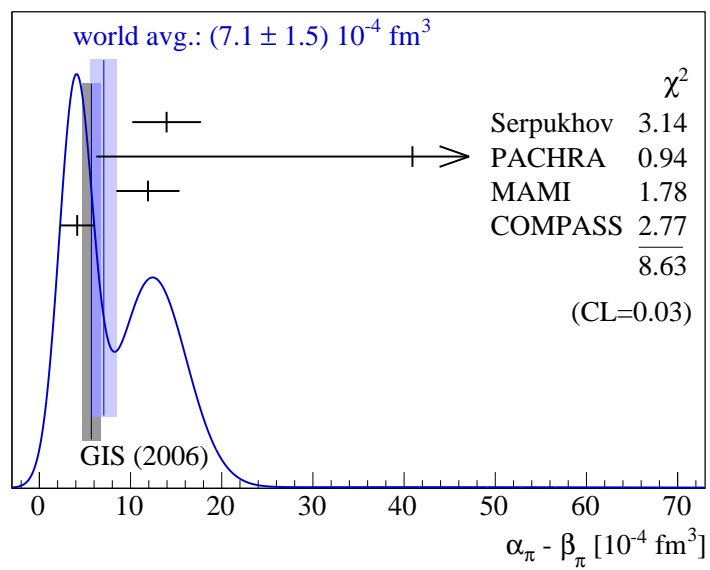


Figure 4.27 Ideogram of polarizability measurements including COMPASS. The world average is indicated in blue and the prediction by $\chi_{\text{PT}}[6]$ is shown in grey. The indicated χ^2 values are the calculated deviation from the world average for the individual measurements while the confidence level (CL) shows the bad agreement between the measurements and the world average.

Chapter 5

Preparing the analysis for the data taken in 2012

For analyzing the data taken in 2012, the knowledge obtained during the study of the data taken in 2009 is used. This new measurement has been proposed in [91]. Several calibrations which were previously applied on analysis level only for specific physics channels are transferred into the reconstruction software such that they will be of more general use. For this purpose, the software is adapted to make use of all detectors used for the analysis.

In this section, the software which is newly implemented, as well as the studies performed on the data are discussed.

5.1 CEDAR

For identifying the beam particles the CEDAR detectors are used, their principle of operation is discussed in section 2.5.1. The first attempt to use the detectors to identify particles was applied in [92]. Here the number of PMTs giving a signal was counted, a kaon is identified if one of the two detectors has signals in six or more PMTs. This method has a quite small efficiency of about 30 % because this method is only applicable in case the beam enters the detector very parallel ($\Theta_{\text{beam}} < 30 \mu\text{rad}$) to the detector axis.

In case of a real beam in which the particles are traversing the CEDARs not perfectly parallel, the photons of a specific particle type will not be focused on the diaphragm under all angles. For this case the performance of the CEDARs can be increased by taking into account the beam kinematics and calculate a likelihood for the particle ID [85]. This method has been adjusted for the 2012 data and been implemented in the official COMPASS reconstruction framework CORAL. The algorithm will be described in this section and the performance will be analyzed.

5.1.1 CEDAR reconstruction

The quantities which are used to calculate the likelihood are the tilt-direction (dX/dZ_{CE} , dY/dZ_{CE}) of the beam respectively to the CEDAR symmetry-axis and the distribution of hits in the PMTs. A PMT is considered as having a hit when the connected TDC gives a signal within a range of ± 1 TDCbin of 64 ps around the extracted T0-time. The tilt-angles can be calculated by extrapolating the beam-parameters ($dX/dZ, dY/dZ, X, Y$) at the target position to the Z-position between the CEDAR detectors. This is done using a transport matrix given by CERN [93]. As can be seen from fig. 5.1 the two CEDAR detectors are tilted slightly relatively to each other.

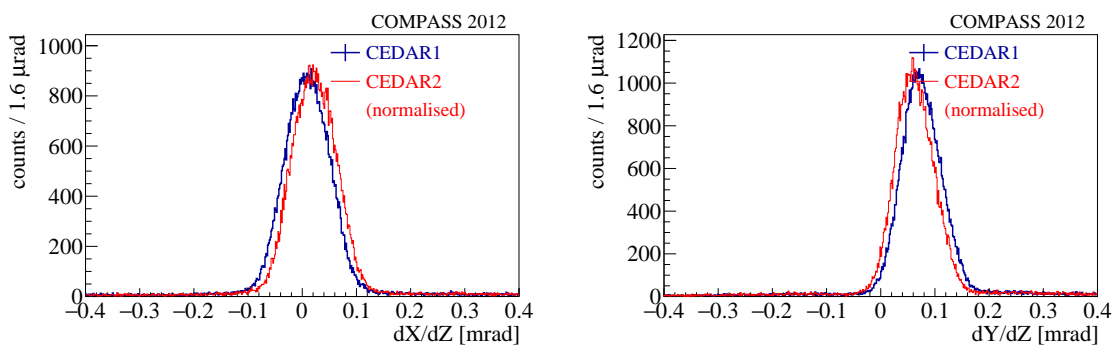


Figure 5.1 CEDAR tilt-direction: dX/dZ_{CE} left panel, dY/dZ_{CE} right panel. CE01 is shown in blue CE02 in red.

In the further analysis, the tilt offset is corrected for and the tilt-direction centered around zero.

The next step is to take advantage of the rotational symmetry of the PMTs around the beam axis. This is done by ensuring, that the PMTs are numbered consecutively around the beam axis by plotting the occupancy of each PMT as a function of the phi angle of the beam direction fig. 5.2. Here the peak corresponds to the distribution of hits created by the dominant π^- component in the beam. By performing a linear fit to the distribution, the CEDARs are rotated such that the beam direction points onto a PMT or between two PMTs. After this rotation, the PMTs can be grouped according to their position fig. 5.3 respectively to the beam direction. In case the beam points onto a certain PMT the grouping scheme shown in the left panel is used, in case it points in between two PMTs grouping scheme shown in the right panel is used.

5.1.2 Getting the event samples

For a good calibration of the CEDARs, data samples where the beam PID is well known have to be selected. It has to be ensured that the samples which are used are identified by another element than the CEDAR-trigger, otherwise a bias towards higher hit multi-

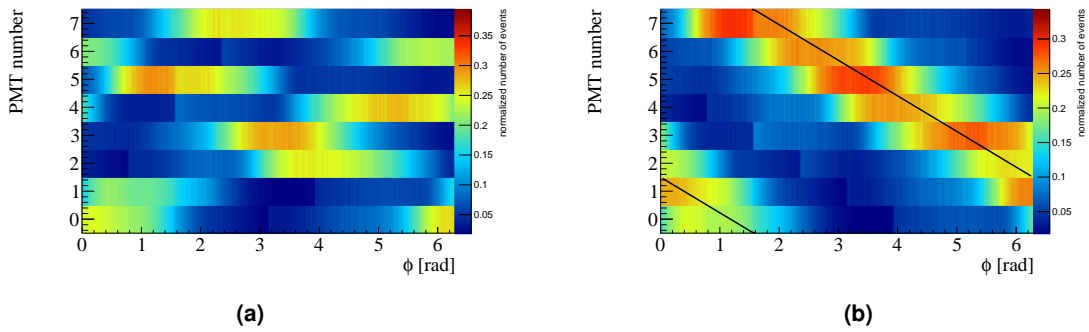


Figure 5.2 CEDAR PMT number vs. beam direction before fixing the mapping (a). After fixing the mapping (b) the distribution is diagonal in ϕ , this is indicated by a black line. Each ϕ -slice is normalized to its integral.

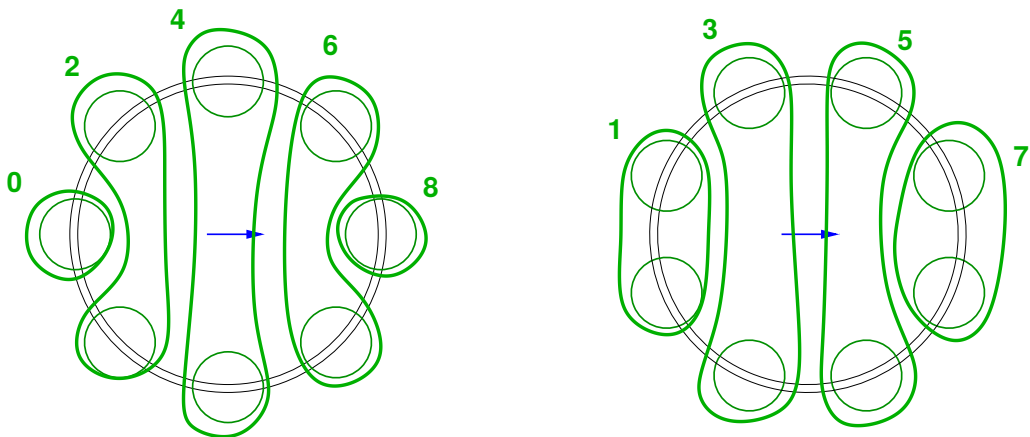


Figure 5.3 Mapping of the CEDAR PMTs in different groups G_0, G_1, \dots, G_7 as used in the text, as a function of the beam direction [85]. The blue arrow indicates the beam direction and the PMTs are shown as circles which are combined into groups of one or two PMTs depending on their position.

plicities disturbs the analysis. For this data events taken with the "Primakoff" triggers as well as with the "low-t" trigger can be used.

For generating a kaon sample this can be done by selecting events from kaon decays. These are $K^- \rightarrow \pi^- \pi^0$, $K^- \rightarrow \pi^- \pi^- \pi^+$ and $K^- \rightarrow \pi^- \pi^0 \pi^0$ [4]. The channel $K^- \rightarrow \mu^- \bar{\nu}_\mu$ has a branching of 63 % but is not usable due to the trigger constraints. Further channels are possible, but due to their small branching ratio, the gain of developing an event selection is marginal. For the calibration the first two event samples have been used. For both channels the selection is similar, the decay-vertex has to be reconstructed upstream of the Ni target. Because there is no recoiling unobserved particle, thus no momentum transfer for freely decaying particles, the measured four-momentum-transfer Q^2 has to be within resolution zero, so certainly less than $1.5 \times 10^{-3} (\text{GeV}/c)^2$. Further the momentum of the final state has to be within 8 GeV/c of the beam momentum and the mass of the final-state has to be within 10 MeV/c² of the kaon-mass of 493.7 MeV/c².

Generating a clean π^- -sample is more difficult because the decay is only possible into $\mu^- \bar{\nu}_\mu$ with a branching ratio of over 99.9 % and this decay is not very well resolved because of its limited phase-space. Having a pion content of more than 96 % in the beam allows to perform a similar selection as for the kaons decaying into the $\pi^- \pi^0 \pi^0$ final state. Here the events are not produced by the decay but by the reaction of the pions with the target material. Now the vertex is required to be inside of the target and the mass of the final state to be more than 550 MeV/c². This selection is used for calibrating the CEDARs.

For studying the CEDAR performance a cleaner π^- -sample is selected using the channel $\pi^- \rightarrow \pi^- \pi^0 \pi^0$ with the same selection criteria as described above. But in addition the outgoing π^- is tagged by the RICH. In order to clean up this sample the number of tracks in the spectrometer is required to be exactly one section 4.3.9. Because of missing calibration files for the RICH, which is filled with Nitrogen, its PID is determined manually. For this the distance of the measured Čerenkov-angle Θ_{Ch} from the Čerenkov-angle for a given particle and momentum is defined

$$(5.1) \quad d\Theta_{\text{Ch}}^i = \frac{1}{\frac{p}{\sqrt{p^2 + (m^i)^2}} \cdot n_{\text{N}}}.$$

Where $n_{\text{N}} = 1.000528$ is the refractive index of Nickel. A clean π^- -sample can be obtained by cutting on $d\Theta_{\text{Ch}}^\pi = [-1.2 \cdot 10^{-4}, 6 \cdot 10^{-6}]$ and $d\Theta_{\text{Ch}}^K > 1 \cdot 10^{-4}$.

In order to take into account the proton fraction of the beam, a sample which selects purely protons would be useful, but no sufficient selection criteria could be found.

5.1.3 Calculating the probabilities

Depending on the tilt-direction of the beam and the particle type each PMT gives a signal with a certain probability. In [94] this probability is stored in bins of dX/dZ_{CE} and dY/dZ_{CE} for each PMT. This has the disadvantage that the training-samples have to be

large in order to avoid empty bins as good as possible. Further the probability may jump from bin-to-bin due to statistical fluctuations. This can be directly seen in a non-uniform vertex distribution, fig. 5.4.

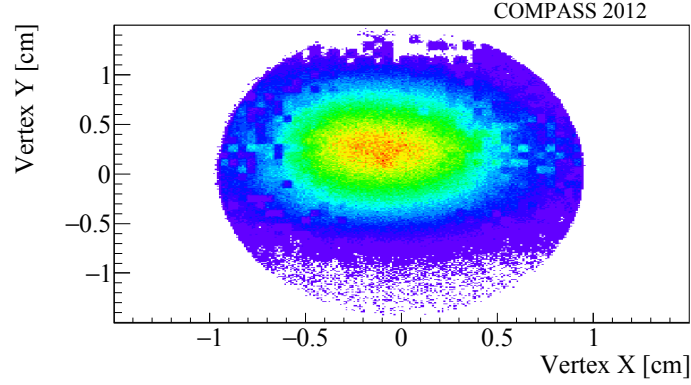


Figure 5.4 Vertex distribution with a binned CEDAR calibration, bin-by-bin fluctuations in the efficiency are visible as speckles in the XY distribution of the vertex. Data with radii bigger than 1 cm are excluded as no reasonable calibration is expected due to limited statistics.

Another method is to take advantage of the symmetry of the CEDARs and using the grouping procedure described above [85] c.f fig. 5.3. In this case there is a probability for each group to have $n = 0, 1, 2$ hits which only has a radial dependence on the tilt angle. The radius is defined as $r = \sqrt{(dX/dZ)_{CE}^2 + (dY/dZ)_{CE}^2}$. This probability in each CEDAR can be parametrized for each group g and a given particle as

$$(5.2) \quad P_g^{\pi,K}(n, r) = p_{g,0}^{\pi,K} + \sum_{i=1}^4 \text{atan} \left(\frac{r - p_{g,1,i}^{\pi,K}}{p_{g,2,i}^{\pi,K}} \right).$$

An exemplary fit for group G1 is shown in fig. 5.5 for pions on the left and for kaons on the right. It can be seen that the detector gets sensitive for the photons of a specific particle species at different radii. For radii bigger than ≈ 0.3 mrad the statistical precision is limited and the curves are not going to zero as expected from the detector geometry.

5.1.4 Getting the likelihood and calculating the PID

Having parametrized all probabilities for each CEDAR and every group a likelihood that a certain particle type gives a specific hit pattern in the CEDAR can be defined. The logarithm of this likelihood is calculated by

$$(5.3) \quad \log \mathcal{L}_{G0}^{\pi,K} = \sum_{i=0,2,4,6,8} \log P_g^{\pi,K}(n, r)$$

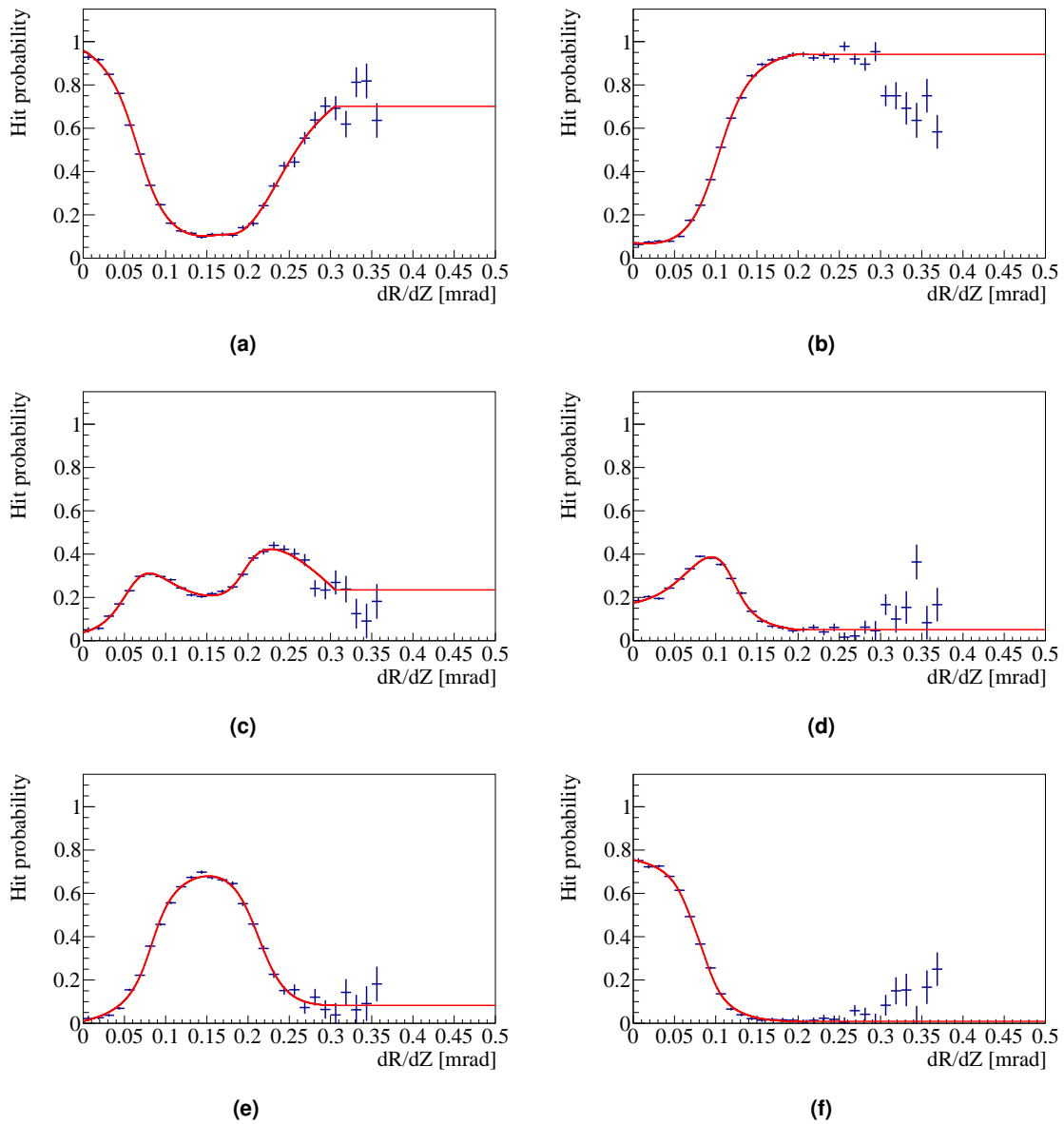


Figure 5.5 Hit probability for the PMT group G1 for pions (left) and kaons (right) as a function of the beam inclination. From top to bottom the probability for no hit, one hit and two hits is shown. The red line indicates the parametrization obtained by a fit.

Table 5.1 Truth-table for the selection of the PID given the different combinations of likelihood-decisions.

| PID CE _i ^π | PID CE _i ^K | PID CE _i |
|----------------------------------|----------------------------------|---------------------|
| π | π | π |
| π | K | Unknown |
| K | K | K |
| K | π | Unknown |
| Unknown | π | π |
| π | Unknown | π |
| Unknown | K | K |
| K | Unknown | K |
| Unknown | Unknown | Unknown |

for grouping scheme G0 and

$$(5.4) \quad \log \mathcal{L}_{G1}^{\pi,K} = \sum_{i=1,3,5,7} \log P_g^{\pi,K}(n, r)$$

for grouping scheme G1, respectively. Plotting the likelihood given by the pion parametrization as a function of the radius is exemplary shown in fig. 5.6 (a,c) for a pion and a kaon sample, respectively. These distributions are normalized to each other and the asymmetry

$$(5.5) \quad \frac{\log L_{\pi}^{\pi} - \log L_{\pi}^K}{\log L_{\pi}^{\pi} + \log L_{\pi}^K}$$

is calculated, fig. 5.6 (e). The naming scheme is given in the format $\log L_{\text{CEDAR tag}}^{\text{particle sample}}$. In this picture regions where kaons can be clearly defined have values close to -1 and pions are identified by values close to +1. An empirical parametrization of the transition region is applied which separates the picture into three regions, one for kaons, one for pions and an intermediate one which does not allow a clean distinction. The same approach is performed for the likelihood given by the kaon parametrization, fig. 5.6 (b,d,f).

The final decision for the particle type is made by combining this information and using both CEDARs. Table 5.1 shows which combinations lead to which decision. The same logic is applied to combine the two different detectors.

The algorithm is fully implemented in the COMPASS reconstruction and provides access to the PID for the analyzer. For the case that a different purity or a different efficiency is desired the user may scale the regions which give a certain PID.

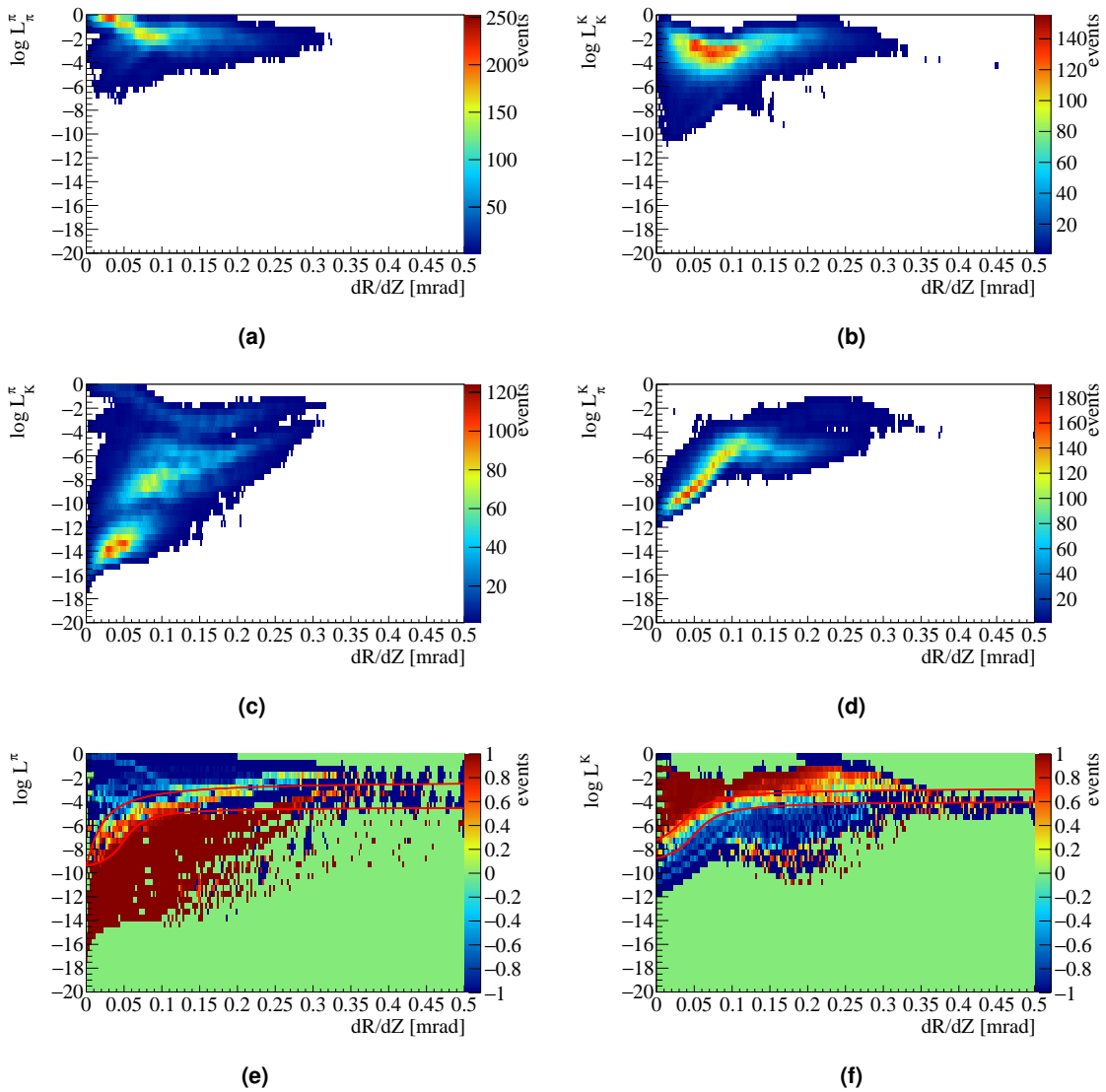


Figure 5.6 pionPiSample, KKsample, pionKsample, kaonPsample

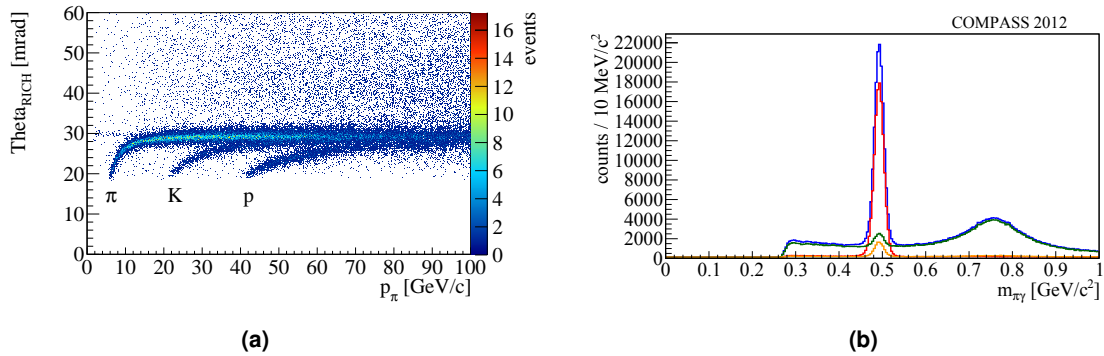


Figure 5.7 Reconstructed Čerenkov-angle as a function of the particle momentum(a). For events from the reaction $\pi^- \text{Ni} \rightarrow \pi^- \pi^0 \pi^0 \text{Ni}$ pions are selected by manually cutting on the pion-band which gives a clean pion sample. In (b) the invariant mass from the $\pi^- \pi^0$ final-state is shown in blue. The yellow curve shows events not tagged by the CEDARs while the green and red curves show events where the beam particle is tagged as pion or kaon, respectively.

5.2 Performance

Using this procedure the data can be analyzed using pure samples from kaon decay or from the reaction $\pi^- \text{Ni} \rightarrow \pi^- \pi^0 \pi^0 \text{Ni}$ with the final-state charged particle tagged as pion by the RICH applying this procedure the efficiency ϵ and the miss-identification probability η can be determined as shown in eq. 5.6. Especially the important parameter of kaon suppression is given by $\epsilon_{\pi\pi}$ is above 92 %.

5.2.1 Stability and application to other years

The calibration procedure has been applied to 2.5 weeks of data taking in 2009 and to several months in 2012. As can be seen from fig. 5.8, the temperature measured at the center of e.g. CEDAR1 is not constant over time. This leads to fluctuations in the ratio of pressure and temperature and thus the density inside the detectors. Every deviation in this quantity leads to a modified refractive index and a slightly different Čerenkov-angle, this makes it necessary to regulate the pressure inside the CEDARs. While in the years 2008 and 2009 the deviation was monitored and a manual intervention was necessary when the pre-programmed limits were exceeded an automatic procedure has been established in the beginning of 2012. The difference between these two procedures can be seen from the step-like structure in fig. 5.8(a). The temperature is shown for the upstream side of the detector, the resulting density is a function of the temperature gradient parallel to the detector axis.

In order to adapt the method for the use with the data taken in 2008 [95] the method using calibration samples is not applicable because no trigger was present giving an unbiased kaon sample. Currently a method is under investigation where the likelihoods can be

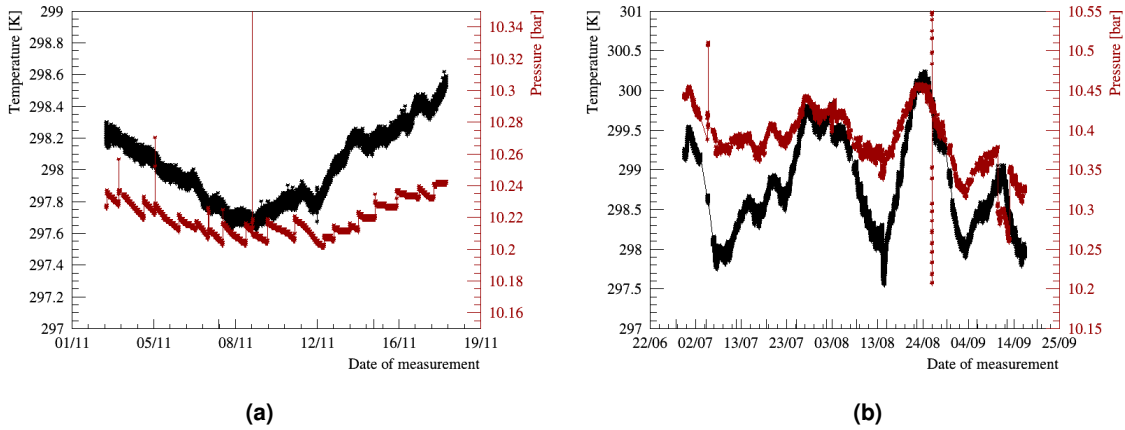


Figure 5.8 Temperature (black) and Pressure variations (red) in CEDAR 1. In (a) the pressure was manually adjusted leading to a step-like structure. In 2012 (b) this adjustment was performed automatically and the structure is more smooth.

calculated from purely geometric considerations using a pion sample as reference. It further is found that the alignment of the detectors has a certain time-dependence. It has to be checked if this is also true for the data taken in 2012.

In 2009, data were taken using a positive hadron beam consisting of 78.3 % protons [44]. In this case, one CEDAR was set to give a signal in case a proton passing through, and one CEDAR giving a signal in case a pion is passing through. Using the likelihood based algorithm, described above, results in a distribution like shown in fig. 5.9. The likelihood splits up into clearly separated bands corresponding to different multiplicities and thus the efficiency of the two algorithms is similar in case the same multiplicity is selected.

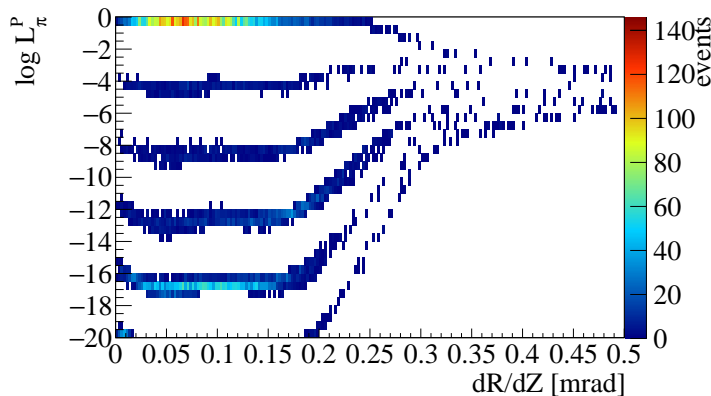


Figure 5.9 Likelihood for tagging a pion as a proton in the 2012 data using a positive hadron beam with the CEDAR set up to detect protons. The likelihood gets split up into clean band corresponding to different multiplicities.

5.2.2 Determination of the beam composition

The beam composition given in [44] is determined by using data given by CERN [96] which is then extrapolated to the COMPASS target using the decay of the particles. This is only an approximation because the particles have different cross-sections and thus the loss by interaction has to be considered.

One possibility to measure the beam composition is to determine the efficiencies and purities for the CEDARs and then tagging events which are triggered by the random trigger. Considering only three particle species in the beam, π , K, U. Where the unidentified particles U are assumed to be protons. Because the tagging probability for protons is not known a fraction of 0.5 % mixing purely into the pion fraction is assumed.

$$(5.6) \quad \overleftrightarrow{\epsilon}_{\text{CEDAR}} = \begin{pmatrix} \epsilon_{\pi\pi} & \eta_{\pi K} & \eta_{\pi U} \\ \eta_{K\pi} & \epsilon_{KK} & \eta_{KU} \\ \eta_{U\pi} & \eta_{UK} & \epsilon_{UU} \end{pmatrix} = \begin{pmatrix} 92\% & 0.5\% & 7.5\% \\ 6.6\% & 86.5\% & 6.9\% \\ ? & ? & ? \end{pmatrix}.$$

An unbiased beam sample can be obtained by analyzing two run runs which were triggered by the random trigger, only. In this runs the CEDARs tagged a beam composition of $N_{\pi}^t=91.2\%$, $N_K^t=3.0\%$ and $N_U^t=5.8\%$. The true beam composition can be calculated by solving the equation $\vec{N}^t = \overleftrightarrow{\epsilon}_{\text{CEDAR}} \cdot \vec{N}$. Using this knowledge the kaon fraction in the beam tends to be 2.8 % in contrast to the 2.4 % given in [44]. Currently a more elaborate analysis is performed [67] in which the contributions from other particles like electron are taken into account.

Another, maybe less precise possibility is to look at the PMT of one CEDAR which is not expected to give any hit for pions. If one looks at the distribution for beam-gradients below 0.15 mrad the probability for no hit in this PMT starts to deviate from one with a similar shape as probability for a kaon to give at least a hit in this PMT, fig. 5.10 (a). By scaling the kaon distribution in a way that it matches the pion distribution the optimal scaling is found for $N_K/N_{\pi} \approx 2.6\%$.

5.3 Beam momentum

In order to calculate the four-momentum transfer Q^2 c.f. section 1.5, knowledge of the momenta of all incoming and outgoing particles is necessary. Analysis where the four-momentum transfer is above $0.1 (\text{GeV}/c)^2$ e.g. [97, 40] the beam-energy is calculated from the momenta of the outgoing particles, assuming an exclusive reaction. In case of very low momentum transfers the resolution is very crucial and the effect of the resolution of the electromagnetic calorimeter is the worst-known variable. In case of muon beam the beam-momentum station BMS is installed into the COMPASS beam-line which is able to directly measure the beam momentum. For hadron beams this device is removed in order to reduce the amount of material in the beam line.

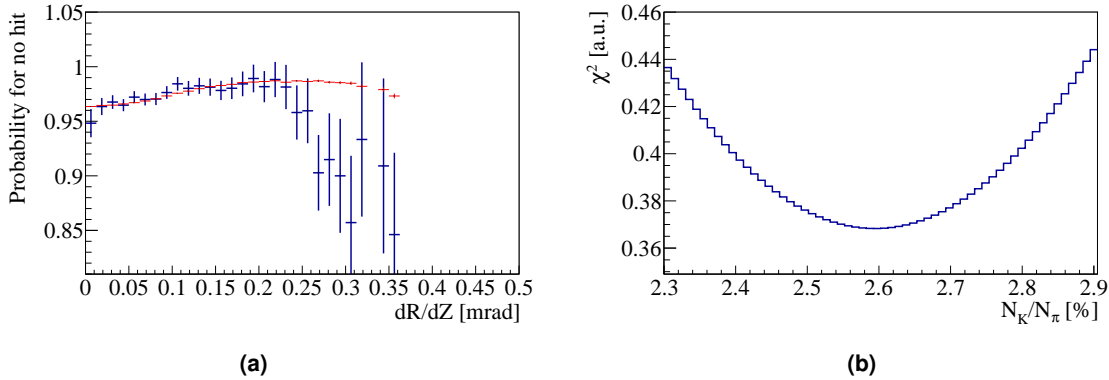


Figure 5.10 Distribution for no-hit probability in PMT group G6, c.f. fig. 5.3, (a) in case of the pion sample (blue). In red the distribution as it would be expected from a ratio $N_K/N_\pi \approx 2.6\%$ is shown. In (b) the χ^2 distribution when minimizing the difference between the two histograms in (a) is shown.

As the beam line has fixed magnetic parameters its transport properties are slightly different for each particle momentum. This leads to a dependence of the beam-momentum on the spatial-coordinates of the beam at the COMPASS target which can be exploited for constraining the beam energy. In [76] a neuronal network was trained in order to get the correlation of the beam-energy E with the coordinates (x, y, dx, dy) for the 2009 Primakoff-data. Here dx and dy stand for the beam gradient in x and y - direction, respectively. The computation of the beam-energy using this neuronal network took about 1 ms per event. This caveat can be avoided by parametrizing the neuronal network with a polynomial with 441 free parameters, where for each variable terms up to 5th order are used. The data-set which is used for this extraction is based on the reaction $\pi^- \text{Ni} \rightarrow \text{Ni} \pi^- \pi^- \pi^+$ at low momentum-transfers $Q^2 < 0.2 \text{ (GeV}/c)^2$. For studying the beam-energy dependence in the 2012 data-set the same selection has been applied to one week of data-taking (W28) and in total an amount of about 700 000 events have been used for this analysis.

As the determination of the parametrization of the polynomial is based on the result of the neuronal network, which has to be trained in a first step, the computational time to determine these parameters is significant. A more efficient way of determining the parameters is to consider the task as a linear problem [98]. In this approach the difference between the beam-energy measured by the final-state particles $E_{\text{beam}}^{\text{meas.}}$ and the beam energy given by the parametrization can be described by the χ^2 -function

$$(5.7) \quad \chi^2 = \sum_{\text{events}} \left(E_{\text{beam}}^{\text{meas.}} - E_{\text{beam}}^{\text{calc.}} \right)^2 = \sum_{\text{events}} \left(E_{\text{beam}}^{\text{meas.}} - \sum_{i=0}^N (p_i \cdot X_i) \right)^2.$$

Here the X_i describe the 441 linear weights of the polynomial $p_i = x^{n_x} y^{n_y} dx^{n_{dx}} dy^{n_{dy}}$ with exponents in the range 0 to 4. An optimal parametrization is found if this χ^2 -function is

minimal or the partial derivative in each X_j is zero,

$$(5.8) \quad \frac{\partial \chi^2}{\partial X_j} = \sum_{\text{events}} 2 \cdot E_{\text{beam}}^{\text{meas.}} \cdot X_j - 2 \cdot \left(\sum_{i=0}^N p_i \cdot X_i \cdot X_j \right) = 0.$$

This equation can be rewritten in a matrix form eq. 5.9 and solved by inverting the matrix. In this way the computational effort to determine the parameters is, since the matrix inversion time is negligible, reduced to the time spent for parsing all events.

$$(5.9) \quad \sum_{\text{events}} E_{\text{beam}}^{\text{meas.}} \cdot \begin{pmatrix} X_0 \\ \vdots \\ X_N \end{pmatrix} = \sum_{\text{events}} \begin{pmatrix} X_0 \cdot X_0 & \dots & X_0 \cdot X_N \\ \vdots & \ddots & \vdots \\ X_N \cdot X_0 & \dots & X_N \cdot X_N \end{pmatrix} \cdot \begin{pmatrix} p_0 \\ \vdots \\ p_N \end{pmatrix}$$

In order to increase the numerical precision in the calculation, an approximate leading term of the parametrization of 191 GeV is subtracted as well as a dominant linear term in dY which is apparent in fig. 5.12 (g). In fig. 5.12 the leading-order contributions of the individual coordinates are shown. On the left panels the summed energy of the final-state particles leads to an expected smearing due to resolution. On the right side the correlation from the polynomial parametrization shows narrow distributions without background from non-exclusive events. In addition, hints to slightly different kinematic components, which can be extracted with this method are found in the beam correlations, c.f. fig. 5.12 (h).

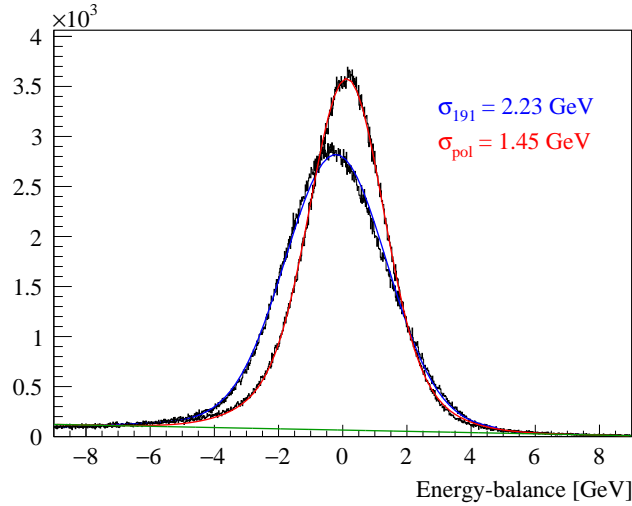


Figure 5.11 Energy-balance distribution for the 3- π final state. The histograms show the total energy of the final-state with a value of 191 GeV subtracted (blue) and the result of the polynomial parametrization subtracted (red). Both histograms are fitted with a sum of two Gaussians plus an arctan-function describing the background. The values extracted as σ are the RMS-widths when setting the background term, shown in green, to zero.

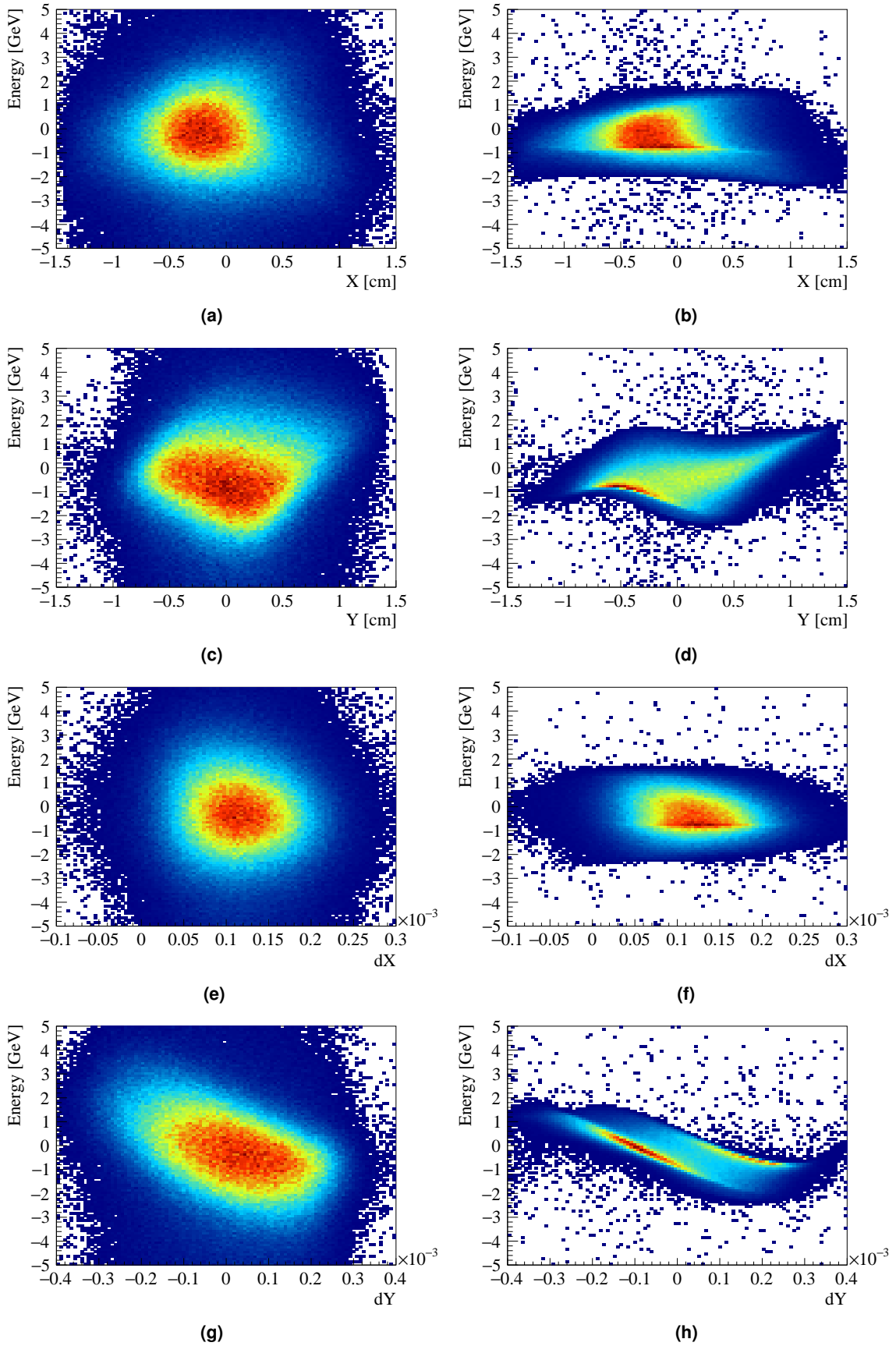


Figure 5.12 Dependence of the beam-energy on the spatial beam-parameters. On the left panels the energy is determined from the $\pi^-\pi^-\pi^+$ final-state. On the right the beam-energy is given by the polynomial parametrization of the beam.

Looking at fig. 5.11 it can be seen that the width of the energy-balance for the $\pi^-\pi^-\pi^+$ final-state is $\sigma_{191} = 2.23$ GeV in case a constant beam momentum is assumed. This width is significantly reduced to $\sigma_{\text{pol}} = 1.45$ GeV in case the energy is derived from the spatial beam-parameters. When trying to apply this approach to the μ^- -beam, no correlations can be found. This can be explained by the fact that the muons result from decaying pions in the beam line and the decay washes out the correlations.

This parametrization has been implemented in the CORAL reconstruction framework after the first production of the 2012 data has been completed, and thus it has to be applied at analysis level for the first production.

5.4 ECAL calibration

A full understanding of the calorimeter performance is crucial for the extraction of physics of reactions containing photons in the final state. The energy resolution, which also depends on the deposited energy, reflects directly the number of photons wrongly contributing to the exclusivity peak. And the position resolution influences strongly the resolution in the four-momentum transfer Q^2 .

In this chapter the calibrations applied for COMPASS data are discussed. Within this thesis additional studies have been performed and possible improvements are discussed.

5.4.1 Electron calibration

An electron beam is used to get the initial energy calibration coefficients. The procedure to get these values is discussed in section 2.4. The result is further refined by other calibrations and thus no further investigation is performed here.

5.4.2 LED calibration

The LED calibration system described in section 2.4 is intended to compensate time-dependent fluctuations of the calorimeter response. The precision depends strongly on the amplitudes obtained for the LED signal. In case the LED amplitudes are below 100 ADCcounts for a given cell, which are monitored with a precision of 1 ADCcount only provide a correction which takes into account fluctuations in the order of $(100/\text{amplitude})\%$. Because in addition to the calibration signal there is also noise on the measurement, averaging over many samples gets a slightly improved resolution.

In fig. 5.13 (a) the variation of the average deviation of the measured π^0 mass from the real value [4] for the most central is given as a function of the run number within one week of data taking. It can be seen that there are strong oscillations which may be explained by a thermal influence on the detector given by day-night fluctuations of the temperature.

In fig. 5.13 (b) the amplitude distribution of the LED system for the same cell is shown. Where some similarities in the shape may be seen but in general the strength of the fluctuations can not be reproduced. In fig. 5.13 (c) the LED amplitude distribution for one lead-glass cell is shown. The extracted correction seems to follow the trend of the π^0 -signal more precisely.

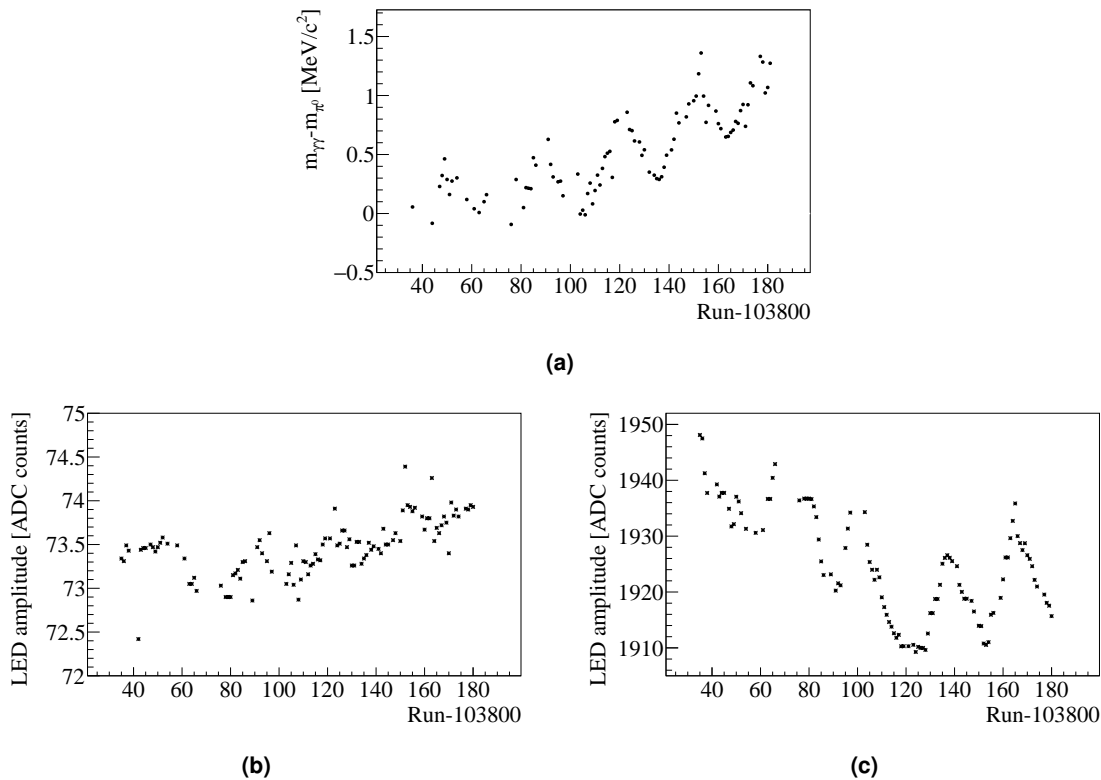


Figure 5.13 Deviation of the π^0 mass from the PDG value as function of the run number. The plot indicates the fluctuations within one week of data-taking. The fluctuations can be explained by thermal differences as expected from day-night changes.

Without compensation, the time-dependence reflects also to the energy balance of the polarizability data, fig. 5.33, where the ΔE peak slightly shifts depending on the week of data-taking. For the most central cells it is possible to compensate for this effect by taking into account the fluctuations of the measured π^0 -mass. For more peripheral cells this is not possible, because the amount of π^0 s is not sufficient to extract a time dependent calibration. The same holds for the muon data. As a result this additional calibration is currently not applied.

The time of the signal is extracted by selecting the maximum of the derivative. A more precise value is determined by using the Newton algorithm to find the absolute maximum of the derivative of the unbinned distribution. This has the advantage that the time is always extracted at the point of the steepest slope and not at the first slope which is detected by the constant-fraction discriminator.

5.4.3 New feature extraction

The standard feature extraction in the COMPASS reconstruction is performed similarly to the constant fraction discriminator applied in the trigger logic used in hardware, described in section 3.5. While its performance in terms of resolution is good it has the disadvantage that it is sensitive to any rising edge found in the data. In fig. 5.14 an exemplary pulse corresponding to noise can be seen, here the ADC is in underflow with measuring amplitudes around zero and then slowly recovering to the baseline value of 50. The implementation using the CFD would extract an amplitude of around 50 in this case. In ECAL2 additional care has been taken to repair cells where significant amount of noise is seen while in ECAL1 this is not the case. In order to reduce the noise on both detectors a new algorithm is implemented to the COMPASS reconstruction.

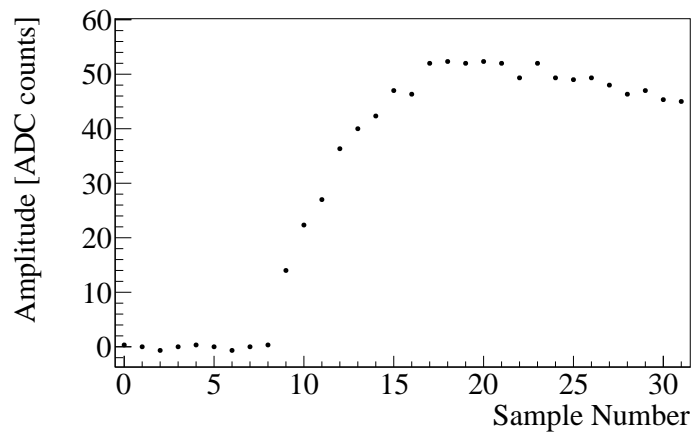


Figure 5.14 Example of a noise pulse. Here a discharged cell slowly recovers up to the nominal baseline value of 50 ADCcounts.

This algorithm makes use of the fact that the pulse shape only depends on the detector cell itself and the electronics attached to it. The actual interaction is only represented by the amplitude and the time of the signal. Using a FFT¹ based algorithm allows to analyze the components of the pulse based on the frequency where for instance the lowest order component represents the baseline. In order to remove high-frequency noise a low-pass filter can be applied allowing only the lowest order fourier-components to be considered for reconstructing the signal. An exemplary pulse is shown in fig. 5.15 where the lowest eight fourier-components have been used. Initially it is not obvious how many fourier-components are needed in order to reconstruct the signal but it can be seen from fig. 5.18 that at least seven components are necessary in order to reconstruct the amplitude.

Looking at the derivative of the reconstructed pulse, fig. 5.16, the shape can be approximated by a parabola centered around the maximum slope of the pulse. The amplitude of the signal is reconstructed by integrating this derivative between the expected maximum

¹fast fourier transform

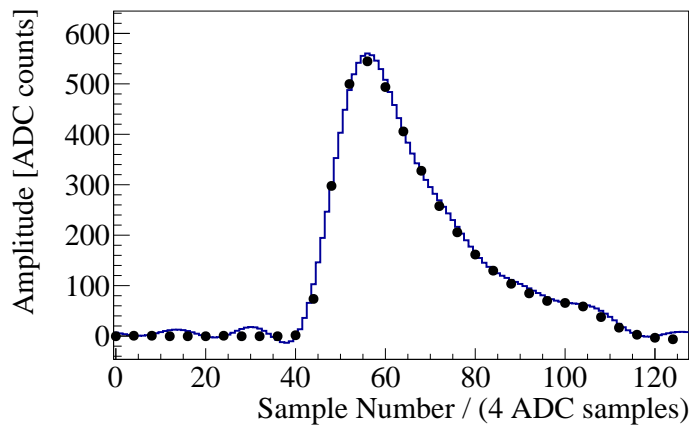


Figure 5.15 Example pulse from ECAL2. The measured data points are shown as black dots. The pulse shape reconstructed from eight fourier-components is shown as blue line. The fourier transformation allows to effectively consider the pulse as if it has more samples. In this case the number of samples is visualized with a reduced spacing by a factor of four.

and the minimum of the pulse. Obviously the boundary values correspond to the position where the derivative crosses the zero-line. The amplitude of pulses which do not correspond to the expected shape are penalized by the difference to the parabolic approximation. In case of the example given in fig. 5.14 the reconstructed amplitude is reduced to about 11 ADCcounts showing the power of this ansatz where otherwise an amplitude of more than 50 ADCcounts would be extracted.

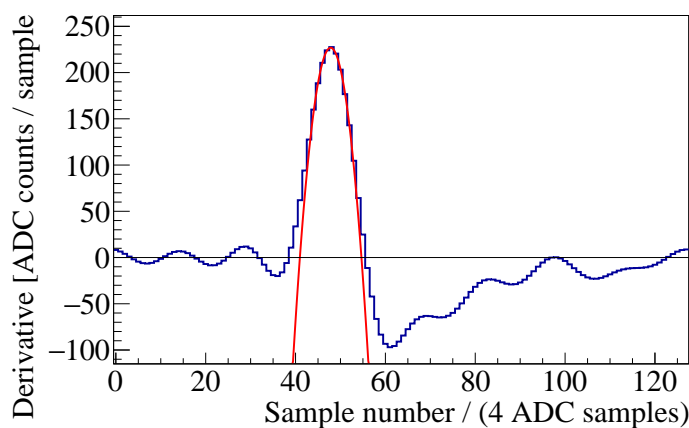


Figure 5.16 Example of the derivative of the pulse extracted with the FFT based algorithm on ECAL2. The blue line shows the derivative with an increased number of "samples" by a factor of four. The red line indicates the parabola with which the shape is approximated.

It is important to consider the response of each individual cell. This can be seen from fig. 5.17 where the parabola width is shown for many pulses on all cells. It can be seen

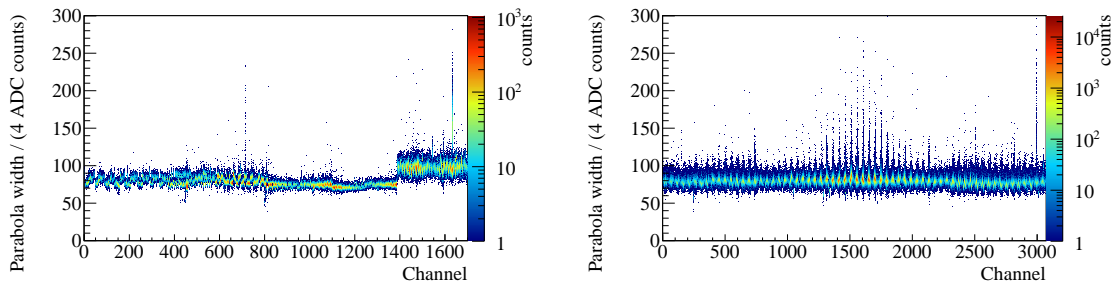


Figure 5.17 Width of the parabola assumption for the derivative of the FFT based amplitude as a function of the channel number. In (a) the distribution is shown for ECAL1 and a strong dependence on the cell type is visible. In (b) the distribution is shown for ECAL2 here a more uniform distribution is extracted.

that a calibration is necessary taking into account the cell-by-cell fluctuations. Further it is found that the extracted amplitude is about 3% smaller than the amplitude measured without this algorithm. This effect has to be taken into account by the calibration.

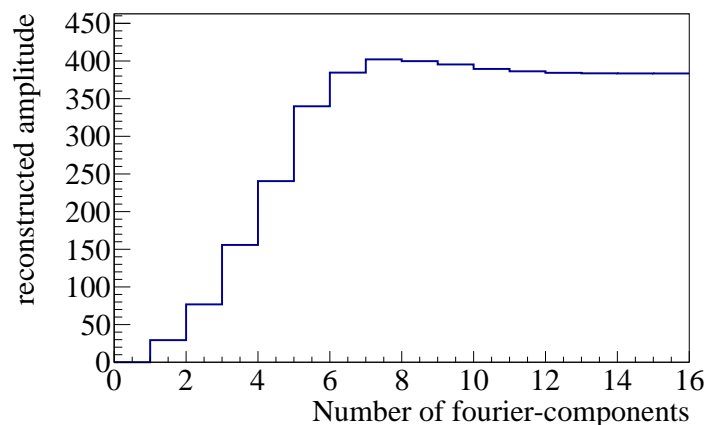


Figure 5.18 Reconstructed amplitude as function of the number of fourier components used. The plot has been extracted for one exemplary pule with an amplitude of 415 ADCcounts. The amplitude is maximum between seven and eight components.

5.4.4 π^0 -calibration

After all calibrations described above are applied, the detector can be calibrated more precisely taking reconstructed π^0 s and calibrating the detector in a way that the mass is reconstructed at the physical value [99]. This is done on a cell-by-cell level for both calorimeters. Because the squared, reconstructed $\gamma\gamma$ mass depends linearly on the energy

of the photon a correction factor α can be calculated by

$$(5.10) \quad \alpha = \frac{1}{(1 + \Delta)^2},$$

where Δ represents the relative deviation of from the true π^0 -mass. Because obviously the reconstructed mass does not only depend on the energy of the cell for which the correction is obtained, but also on the average of the deviations of the energies of all other cells, the procedure is repeated iteratively until no further improvement can be achieved.

In case of the central cells of ECAL2, there are significantly many π^0 s to obtain the corrections not only in one dimension but differentially as a function of energy as well as the time within a spill. The dependence on the time in spill is an effect induced by the high occupancy caused by a hadron beam, and therefore it is not used in case of the measurement with a muon beam. As discussed in section 5.4.2 an additional calibration as a function of the run number should be considered.

In case of the data taken in 2012 with the new reconstruction algorithm applied, the average reconstructed mass is smaller than the π^0 -mass. This leads to the effect that for small energies the correction factor usually is the biggest. Because the calibrations are applied on cell and not on cluster level this leads to an too big correction to the cluster energies, fig. 5.19. This problem is solved by producing a calibration and then running the reconstruction again. This has to be repeated until the final calibration is reached.

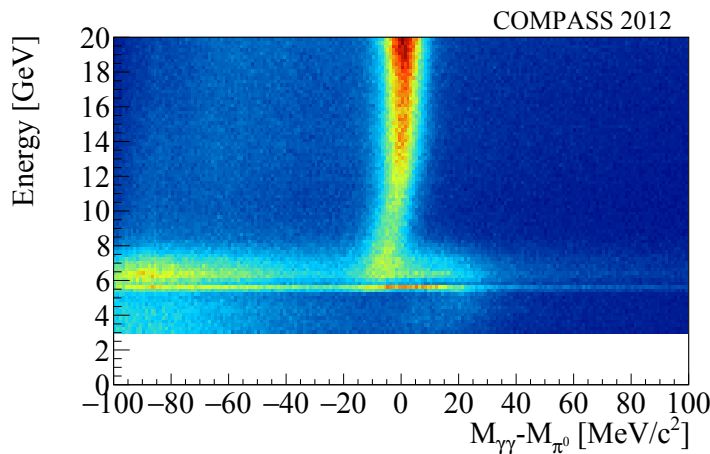


Figure 5.19 Energy dependent deviation of the reconstructed mass from the π^0 -mass after one iteration of π^0 -calibration and re-performing the cluster-reconstruction. A non-linear dependence and an enhancement around 6 GeV.

In fig. 5.19 another problem can be seen, in case the calibration is considered independently for every energy bin, the procedure may not converge in the desired way. In the case seen in this plot the calibration artificially enhances the energy bin around 6 GeV.

In fig. 5.20 a solution is presented, where. The correction coefficients extracted individu-

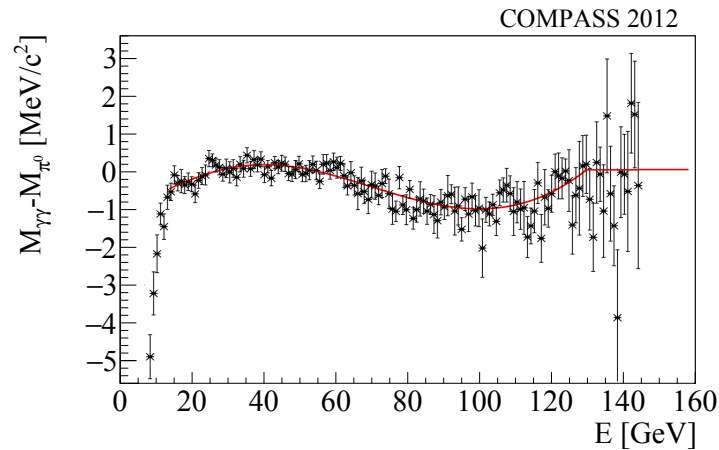


Figure 5.20 Fitted energy dependence of the π^0 -mass using an interpolating function. Bin-by-bin fluctuations are removed by this function. In region with a strong energy dependence the function is not used.

ally in every energy bin are smoothed by an interpolating function. It has to be checked that the fit interpolates the energy dependence correctly and there are no regions with a too steep dependence. This has to be done mostly manually, because the cells behave too differently and no general function can be found. Effects of this improved energy-dependent calibration can be seen in fig. 5.21. In (a) the improvement achieved by using the interpolation is seen, here the black line shows how the correction would look like without using the interpolation. In (b) a similar picture is shown over the full energy range. The last bins have to be carefully checked because here, the function may diverge due to the small number of events.

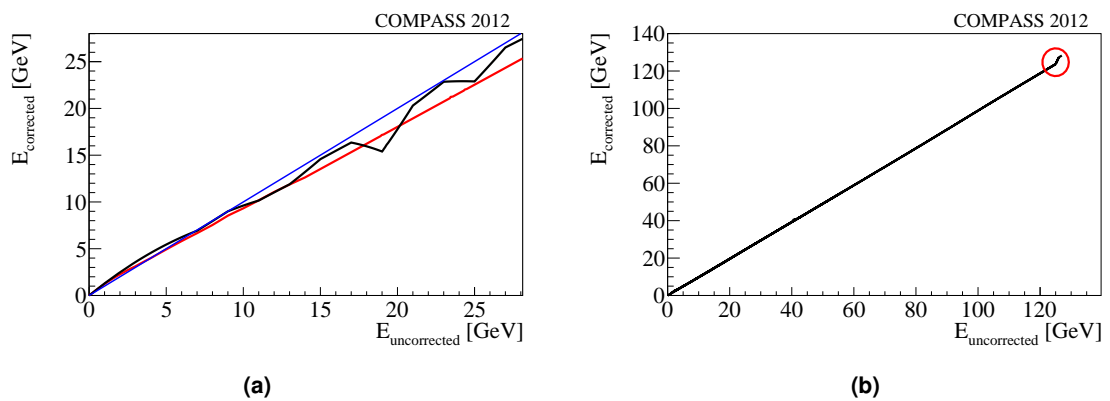


Figure 5.21 Misbehaving energy dependent calibration coefficients. In (a), bin by bin fluctuations are seen while in (b) problems with the end-point of the fit become visible.

5.4.5 Energy correction dependent on the position in the cell

The Shashlik cells used in the central region of ECAL2 have a non-uniform internal structure, c.f. section 2.4.1. This fact has to be considered when looking at the signal amplitude which is measured for a photon with given energy. In case a photon hits the calorimeter close to one of the steel rods a part of the shower is absorbed by this material and the measured energy is too small, fig. 5.22 (b). In case the impact is close to one of the light-guides, the photon detection efficiency is slightly improved. In case of small photon energies the measured energy is higher close to the cell border probably caused by the distribution of the shower energy into more detector cells, fig. 5.22 (a).

This effect appears in the full energy range and different sources for calibration may be used. For energies above 30 GeV the muon data is used. Here the mean value of the energy balance of the reaction $\mu^- \text{Ni} \rightarrow \text{Ni} \mu^- \gamma$ is the main source for determining the coefficients. Hereby one has to rely on the fact that no momentum offsets are measured by the BMS or the COMPASS tracking system.

For lower photon energies this procedure can not be used because there is no trigger for these events. Another approach is to use the π^0 -mass as described in section 5.4.4. Here it is of advantage that the calibration averaged over the cell is already correct. Thus one iteration is enough to extract the position-dependent correction.

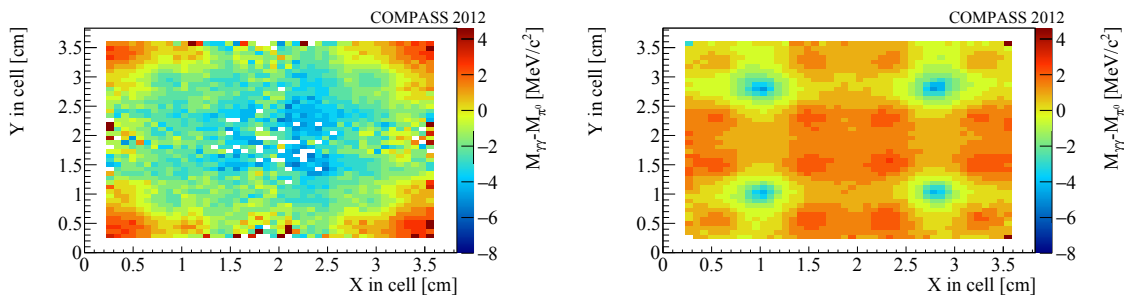


Figure 5.22 Dependence of the reconstructed π^0 -mass as a function of the reconstructed position inside a cell. In (a) a energy bin between 10 and 20 GeV is shown; in this case the mass tends to be reconstructed to higher values when the impact is close to the cell border. In (b) a energy bin between 60 and 70 GeV shows a more complex structure, around the four holding rods the mass is reconstructed at small values while around the light-guides it is reconstructed at higher masses.

The energy dependence as well as the position dependence of this calibration is extracted and manually described by a function connecting the full energy range of the detector. This function is stored into the usual COMPASS calibration database and code has been developed which applies this correction already at reconstruction level. This is an improvement to the approach used for the 2009 data [29] where the calibration was applied at analysis level and its parameters were only extracted for energies above 50 GeV. The impact of this calibration can be seen in fig. 5.23.

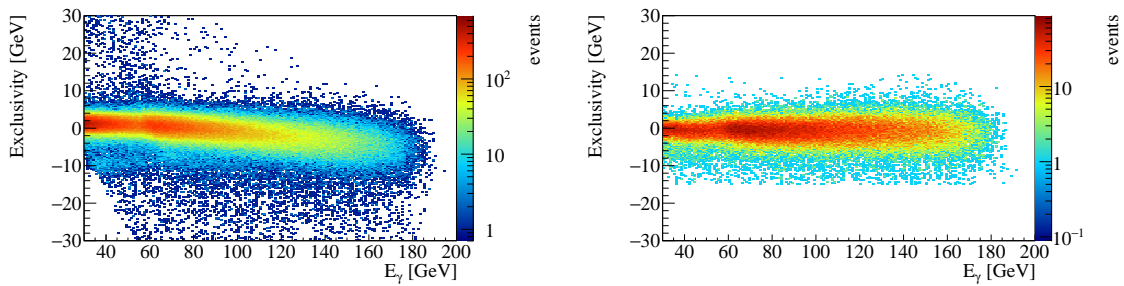


Figure 5.23 Energy dependence of the exclusivity before correction (a) and after the position dependent energy correction is applied (b).

5.4.6 Dependence of the reconstructed cluster position on the position inside a cell

A similar effect as described above can be seen if one studies the reconstructed cluster position as a function of the position inside a cell. Even in case of simulation an S-like structure can be seen fig. 5.24.

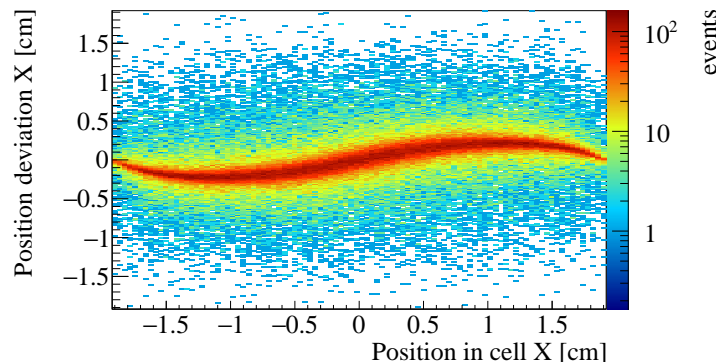


Figure 5.24 Position deviation from the true position of a calorimeter cluster in X-direction as a function of the true position extracted from Monte Carlo data.

This has been already seen [100] and a correction based on a third-order polynomial is applied. This is not done in the current reconstruction of the data taken in 2012 because this polynomial has the problem that it is extracted from reconstructed electrons extrapolated to the detector surface. This leads to the effect that the corrections in horizontal and vertical direction are different e.g. due to the different impact angle on the calorimeter. A further problem is that the polynomial which is currently applied is not continuous at the cell boundary.

The position of the cluster has an impact on the reconstructed four-momentum transfer and thus a correctly determined correction may improve the separation of the signal from the background. In fig. 5.25 this effect can be seen on Monte Carlo-level. One pos-

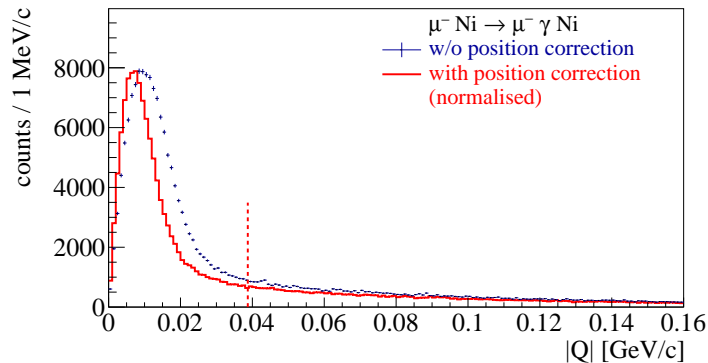


Figure 5.25 Simulated data for $\mu^- \text{Ni} \rightarrow \text{Ni} \mu^- \gamma$ reconstructed without the position dependent position correction applied (red) and with the correction active (blue). Enabling the correction leads to a much sharper peak structure.

sibility to extract the position correction would be to minimize the reconstructed four-momentum transfer as a function of the reconstructed position inside one cell. The correction extracted by this approach then can be parametrized by a function which considers the correct boundary conditions. This was studied close to finishing this thesis and thus could not be investigated in more detail.

5.5 Alignment

The alignment of the individual planes of the tracking detectors is crucial in order to perform a correct track reconstruction. In COMPASS the alignment is performed on special runs with muon beam. These data are taken with a trigger mix consisting of the beam-trigger, the halo-trigger and the veto-inner trigger. This is done in order to record events with beam particles illuminating most of the spectrometer. Furthermore, two runs are taken, one where the magnetic fields of the spectrometer magnets is switched off and one where this magnetic fields are on. The reason for this is that on the one hand some detectors may slightly move in the magnetic field while for other detectors like GEMs the magnetic field modifies the response. The algorithm used in COMPASS is adopted from the one described in [101]. The alignment procedure is done in several iterations and in every iteration different sets of parameters are left free, the initial alignment on period-by-period basis has been performed in [43].

During the analysis of the 2009 data it was figured out that the silicon-microstrip detectors need an additional alignment step [83]. The movement due to temperature variations of these detectors is in the order of the detector resolution and thus a run-by-run based alignment procedure is necessary in order to make use of the full resolution of the detector. This was also attempted in [43] but only with limited success. In this respect it has to be regarded that one detector plane "SI04X" was damaged during installation

and only 50% of its sensor returned signals. As can be seen in fig. 5.26, the resolution of e.g. "SI05X" strongly depends on the kinematics of the track, and thus on whether "SI04X" contributes to the track.

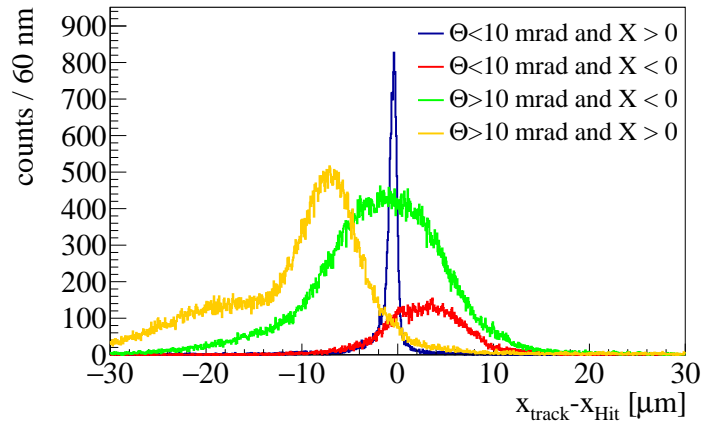


Figure 5.26 Residuum of SI05X for different track criteria prior to the final alignment procedure. In case the track crosses the detector at $X < 0$ the SI04X detector contributes to the tracking while for $X > 0$ this detector is broken. In case the broken region is hit, there are two different cases how SI05X behaves wrongly in case of small angles (blue) it contributes dominantly and the residual is very small while at larger angles the contribution of other detectors adds an offset to the residual (yellow). This issue is cured by aligning the silicon detectors with SI04X deactivated.

This issue has been studied and a solution is found by first performing an alignment using all silicon planes except "SI04X" and then aligning that plane in an additional iteration. An exemplary trend of the detector position for the two planes "SI01U" and "SI01V" can be seen in fig. 5.27 for three weeks of data taking. It turns out that the alignment has jumps at the transition from one period to another what indicates issues in the degrees of freedom used in the initial alignment procedure.

It is seen that the global alignment of the spectrometer still is not optimal [102]. Especially the GEM detectors which have a significant influence on the track reconstruction have problems with the alignment. This is shown exemplary for GM01X where a significant trend of the detector residual as a function of the measurement point can be observed. According to [102] also the dead-zones of these detectors are not correctly placed.

5.6 Reconstruction

The data of the full year 2012 are reconstructed and analyzed. For photon energies above 76 GeV the analysis is performed, applying the same procedure as in 2009. Only the Z-position of the vertex is modified to the new value of 2012. The extracted number of events is 183674 and thus approximately a factor three larger than in 2009. For photon

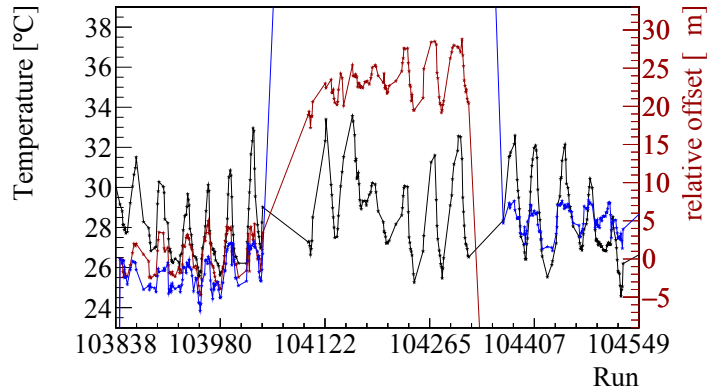


Figure 5.27 The measured temperature in the COMPASS hall as a function of the run number shown in black. Superimposed in red the relative movement of "SI01U" (red) and "SI01V" (blue). It can be seen that the position follows the day-night fluctuations of the temperature while at the edge between two periods the position jumps by an arbitrary number.

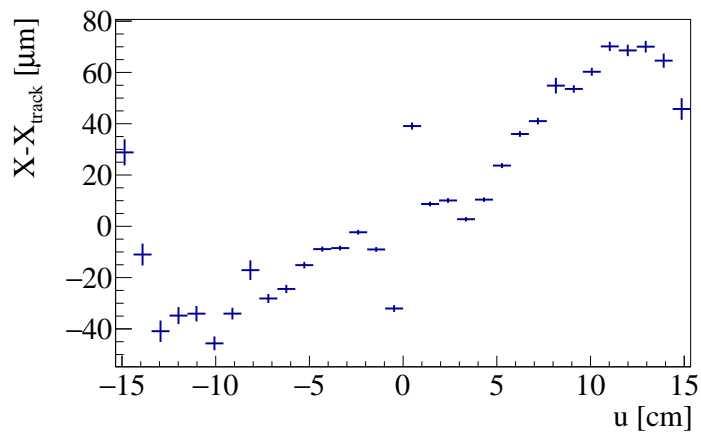


Figure 5.28 Residual of GM01X as a function of the measurement point in the direction of measurement u . A linear slope in this quantity indicates alignment problems.

energies between 30 and 76 GeV the number of events is 236233 and thus similar to the number in the other range, c.f. fig. 5.29. For the periods with muon data a similar number of events can be extracted. Table 5.2 gives an overview over all periods and the number of extracted events.

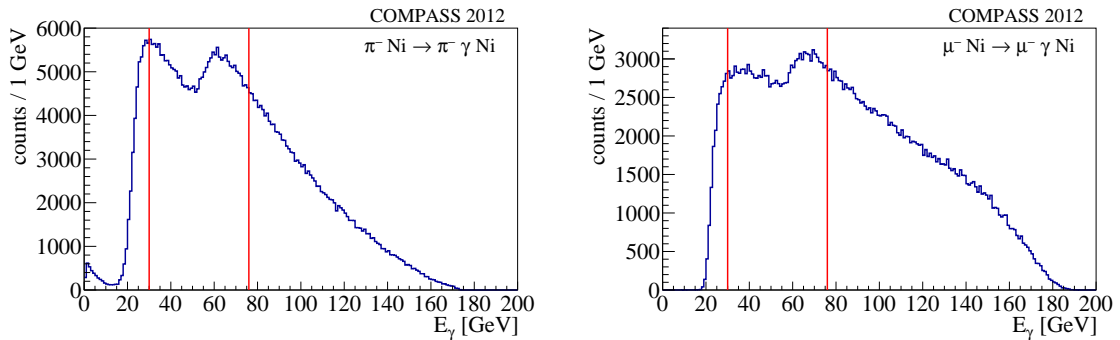


Figure 5.29 Distribution of photon energies measured in 2012 applying the same cuts as for the 2009 data. The dip in the distribution stems from the two different triggers, where the trigger with a lower threshold is scaled by a factor of two. The vertical lines indicate the range which may be used for analysis and for which the number of events is extracted. The left panel shows pion data and the right panel muon data.

For the data with photon energies above 76 GeV it is studied how stable the kinematic distributions are as a function of time. This is done by overlaying the histograms for the different measurement periods. In case of the invariant mass of the $\pi\gamma$ -system, fig. 5.30, the different periods look very similar. Especially at masses above $0.5 \text{ GeV}/c^2$ the structure of the $\rho(770)$ has the same strength and thus the miss-identification probability of π^0 s does not fluctuate.

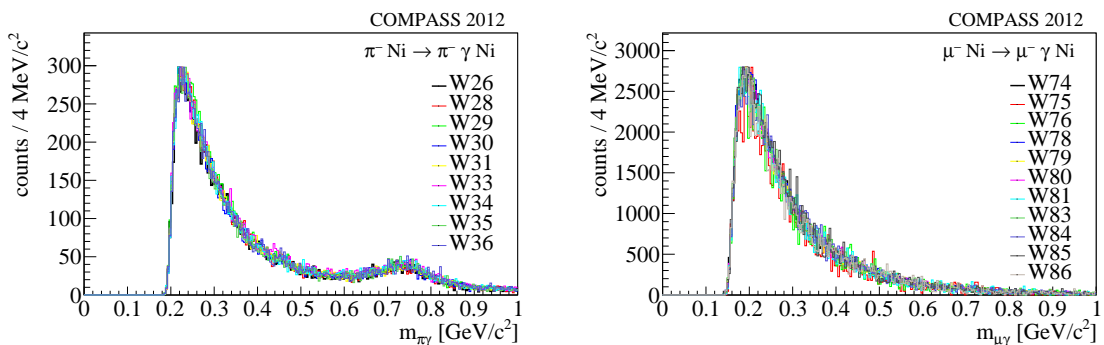


Figure 5.30 Invariant mass distribution of the $\pi\gamma$ -system measured in 2012 for $x_\gamma > 0.4$. The different measurement periods are indicated by colors. All histograms are normalized to the maximum. The left panel shows pion data and the right panel muon data.

The same holds true for the four-momentum transfer Q^2 fig. 5.31. Only the first period seems to be slightly off but this it also has the smallest number of events and thus it might be a statistical effect.

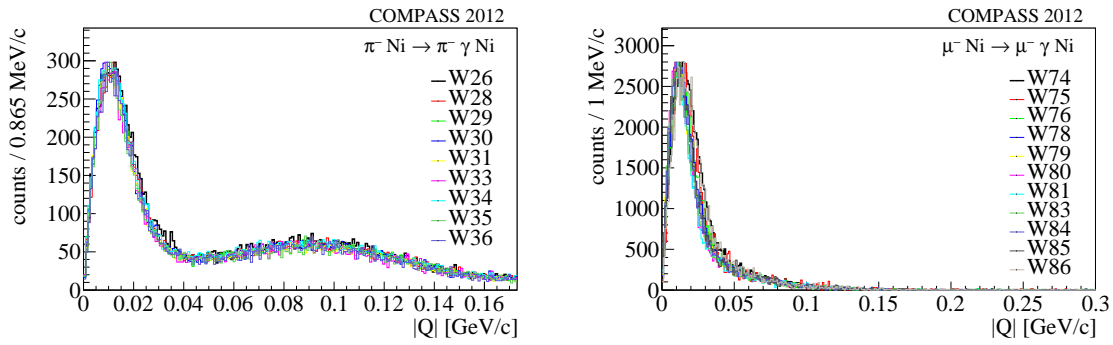


Figure 5.31 Four-momentum transfer distribution measured in 2012 for $x_\gamma > 0.4$. The different measurement periods are indicated by colors. All histograms are normalized to the maximum. The left panel shows pion data and the right panel muon data.

In case of the transverse momentum, the first three weeks have a peak-like structure at small values, fig. 5.32. Comparing this to the discussion of the 2009 data, fig. 4.9, the peak is significantly smaller. This can be explained because in 2012 the electron converter is installed during the full time of data taking. The reduction of events in this peak after the third period is not absolutely clarified, the most probable explanation is the installation of the multiplicity counter fig. 3.17. The additional amount of material between the target and the spectrometer leads to a decrease in the reconstruction efficiency of electrons which are not removed by the electron converter and have a huge cross-section.

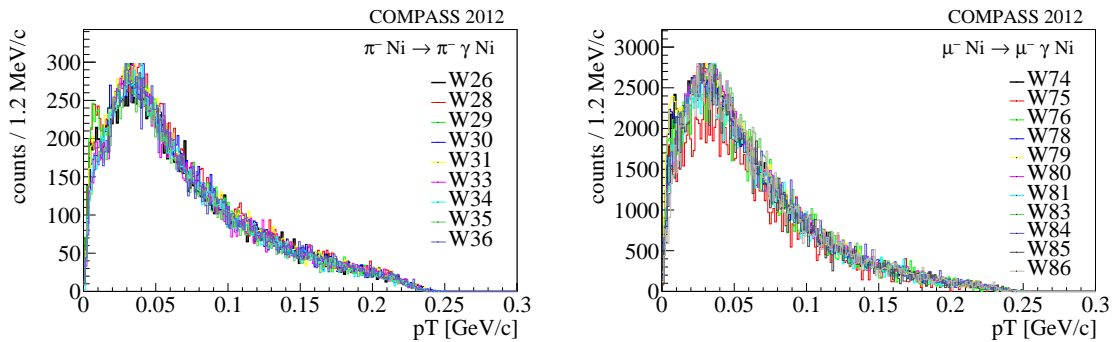


Figure 5.32 Transverse momentum distribution measured in 2012 for $x_\gamma > 0.4$. The different measurement periods are indicated by colors. All histograms are normalized to the maximum. The left panel shows pion data and the right panel muon data.

The relevant kinematic plot, displaying the consistency of the reaction with the process $\pi^- \text{Ni} \rightarrow \text{Ni} \pi^- \gamma$ the energy balance between initial and final-state can be analyzed, c.f. fig. 5.33. Looking at this on a week-by-week basis each distribution has a slightly different central value while the width stays approximately constant. This can be explained by the LED calibration that takes not into account fluctuations on the percent level for the central cells section 5.4.2. This is not a problem for this analysis because this quantity is only checked if it lies inside a rather broad cut range of 15 GeV. In all further calculation

the energy of the photon is derived from the kinematics of the pion.

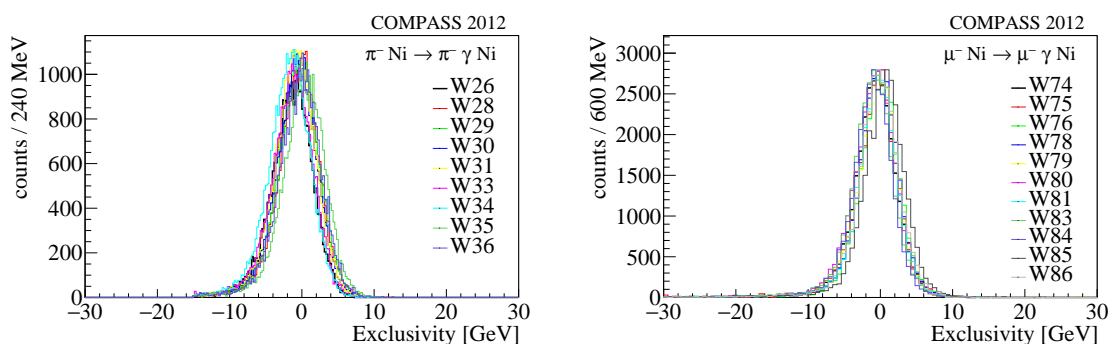


Figure 5.33 Transverse momentum distribution measured in 2012 for $x_\gamma > 0.4$. The different measurement periods are indicated by colors. All histograms are normalized to the maximum. The left panel shows pion data and the right panel muon data.

5.7 Simulation

For this analysis the decision was made to go over from the COMGENAT simulation framework used before to the newly developed TGEANT [103, 104] framework, which is based on GEANT4 [105] and thus written in C++. This has the advantage of a more modern implementation allowing e.g. a better implementation of detector geometries. Further it is possible to implement additional features like a detailed beam-simulation. In this case the interaction is simulated such that the vertex is created at a random Z-position selected uniformly over the length of the two target segments weighted by the squared charge of the nucleus.

In order to prepare the simulation for this analysis several elements of the spectrometer were newly implemented. These are the nickel target, the silicon vertex detector, the multiplicity counter and the sandwich veto detector. All other detectors were already available in the framework.

In addition, an interface to the event generator section 4.4.2 was implemented which allows to provide events inside the framework as soon as the vertex is generated starting from an already simulated beam, interacting with the target.

5.7.1 Verification of the simulation

The new simulation framework has certain improvements and in general is ment to have a better description of the data. This can be checked using the data with muon beam. In case the data are perfectly described by the simulation all distributions should match and the plot of the ratio between data and simulation is a horizontal line as a function of x_γ .

Table 5.2 Number of reconstructed events in the different periods for the two regions of x_γ . The left column shows $\pi\gamma$ events and the right column $\mu\gamma$ events. From the ratio it can be seen that the scaling factor for the lower energetic trigger was changed between W28 and W29. This was also done for the last three periods with muon beam.

| $\pi^- \text{Ni} \rightarrow \text{Ni} \pi^- \gamma$ | | | | $\mu^- \text{Ni} \rightarrow \text{Ni} \mu^- \gamma$ | | | |
|--|-------------------|------------------|-------|--|-------------------|------------------|-------|
| Period | $x_\gamma > 0.16$ | $x_\gamma > 0.4$ | ratio | Period | $x_\gamma > 0.16$ | $x_\gamma > 0.4$ | ratio |
| | | | | W74 | 49439 | 25774 | 0.52 |
| W26 | 45800 | 16655 | 0.36 | W75 | 7551 | 3952 | 0.52 |
| | | | | W76 | 12516 | 6429 | 0.51 |
| | | | | W78 | 61070 | 31342 | 0.51 |
| W28 | 57630 | 21384 | 0.37 | | | | |
| W29 | 70652 | 31838 | 0.45 | W79 | 48284 | 29728 | 0.62 |
| | | | | W80 | 43564 | 27863 | 0.64 |
| W30 | 48325 | 22226 | 0.46 | | | | |
| W31 | 51183 | 23524 | 0.46 | W81 | 14331 | 9020 | 0.63 |
| | | | | W83 | 22737 | 14736 | 0.65 |
| W33 | 38125 | 17659 | 0.46 | | | | |
| W34 | 46270 | 21648 | 0.47 | W84 | 19722 | 11484 | 0.58 |
| | | | | W85 | 12371 | 6662 | 0.54 |
| W35 | 33147 | 15295 | 0.46 | | | | |
| W36 | 28775 | 13445 | 0.47 | W86 | 14070 | 7552 | 0.54 |
| Total π | 419907 | 183674 | 0.44 | Total μ | 305655 | 174542 | 0.57 |

As a first finding in this study it turned out that the implementation of the shower simulation in the electromagnetic calorimeters using a parametrization given in [106] is not calibrated well and the resulting exclusivity spectrum does not match the data, fig. 5.34. A solution to this problem is to perform a full simulation of the showers, tracking all shower particles through the calorimeter cells. This leads to an increased processing time of around 30 s per event. As a consequence of this finding the parametrization has been recalibrated [107] but this currently has not been used for this analysis due to time constraints.

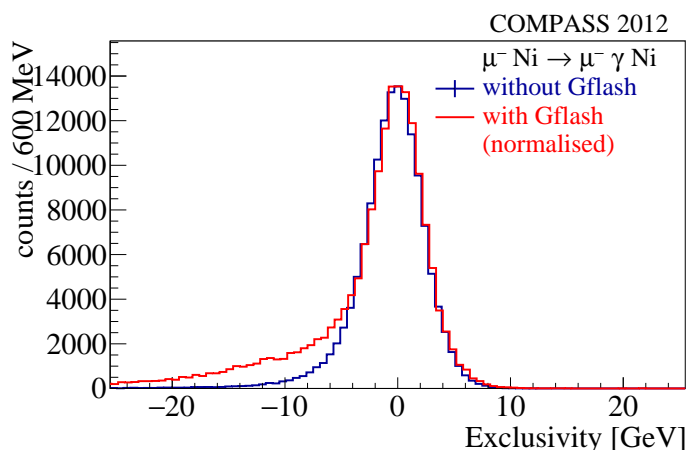


Figure 5.34 Exclusivity distribution obtained from the 2012 data compared with the TGEANT simulation. In case the "Gflash" parametrization is used (a) the simulated width is too high. In case the full shower simulation is applied (b) the spectra match nicely.

Having a reasonable simulation of the electromagnetic calorimeter the extracted physics can be studied in more detail, testing the simulation of the other parts of the spectrometer. It turns out that the ratio between data and simulation is not flat but rather the efficiency to reconstruct events at large values of x_γ is too good in the simulation. This leads to a fake polarizability of $\alpha_\mu^{\text{false}} = 2.5 \times 10^{-4} \text{ fm}^3$, fig. 5.35. It still has to be verified if the effect is stemming from a problem with the reconstruction of the data or a problem with the Monte Carlo simulation. For this two tests were performed.

First the effect of a wrongly aligned spectrometer is checked. This is done by simulating the events using detector positions as extracted from a certain run and reconstructing these events using the detector positions extracted from a different run. Using this approach no significant improvement in the agreement can be found.

Another test is to change the efficiencies assumed for different detectors in simulation. As a first step single detector planes are set to a reduced efficiency of 50 % and the events are reconstructed with different combinations. As a more advanced step efficiencies depending on the position in the detector as described in section 5.7.2 are used. Also these tests turned out to have a too small impact on the result.

Because it is very complex to understand the discrepancy between data and simulation

another approach is to compare the simulation with TGEANT with a similar simulation with COMGEANT. For this a spectrometer setup is chosen in which the description of all elements is available in both frameworks. In this comparison it is found that for a realistic description and reconstruction of the vertex distribution in Z -direction an advanced version of the simulation of the response of the silicon detectors, taking into account the energy loss in the detector, is necessary. The version developed in [83] turns out to be non-operational in the TGEANT case and a previous version is used. Further the cut-off parameter up to which length secondary electron tracks which are produced in the detector are simulated has to be tuned in TGEANT. In the original configuration only secondary tracks were produced in case they have a mean flight path in the detector of more than 100 mm which leads to an energy-loss distribution extending to too high values above 1 MeV. This is fixed by reducing this length to 1 μm while the peak position still is different.

Analyzing the data again, after applying all these modifications still shows problems related to the vertex reconstruction. In case the $\sqrt{Q^2}$ -spectrum of TGEANT is compared with the one reconstructed from COMGEANT-data the width is much smaller, fig. 5.36 (a). In this case only the information from tracking is used for generating the kinematics while the photon kinematics are taken from the true Lorentz vectors. A study cutting on the vertex resolution $[(X - X_{\text{true}})^2 + (Y - Y_{\text{true}})^2 + (Z - Z_{\text{true}})^2] < 1 \text{ cm}^2$ [108] shows that the discrepancy in $\sqrt{Q^2}$ gets reduced fig. 5.36 (b) and thus the problem seems to be related to the simulation of the vertex. This may either be produced by a wrongly applied simulation of the silicon detectors or an underestimated effect from multiple scattering. These influences are currently under investigation.

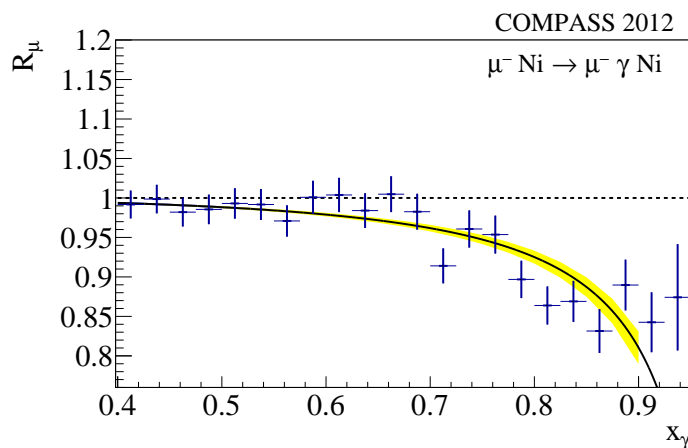


Figure 5.35 x_γ ratio for part of the muon data taken in 2012 with the current TGEANT simulation. A false polarizability of $a_\mu^{\text{false}} = 2.5 \times 10^{-4} \text{ fm}^3$ is extracted.

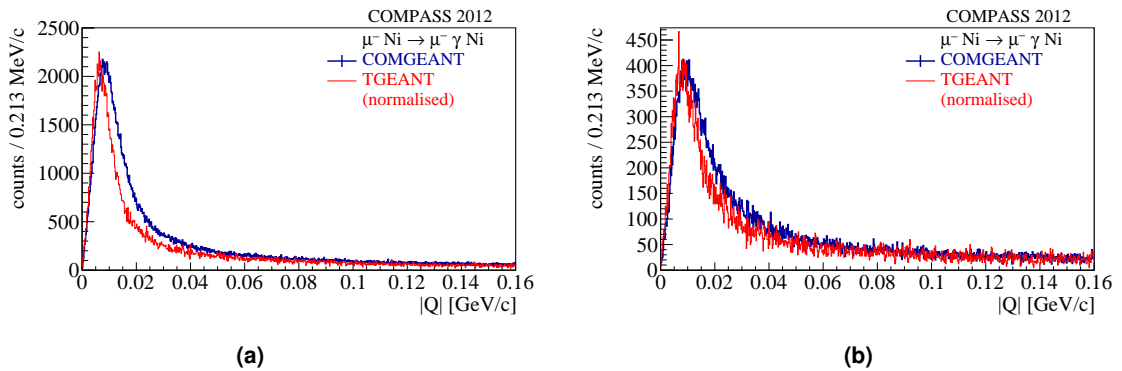


Figure 5.36 Difference between the reconstructed four-momentum transfer distribution for events generated by COMGEANT (blue) and TGEANT (red). The spectra in (a) agree less than in (b) where a cut on the residual of the primary vertex is performed.

5.7.2 Detector efficiencies

For the analysis of the data from 2009 the efficiency of each detector is assumed to be the average in the desired kinematic region. The change of the polarizability value for pions using this method was $\Delta\alpha_\pi = -1.4 \times 10^{-4} \text{ fm}^3$ [29] compared to a reconstruction where the efficiencies are determined globally. As a more precise step a determination of the detector efficiencies as a function of the position where the track crosses a detector can be applied. For this the TGEANT framework provides tools which allow processing of efficiency maps from each detector into a format which can be used in the reconstruction. An exemplary efficiency distribution for GM05Y can be found in fig. 5.37. It is possible to interpolate regions in the detector where no tracks are found as well as to manipulate the maps using image processing tools in order to impose prior knowledge. The efficiency maps can be extracted from the already reconstructed events where a huge amount of data is available. The drawback is that these pseudo-efficiencies are slightly biased and e.g. effects of miss-alignment have an impact. In case real efficiencies from specially reconstructed data are used one is limited by statistics and the geometric resolution is not very precise.

As a first test, efficiency maps for all GEM and all MWPC detectors are extracted using pseudo-efficiencies and applied to the simulation. The impact of this correction is rather small with an effect of $\Delta\alpha_\pi = -0.1 \times 10^{-4} \text{ fm}^3$ still it may change in case more detectors are considered.

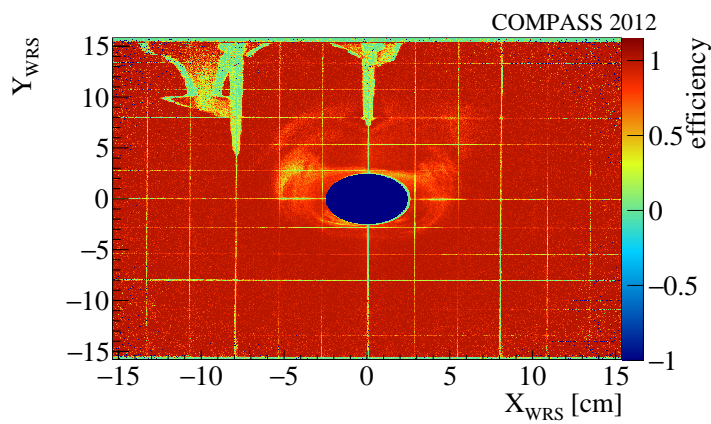


Figure 5.37 Efficiency of the GEM detector GM05Y as a function of the position of the track in the wire reference-system (WRS). Negative values indicate points where no track was found or where the detector has its dead-zone. The grid structure is produced by the support elements of the detector while the broad patterns on top are produced by too much glue applied in these regions.

Chapter 6

Conclusion and Outlook

For the data taken in 2009 and 2012 a trigger system has been developed. It is implemented fully in the digital readout of the electromagnetic calorimeter ECAL2. The system allows to trigger Primakoff-Compton events down to an energy threshold of 30 GeV. It was shown, that the trigger operated with a good efficiency over the full energy range. Operating at a higher threshold above about 60 GeV, it is possible to investigate final-states with more than one photon.

The data which were taken in 2009 are fully analyzed for the Primakoff Compton channel. In total about 63000 events could be extracted. From these data the worlds most precise value for the polarizability of the charged pion of $\alpha_\pi = (2.0 \pm 0.6_{\text{stat.}} \pm 0.7_{\text{syst.}}) \times 10^{-4} \text{ fm}^3$ is extracted assuming $\alpha_\pi = -\beta_\pi$, and published in [1]. The published value is the only measurement considered by the particle data group for this quantity[4].

The analysis of the data taken in 2012 has been started, where with more events and a broader kinematic range the precision from the 2009 data can be improved. Further an independent measurement of α_π and β_π is in reach. The full statistics of the data taken in 2012 has been analyzed and first conclusions can be drawn. The amount of measured $\pi^- \text{Ni} \rightarrow \text{Ni} \pi^- \gamma$ events with values of $x_\gamma > 0.4$ is with slightly above 180×10^3 about a factor of three larger than the number of events collected in 2009. The amount of $\mu^- \text{Ni} \rightarrow \text{Ni} \mu^- \gamma$ is with events with values of $x_\gamma > 0.4$ is more than 170×10^3 . The quality of the data looks promising and seems to be similar to 2009 where around 60×10^3 events have been extracted.

In case of a reproduction of the data several aspects have to be considered. The reconstruction of the data has shown that the alignment of the spectrometer is not perfect and has to be refined. Further the reconstruction of the beam momentum has to be enabled in the reconstruction. Another possible improvement which may be anticipated comes from the refined analysis of the CEDARS [95] a time-dependent calibration would improve the efficiency of the particle identification and a more general reconstruction approach would allow identifying protons under certain kinematics. The cluster position dependence on the position within a cell of ECAL2 should be extracted and applied on the reconstruction level.

6 CONCLUSION AND OUTLOOK

In terms of the simulation, more efforts are necessary in order to extract a physics result. Obviously the problem with the biggest impact is the understanding of the discrepancy observed to the COMGEANT simulation as well as to the data. This problem is currently worked on [108]. Further the impact of the position dependent corrections have to be studied on a more precise level and implemented for all relevant detectors. In case of the calorimeter reconstruction the implementation of the parametrized "Gflash"-shower simulation should be studied in order to decrease the simulation time.

Own contributions

I started this thesis by simulating the trigger logic and implementing it into FPGA code on a newly developed back-plane module. Together with Igor Konorov I debugged the logic and prepared it to be fully commissioned during the 2012 data taking. I was responsible for the operation of the system as well as for the readout of the whole electromagnetic calorimeter. I further tested the readout to be operational for the newly developed ECAL0 detector.

Later on I took over the analysis performed by Thiemo Nagel in his PhD thesis and improved it till the data was ready for release. Together with Alexey Guskov and the support of Jan Friedrich I performed the cross-check of the analysis and tested the methods for subtracting the background contributions. After the data have been released, I was part of the drafting committee for the published paper [1] and took part in the refereeing process.

For the preparation of the analysis of the 2012 data I implemented several improvements to the reconstruction code and prepared calibrations. Further I supervised the production process. I implemented several geometries into the TGEANT framework and prepared the simulation for analysis. I started comparing the new simulation framework to the old simulation and to the reconstructed data.

As a not primary focus of the thesis I also studied the reaction $\pi^- \text{Ni} \rightarrow \pi^- \eta \text{Ni}$ and provided several insights how this channel can be further analyzed. I helped several people to get familiar with the COMPASS software and to use it for their analyzes I also took responsibility in the support of several other experiments in questions about electronics. And thus supported the development of the electronics for the BOB experiment, the PENeLOPE experiment and developed a standalone Ethernet based readout for test measurements used by the AFIS experiment.

Acknowledgments

First of all I would like to thank Prof. Stephan Paul for the opportunity to work on this thesis. From the start with my Diploma thesis I was able to get insight into several topics in physics as well as in terms of more technology related topics. He also gave me the freedom to participate, despite in my main subject, in several other interesting projects. Further I greatly appreciate the possibility to represent my work in many conferences and in many countries.

Next I want to thank the people involved in the electronics development. I was introduced to this topic by Igor Konorov and Alexander Mann. I could gather a lot of knowledge and the passion in development of cutting edge. I also appreciated the discussions about the developments with Dmytro Levit, Dominic Gaisbauer, Dominik Steffen and Yunpeng Bai.

During the analysis I received great support by Jan Friedrich from whom I received a lot of support due to his great experience in data analysis. Further I had a very good cooperation with my cross-check partner Alexey Guskov and thank Thiemo Nagel for the initial work done in this topic. I received a lot of support in discussion technical details of the analysis with my colleagues Boris Grube, Sebastian Uhl, Markus Krämer, Alex Austregesilo,, Sverre Dørheim, Karl Bicker, Christian Dreisbach and Steffan Wallner.

I'd like to thank my long-term office partners Alexander Mann, Karl Bicker, Alex Austragesilo and Dmytro Levit for having a productive and fun time. Here I also want to thank the PENELOPE and AFIS groups and especially Dominic Gaisbauer, Wolfgang Schreyer, Lea Prüfer and Michael Milde for exciting card games during the coffee breaks.

A great thank goes to Florian Haas, Alex Austragesilo, Prof. Stephan Paul and Sverre Dørheim and Jan Friedrich for supporting my during a complicated time I had in the middle of my thesis. It was really great to have this kind of support from people I work with.

Finally, I want to thank my parents Waltraud and Klaus Huber for the constant support during my life my studies and this thesis. Na koniec chciałbym podziękować Joanna Kontny. Bez twojej cierpliwości i wsparcia nie osiągnąłbym celu. Jesteś moim więcej.

Appendix A

Calibration files for 2012

A.1 CEDAR 1 calibration file

```
#T0 calibration for 8@PMTs
timeT0 -1446 -1445 -1445 -1445 -1445 -1445 -1446 -1446
#T0 RMS calibration for 8 PMTs
timeRMS 1 1 1 1 1 1 1 1
#angular offset in x direction (urad)
xCent -3.595e-5
#angular offset in y direction (urad)
yCent -4.782e-6
#change mapping of the individual PMs
remap 0 2 3 4 1 5 6 7

#Transport Matrix provided by Lau Gatignon for the beam optics
transp 3000.0 1.000 30.000 0.000 1.000 1.000 30.000
transp 0.0 1.000 0.000 0.000 0.000 0.000
transp -6939.6 0.670 47.160 -0.021 0.000 0.924 73.374
transp -0.014 0.000 0.000 0.000 0.772 0.022
transp -7571.3 0.536 47.160 -0.021 0.000 0.838 73.374
transp -0.014 0.000 0.000 0.000 0.908 0.022
transp -7591.3 0.531 47.160 -0.021 0.000 0.835 73.374
transp -0.014 0.000 0.000 0.000 0.912 0.022
transp -8223.0 0.398 47.160 -0.021 0.000 0.749 73.374
transp -0.014 0.000 0.000 0.000 1.048 0.022
```

A CALIBRATION FILES FOR 2012

```
#Parametrization of the probability functions for pions
#the naming is in the format C<cedarNumber>G<groupNumber>P<hits>
#the next value represents the number of parameters used. The formula is:
#P0 + P1 * atan[ (CEDr - P2) / P3 ] + P4 * atan[ (CEDr - P5) / P6 ] + ...
C1G0P0 13 8.903484976345e-01
-3.556547299835e-01 6.868818780741e-05 3.029130725338e-05
3.815039443881e-01 2.076552251572e-04 3.292524695022e-05
-1.444810395700e-01 2.933010219413e-04 5.489377668317e-05
0.000000000000e+00 0.000000000000e+00 1.000000000000e-04
C1G0P1 13 1.851213370559e-01
5.000000000000e-01 6.795437858132e-05 3.625380393100e-05
-3.360961838307e-01 2.077305533204e-04 2.936586291333e-05
1.529428970561e-01 2.986817764533e-04 6.298865367955e-05
-2.628094356545e-01 5.834361105273e-05 1.067802749781e-04
C1G1P0 13 7.889364230783e-01
-3.741778453307e-01 6.482799209054e-05 2.846455569039e-05
3.588143654015e-01 2.442583464408e-04 5.192838236431e-05
-1.481778535037e-01 3.999999999633e-04 9.350092486198e-05
0.000000000000e+00 0.000000000000e+00 1.000000000000e-04
C1G1P1 13 9.951737095174e-02
4.262975325344e-01 5.910210401272e-05 3.817031296899e-05
-5.000000000000e-01 9.020262460420e-05 5.626312155640e-05
4.933385085879e-01 2.169013197140e-04 5.805642533097e-05
-3.603494975544e-01 2.581866362981e-04 4.030607122716e-05
C1G1P2 13 3.958325355050e-02
2.887803213251e-01 8.262553611648e-05 2.980901900477e-05
-5.000000000000e-01 2.114092621329e-04 4.045934120616e-05
3.262549434025e-01 2.190881569646e-04 9.730935205611e-05
0.000000000000e+00 0.000000000000e+00 1.000000000000e-04
C1G2P0 13 6.844351249022e-01
-5.000000000000e-01 7.345064861747e-05 3.958465167073e-05
1.390530023510e-01 2.835631039513e-04 3.706063382586e-05
3.858321366821e-01 5.301914214858e-05 1.968657226171e-04
0.000000000000e+00 0.000000000000e+00 1.000000000000e-04
C1G2P1 13 1.357097280886e-01
2.838464992641e-01 6.551320302296e-05 3.255420851274e-05
-2.360796434921e-01 1.271721620127e-04 4.577680419763e-05
1.498575355827e-01 2.422095102963e-04 4.646508783225e-05
-1.122295140868e-01 3.210230254008e-04 7.737499420816e-05
C1G2P2 13 3.436957778610e-02
9.722728557542e-02 9.084858005099e-05 2.222375351244e-05
-2.344706378825e-01 2.568263993693e-04 4.148835095590e-05
1.717538298305e-01 1.264374784714e-04 3.430136838411e-05
0.000000000000e+00 0.000000000000e+00 1.000000000000e-04
```

C1G3P0 13 8.369505819095e-01
 -3.532520287243e-01 1.040030018383e-04 4.913708665900e-05
 5.000000000000e-01 3.201643850701e-04 3.065680308932e-05
 -2.919055529437e-01 3.246731677013e-04 1.900000277704e-05
 0.000000000000e+00 0.000000000000e+00 1.000000000000e-04
 C1G3P1 13 1.347579184368e-01
 4.997487749337e-01 8.599509260346e-05 5.892814160904e-05
 -5.170249011130e-02 1.560909048759e-04 2.431758818233e-05
 -1.482866429979e-01 4.902232505357e-05 5.397096446192e-05
 -1.794240243279e-01 2.153795657392e-04 8.042031259651e-05
 C1G3P2 13 5.796777461240e-02
 4.787675164726e-01 1.487721995825e-04 7.288087234810e-05
 -2.902160714662e-01 1.145406732298e-04 8.875865339054e-05
 -1.651262850296e-01 3.064690194389e-04 4.132364741313e-05
 0.000000000000e+00 0.000000000000e+00 1.000000000000e-04
 C1G4P0 13 7.613039716915e-01
 4.122389230164e-01 1.975833515994e-04 1.567325410454e-04
 -5.000000000000e-01 1.765371491653e-04 8.779079417194e-05
 1.519423202253e-02 1.541552928053e-04 1.900000006143e-05
 0.000000000000e+00 0.000000000000e+00 1.000000000000e-04
 C1G4P1 13 1.922040623967e-01
 4.079559129105e-01 9.706501711375e-05 3.480626185484e-05
 -3.231339507325e-01 9.582945803475e-05 3.097007524542e-05
 4.166609158263e-01 1.914459421882e-04 6.717112545762e-05
 -4.550468761617e-01 1.957533648951e-04 1.159787939079e-04
 C1G4P2 13 4.366867483199e-02
 4.763758608913e-01 4.900014074534e-05 6.931221527838e-05
 -4.707435505169e-01 5.037862600678e-05 6.804901836043e-05
 2.040641193870e-02 2.725636209991e-04 2.388406147733e-05
 0.000000000000e+00 0.000000000000e+00 1.000000000000e-04
 C1G5P0 13 7.708158561045e-01
 -1.938073042978e-01 1.745234068601e-04 8.583394715455e-05
 3.210035604327e-01 1.912067435633e-04 1.068849792990e-04
 -2.064970873721e-01 2.972597817212e-04 6.279018972612e-05
 0.000000000000e+00 0.000000000000e+00 1.000000000000e-04
 C1G5P1 13 1.898227033004e-01
 -2.927692511048e-01 4.943362795622e-05 1.798240761596e-04
 4.548347479617e-01 9.605137022451e-05 1.683442194018e-04
 9.075048469120e-02 3.022517825756e-04 3.677128641526e-05
 -1.877135564208e-01 1.379100906577e-04 1.370503744509e-04

A CALIBRATION FILES FOR 2012

C1G5P2 13 5.788109276625e-02
 3.470483260485e-01 5.299400425817e-05 1.161177951286e-04
 -3.676824058300e-01 5.385273477461e-05 1.166224109746e-04
 3.054748006227e-02 3.211144208506e-04 5.650741091324e-05
 0.000000000000e+00 0.000000000000e+00 1.000000000000e-04
 C1G6P0 13 9.074806091143e-01
 7.630950250362e-03 2.307343366533e-04 2.948229010985e-05
 4.978171739774e-01 3.846411252216e-04 3.344699175457e-04
 -3.565696245801e-01 3.166754061374e-04 9.416372407874e-05
 0.000000000000e+00 0.000000000000e+00 1.000000000000e-04
 C1G6P1 13 9.919000039137e-02
 -2.984254666902e-03 1.036406190335e-04 1.900000257814e-05
 9.636169255171e-02 3.785527293598e-04 1.912726616797e-05
 2.751551670624e-01 3.079286992889e-04 5.352915019849e-05
 -3.498481350481e-01 3.475794634839e-04 7.898424320209e-05
 C1G6P2 13 -1.839306010485e-02
 4.041554781091e-03 1.296703353988e-04 2.390289220930e-05
 -4.976028905470e-01 3.836025837946e-04 3.762629234940e-04
 3.127102613094e-01 3.327370412688e-04 1.701815295395e-04
 0.000000000000e+00 0.000000000000e+00 1.000000000000e-04
 C1G7P0 13 7.355663107952e-01
 -1.097348550611e-02 1.210389217782e-04 3.359880923805e-05
 4.853341880400e-01 1.509986413758e-04 6.426766659393e-04
 -2.181455062340e-01 3.192415050173e-04 7.581799285979e-05
 0.000000000000e+00 0.000000000000e+00 1.000000000000e-04
 C1G7P1 13 8.229688219794e-02
 -1.668277568666e-01 7.344816987489e-05 2.333026267757e-04
 -4.054088983805e-02 3.316061692275e-04 9.092613564030e-04
 5.298383079505e-02 3.109828575578e-04 3.919232645919e-05
 4.827656811510e-01 6.094224756814e-05 8.851101063888e-04
 C1G7P2 13 1.151997919221e-01
 2.675782064779e-01 1.131944761764e-04 9.771264418395e-05
 -3.528514006327e-01 1.102439442902e-04 1.222483602091e-04
 8.435314198082e-02 3.037819262894e-04 7.487036861514e-05
 0.000000000000e+00 0.000000000000e+00 1.000000000000e-04
 C1G8P0 13 9.072140812647e-01
 4.988813710197e-01 3.174009466747e-04 3.275633188163e-04
 -1.335641579238e-02 1.253785588400e-04 3.470037230229e-05
 -3.401536890992e-01 3.177029627783e-04 1.207491937708e-04
 0.000000000000e+00 0.000000000000e+00 1.000000000000e-04
 C1G8P1 13 5.268372378278e-02
 2.652818256886e-01 1.271386845079e-04 7.322076361182e-05
 -3.407983228341e-01 1.283777909081e-04 8.894485873852e-05
 4.972678469565e-01 3.304852993866e-04 1.447035841096e-04
 -4.999792920037e-01 3.993078004992e-04 2.344567654007e-04

```

#Parametrization of the probability functions for kaons
#the naming is in the format C<cedarNumber>G<groupNumber>K<hits>
#the next value represents the number of parameters used. The formula is:
#P0 + P1 * atan[ (CEDr - P2) / P3 ] + P4 * atan[ (CEDr - P5) / P6 ] + ...
C1G0K0  13  2.807794666289e-01
          2.098133906983e-01  1.043097516124e-04  2.225629257001e-05
          1.078582635131e-01  7.912494567945e-05  1.900000035463e-05
          -2.075053687629e-01  3.029716599402e-04  4.397100491458e-05
          0.000000000000e+00  0.000000000000e+00  1.000000000000e-04
C1G0K1  13  7.763922457718e-01
          5.000000000000e-01  2.650735950348e-04  1.370906982996e-04
          -3.498037446674e-01  9.373264732553e-05  2.801128551892e-05
          -4.950812362600e-01  1.656617278255e-04  3.089946446161e-05
          3.572527602736e-01  1.647248973107e-04  2.288822849116e-05
C1G1K0  13  1.806615350133e-01
          -1.198239059374e-01  4.900000000125e-05  5.737158683882e-05
          4.791834851476e-01  1.090546211387e-04  3.755747332864e-05
          -2.858932959914e-01  3.101231614619e-04  5.345623984606e-05
          0.000000000000e+00  0.000000000000e+00  1.000000000000e-04
C1G1K1  13  2.903991049061e-01
          5.000000000000e-01  6.300208583617e-05  4.412632627987e-05
          -4.094729674830e-01  4.900001119171e-05  5.514184887797e-05
          1.186638070610e-01  3.137814812758e-04  5.398825265323e-05
          -2.016221671699e-01  1.312579632932e-04  2.975547946254e-05
C1G1K2  13  6.007755163223e-01
          -1.637256714395e-01  1.029552422969e-04  1.900000000030e-05
          -1.160660851596e-01  7.523419262685e-05  1.900000000101e-05
          1.686042514351e-01  3.158221920576e-04  6.078518519193e-05
          0.000000000000e+00  0.000000000000e+00  1.000000000000e-04
C1G2K0  13  6.694767344204e-02
          1.260961739334e-01  1.212925539526e-04  2.400223368837e-05
          3.226629827480e-01  1.922538262809e-04  4.387196283490e-05
          -5.000000000000e-01  2.990888202779e-04  1.116927142456e-04
          0.000000000000e+00  0.000000000000e+00  1.000000000000e-04
C1G2K1  13  4.122557211049e-01
          4.938662221794e-01  1.023327399187e-04  4.392106587464e-05
          -4.948810715083e-01  2.102959808279e-04  9.713182533397e-05
          4.560947521945e-01  3.162163283674e-04  9.423979659649e-05
          -3.945899988154e-01  1.229625784496e-04  7.900767001289e-05
C1G2K2  13  5.365050187978e-01
          -1.400550604612e-01  9.801142399847e-05  1.917916552716e-05
          -1.266836990425e-01  1.265049848867e-04  2.591925506952e-05
          1.111540745402e-01  2.842313178977e-04  2.618133754154e-05
          0.000000000000e+00  0.000000000000e+00  1.000000000000e-04

```

A CALIBRATION FILES FOR 2012

C1G3K0 13 2.230045556734e-01
 -6.790799258795e-03 4.900000000241e-05 1.900000000716e-05
 5.000000000000e-01 3.289722675574e-04 1.166049241477e-04
 -3.239946102025e-01 3.498965172481e-04 6.710391686501e-05
 0.000000000000e+00 0.000000000000e+00 1.000000000000e-04
 C1G3K1 13 2.637577081776e-01
 3.014179588213e-02 1.694266896708e-04 1.994303238124e-05
 -3.779857016934e-01 8.120140540736e-05 5.073200744840e-05
 4.706639145824e-01 9.388909758544e-05 5.167926681040e-05
 -7.463677156145e-02 3.379512112522e-04 1.900594984473e-05
 C1G3K2 13 6.364245726846e-01
 1.408244352287e-01 4.90000000020e-05 3.920974490883e-05
 -5.000000000000e-01 1.087668632092e-04 1.183081705052e-04
 1.011548390619e-01 3.449920444969e-04 2.071126440596e-05
 0.000000000000e+00 0.000000000000e+00 1.000000000000e-04
 C1G4K0 13 1.836542669362e-01
 2.875956887818e-01 1.155560190871e-04 1.988301690370e-05
 7.710181998710e-02 2.784801421609e-04 5.678102517224e-05
 -2.808318678361e-01 1.171450649738e-04 1.950077266938e-05
 0.000000000000e+00 0.000000000000e+00 1.000000000000e-04
 C1G4K1 13 2.716639643906e-01
 4.504752634881e-01 5.730240300127e-05 7.820972501853e-05
 -4.255969337021e-01 5.151401736112e-05 7.509574327032e-05
 1.924086336816e-02 1.321677235117e-04 1.900000087194e-05
 -1.392918321252e-02 3.999970596909e-04 1.900081936126e-05
 C1G4K2 13 5.020912341243e-01
 -1.466949822045e-01 1.038068737287e-04 6.418149409354e-05
 -5.815726766908e-02 2.607590276985e-04 1.900000094999e-05
 1.481589628421e-01 4.900004664409e-05 1.384950658535e-04
 0.000000000000e+00 0.000000000000e+00 1.000000000000e-04
 C1G5K0 13 1.415896649864e-01
 -5.795191661471e-02 3.492676154227e-04 1.900000000462e-05
 5.000000000000e-01 8.278371325829e-05 1.013865720989e-04
 -2.984383388903e-01 5.345656916484e-05 7.495255033214e-05
 0.000000000000e+00 0.000000000000e+00 1.000000000000e-04
 C1G5K1 13 2.381615694689e-01
 2.016712867946e-01 7.288927764141e-05 7.061106322185e-05
 -4.958307931639e-01 1.290729732040e-04 1.998335145070e-05
 4.899763557887e-01 1.275314203376e-04 1.938353540059e-05
 -1.134642204788e-01 2.843511370485e-04 7.813657747555e-05

C1G5K2 13 5.712758183258e-01
 9.369291180300e-02 3.265728666351e-04 2.138527979009e-05
 -4.678821912153e-02 1.110077203477e-04 1.900000004300e-05
 -2.378775925730e-01 8.173753739516e-05 7.210273116487e-05
 0.000000000000e+00 0.000000000000e+00 1.000000000000e-04
 C1G6K0 13 1.553844764063e-01
 -1.134252373386e-01 4.900000000520e-05 6.605611040732e-05
 5.000000000000e-01 1.031249368283e-04 5.547463797412e-05
 -2.628215342010e-01 3.002553092097e-04 3.975617756480e-05
 0.000000000000e+00 0.000000000000e+00 1.000000000000e-04
 C1G6K1 13 2.136462491842e-01
 4.238949455915e-01 5.807002604145e-05 5.791640272073e-05
 -3.706854532872e-01 1.324670985524e-04 5.734245907463e-05
 1.439596372679e-01 3.039779952137e-04 4.658198708240e-05
 -8.250222010722e-02 9.870567384723e-05 1.900000000004e-05
 C1G6K2 13 5.736962362349e-01
 2.250006003605e-01 8.283970802208e-05 9.978522514757e-05
 1.200832515555e-01 2.950034555889e-04 4.585939103974e-05
 -5.000000000000e-01 6.101478891096e-05 4.845691308541e-05
 0.000000000000e+00 0.000000000000e+00 1.000000000000e-04
 C1G7K0 13 1.455164670174e-01
 -1.617019746938e-01 1.265375459661e-04 1.270246537815e-04
 5.000000000000e-01 7.504370749089e-05 4.267991861609e-05
 -2.174200042650e-01 3.134706400279e-04 3.612367073673e-05
 0.000000000000e+00 0.000000000000e+00 1.000000000000e-04
 C1G7K1 13 2.166744178526e-01
 4.094325711767e-01 4.900871119221e-05 5.057914435250e-05
 -4.992553339579e-01 8.633914852258e-05 4.481761946463e-05
 3.262563741187e-01 2.585616187004e-04 1.160084313189e-04
 -9.329210029969e-02 2.274830224683e-04 4.193086443019e-05
 C1G7K2 13 6.248592259535e-01
 7.194451075365e-02 1.151226537641e-04 4.449715150090e-05
 -3.935264360187e-01 5.103283927769e-05 3.663088700230e-05
 1.324420148643e-01 3.038446714641e-04 3.538960763296e-05
 0.000000000000e+00 0.000000000000e+00 1.000000000000e-04
 C1G8K0 13 2.204140647548e-01
 -5.000000000000e-01 2.682356416734e-04 8.668385494530e-05
 3.912300715831e-01 5.625061569332e-05 3.361778468584e-05
 1.970089951221e-01 2.331006386506e-04 5.329157471930e-05
 0.000000000000e+00 0.000000000000e+00 1.000000000000e-04
 C1G8K1 13 6.890922123591e-01
 -5.000000000000e-01 5.569234358717e-05 3.746569839604e-05
 2.344580204461e-01 4.900003257041e-05 1.058757067184e-04
 4.997878985488e-01 3.174166701601e-04 2.640440553142e-05
 -3.181641356513e-01 3.188306118661e-04 1.900000267944e-05

```
#Parametrization for the likelihood limits.
#In order to make it flexible it is given as a TF1 string from ROOT
LIMIT C1G0PKLIM -7.3+1.8*TMath::ATan((x-5e-05)/2.1e-05)
LIMIT C1G0PPLIM -11.4+5.8*TMath::ATan((x+7e-06)/2.0e-05)
LIMIT C1G0KKLIM -5.7+1.8*TMath::ATan((x-3.4e-05)/3.0e-05)
LIMIT C1G0KPLIM -6.8+1.8*TMath::ATan((x-5e-05)/2.6e-05)
LIMIT C1G1PKLIM -7.6+1.8*TMath::ATan((x-5e-05)/3.1e-05)
LIMIT C1G1PPLIM -10.2+5.8*TMath::ATan((x+7e-06)/4.0e-05)
LIMIT C1G1KKLIM -5.4+2.0*TMath::ATan((x-4e-05)/4.0e-05)
LIMIT C1G1KPLIM -6.6+1.8*TMath::ATan((x-5e-05)/3.1e-05)
```

A.2 CEDAR 2 calibration file

```
#T0 calibration for 8 PMTs
timeT0 -1467 -1466 -1467 -1466 -1467 -1467 -1467 -1466
#T0 RMS calibration for 8 PMTs
timeRMS 1 1 1 1 1 1 1 1
#angular offset in x direction
xCent -4.101e-5
#angular offset in y direction
yCent -8.282e-6
#change mapping of the individual PMs
remap 1 0 6 4 2 3 7 5

#Transport Matrix provided by Lau Gagnon for the beam optics
transp 3000.0 1.000 30.000 0.000 1.000 1.000 30.000
transp 0.0 1.000 0.000 0.000 0.000 0.000 0.000
transp -6939.6 0.670 47.160 -0.021 0.000 0.924 73.374
transp -0.014 0.000 0.000 0.000 0.772 0.022
transp -7571.3 0.536 47.160 -0.021 0.000 0.838 73.374
transp -0.014 0.000 0.000 0.000 0.908 0.022
transp -7591.3 0.531 47.160 -0.021 0.000 0.835 73.374
transp -0.014 0.000 0.000 0.000 0.912 0.022
transp -8223.0 0.398 47.160 -0.021 0.000 0.749 73.374
transp -0.014 0.000 0.000 0.000 1.048 0.022
```

```

#Parametrization of the probability functions for pions
#the naming is in the format C<cedarNumber>G<groupNumber>P<hits>
#the next value represents the number of parameters used. The formula is:
#P0 + P1 * atan[ (CEDr - P2) / P3 ] + P4 * atan[ (CEDr - P5) / P6 ] + ...
C2G0P0  13 8.884236176789
        -3.527964167537e-01 5.835024068593e-05 2.803081978637e-05
        3.848692914082e-01 2.055692113394e-04 3.392505799362e-05
        -1.469060670943e-01 2.976654385027e-04 4.558130144044e-05
        0.000000000000e+00 0.000000000000e+00 1.000000000000e-04
C2G0P1  13 9.429146920853e-02
        3.720384226992e-01 5.855174685522e-05 2.919449512380e-05
        -2.008466413557e-01 2.017231910820e-04 2.330845347038e-05
        2.721701699227e-01 2.941302673432e-04 4.469086211366e-05
        -3.640572400995e-01 2.412864952179e-04 7.676021345483e-05
C2G1P0  13 7.867059047106e-01
        -3.684289444622e-01 5.524334460015e-05 2.623790355017e-05
        3.901497276216e-01 2.415841950481e-04 5.273412509988e-05
        -1.672058629206e-01 3.603881826988e-04 7.347511460205e-05
        0.000000000000e+00 0.000000000000e+00 1.000000000000e-04
C2G1P1  13 4.049402911129e-02
        3.535959658290e-01 4.900000015068e-05 4.217834929531e-05
        -2.717945503980e-01 8.807976401729e-05 3.793522396659e-05
        1.550707479642e-01 1.975186898703e-04 3.323178280005e-05
        -1.430364867372e-01 2.653102458784e-04 2.400864626525e-05
C2G1P2  13 7.173400759632e-02
        2.887904965981e-01 7.161193034228e-05 2.751852014517e-05
        -5.000000000000e-01 2.108608264923e-04 4.060567619170e-05
        3.413293550545e-01 2.414384119914e-04 9.753225514505e-05
        0.000000000000e+00 0.000000000000e+00 1.000000000000e-04
C2G2P0  13 7.894450213063e-01
        -3.824593346608e-01 6.317907131072e-05 3.185334857107e-05
        5.000000000000e-01 3.158794669438e-04 9.695633412161e-05
        -2.434907641874e-01 3.686430048639e-04 7.425584938386e-05
        0.000000000000e+00 0.000000000000e+00 1.000000000000e-04
C2G2P1  13 1.425959073188e-01
        4.613996987043e-01 5.865558397958e-05 4.054015481916e-05
        -4.356864875099e-01 1.020670427138e-04 5.272183761994e-05
        4.649267813842e-01 2.420724410130e-04 6.968138069488e-05
        -3.903798077648e-01 2.682119164840e-04 9.150508560768e-05
C2G2P2  13 4.168026405718e-02
        2.982572218826e-01 9.568922661602e-05 3.575485896061e-05
        -2.487825495371e-01 2.550265625080e-04 4.098348997889e-05
        2.075715462467e-02 3.999999998121e-04 3.634839785434e-05
        0.000000000000e+00 0.000000000000e+00 1.000000000000e-04

```

A CALIBRATION FILES FOR 2012

C2G3P0 13 8.286523712952e-01
-3.717353362864e-01 8.814920790488e-05 4.637789033338e-05
3.962657097961e-01 2.915509597138e-04 8.781242291551e-05
-1.659142531894e-01 2.421280586747e-04 9.628243922869e-05
0.000000000000e+00 0.000000000000e+00 1.000000000000e-04
C2G3P1 13 1.985257521854e-01
4.435357203992e-01 7.700212117387e-05 4.871259564577e-05
-3.267557486897e-02 1.536068040470e-04 1.900116150984e-05
4.226483555030e-02 2.982147573176e-04 3.402397910060e-05
-4.360706238776e-01 1.285999767510e-04 1.390609610462e-04
C2G3P2 13 1.419961158166e-02
2.574727242552e-01 1.361518971163e-04 4.538383274809e-05
1.534731228907e-01 2.081880663518e-04 4.480874221657e-05
-5.000000000000e-01 2.564400351638e-04 1.359691862835e-04
0.000000000000e+00 0.000000000000e+00 1.000000000000e-04
C2G4P0 13 6.623074051181e-01
-1.903590801157e-01 1.351522345620e-04 6.320538549037e-05
1.638124104311e-01 4.900000003979e-05 4.344285420353e-04
-3.483253686255e-02 1.959773185383e-04 1.900000089622e-05
0.000000000000e+00 0.000000000000e+00 1.000000000000e-04
C2G4P1 13 2.408772401815e-01
3.925246282702e-01 1.357513941429e-04 8.396067689745e-05
-4.902812338472e-01 1.683788447129e-04 1.564437193367e-04
4.658099096537e-01 2.405809667293e-04 7.408449280526e-05
-3.066282202890e-01 2.555319799801e-04 5.792709296461e-05
C2G4P2 13 7.187631831998e-02
7.799536842598e-02 2.548358962909e-04 5.286461296357e-05
-4.973075542238e-01 2.040545246000e-04 3.919025481013e-05
4.497650065514e-01 2.016036491303e-04 3.594436853070e-05
0.000000000000e+00 0.000000000000e+00 1.000000000000e-04
C2G5P0 13 7.558322024148e-01
8.293722356960e-02 2.560286256672e-04 7.636832464603e-05
8.559714728105e-03 4.900000000000e-05 2.312394409060e-05
-1.975527780049e-01 2.991132451367e-04 4.835845946358e-05
0.000000000000e+00 0.000000000000e+00 1.000000000000e-04
C2G5P1 13 2.822635778765e-01
-9.584081922645e-02 3.759173774180e-04 6.294359293699e-05
-4.418499119620e-01 4.957286229688e-05 9.275569464483e-04
4.869328188489e-01 2.902225209058e-04 9.776480854295e-05
-1.697529703496e-01 2.371183432805e-04 6.237547272626e-05

C2G5P2 13 2.145457143738e-01
 -1.852573052925e-01 1.289139802151e-04 2.471793930558e-04
 4.311514660487e-01 3.998055652179e-04 5.496377343521e-04
 3.352701537352e-03 2.903889848562e-04 1.900002967898e-05
 0.000000000000e+00 0.000000000000e+00 1.000000000000e-04
 C2G6P0 13 7.458520652870e-01
 4.979148207785e-01 4.900000120372e-05 5.427210374667e-05
 -1.307423772000e-01 3.067175347292e-04 4.191409560851e-05
 -4.414612733231e-01 5.005125777255e-05 4.964729730188e-05
 0.000000000000e+00 0.000000000000e+00 1.000000000000e-04
 C2G6P1 13 2.842386810811e-01
 2.796676130664e-01 5.637916789119e-05 7.347201022315e-05
 1.838626193814e-02 1.518007178024e-04 3.236747854280e-05
 1.448797309348e-01 2.960663242627e-04 5.990100511386e-05
 -4.891997301403e-01 4.900030196148e-05 1.244340936386e-04
 C2G6P2 13 5.662610538971e-02
 4.892311126720e-01 5.576485391803e-05 6.694929026830e-05
 -4.891993473872e-01 5.702281450031e-05 6.418520803081e-05
 3.255077625566e-02 3.240050944856e-04 3.227856889214e-05
 0.000000000000e+00 0.000000000000e+00 1.000000000000e-04
 C2G7P0 13 7.080971357863e-01
 -2.472717287605e-02 1.249632855362e-04 6.276498395406e-05
 4.983570775611e-01 1.181252506328e-04 6.459469898801e-04
 -1.995295177105e-01 3.163856631089e-04 5.783818891996e-05
 0.000000000000e+00 0.000000000000e+00 1.000000000000e-04
 C2G7P1 13 1.619911058057e-01
 1.682653023939e-02 5.271415179227e-05 3.385564861855e-05
 8.860993319138e-02 1.583722973131e-04 1.121833593536e-04
 1.514616410068e-01 3.182214961794e-04 6.011146218796e-05
 -4.655354281470e-01 1.774442750965e-04 3.955791347852e-04
 C2G7P2 13 9.545711203647e-02
 4.596257223560e-01 9.421638061072e-05 4.583200556200e-05
 -4.829964968900e-01 9.298698154348e-05 4.774331605350e-05
 5.569256990631e-02 3.183926202802e-04 4.647815870424e-05
 0.000000000000e+00 0.000000000000e+00 1.000000000000e-04
 C2G8P0 13 8.736435472031e-01
 -3.822716394579e-01 5.158428901222e-05 6.195731537198e-05
 3.937977261652e-01 5.171334141011e-05 5.933934137801e-05
 -6.424776845912e-02 3.045170667198e-04 2.901356086201e-05
 0.000000000000e+00 0.000000000000e+00 1.000000000000e-04
 C2G8P1 13 1.463117639197e-01
 -3.080302913071e-01 1.789064079827e-04 1.434659838770e-04
 2.933802709595e-02 1.264909114203e-04 4.315204139520e-05
 5.170827117659e-02 3.113651438495e-04 1.900003821734e-05
 2.314152441877e-01 2.178416361020e-04 1.099243668221e-04

A CALIBRATION FILES FOR 2012

```
#Parametrization of the probability functions for kaons
#the naming is in the format C<cedarNumber>G<groupNumber>K<hits>
#the next value represents the number of parameters used. The formula is:
#P0 + P1 * atan[ (CEDr - P2) / P3 ] + P4 * atan[ (CEDr - P5) / P6 ] + ...
C2G0K0 13 2.997628959633e-01
      1.712266738745e-01 1.025664495223e-04 1.900000001943e-05
      1.403871962374e-01 7.671171144690e-05 1.900000000000e-05
      -1.850270159366e-01 3.044067711603e-04 4.349551559481e-05
      0.000000000000e+00 0.000000000000e+00 1.000000000000e-04
C2G0K1 13 6.588449842510e-01
      1.477132885778e-01 3.034765100049e-04 2.570646780917e-05
      -3.825553578997e-01 1.002779583054e-04 2.714748110101e-05
      -3.193521163645e-01 7.525300916910e-05 2.861686431347e-05
      4.346436463560e-01 8.683217287428e-05 4.510039950097e-05
C2G1K0 13 3.224811274058e-01
      -3.327326632706e-01 6.048481186132e-05 1.571893929141e-04
      5.000000000000e-01 1.080540160980e-04 3.489482550045e-05
      -1.697790199666e-01 3.147058921516e-04 2.748598335141e-05
      0.000000000000e+00 0.000000000000e+00 1.000000000000e-04
C2G1K1 13 2.125318992808e-01
      4.994552525669e-01 6.659384810607e-05 2.019024515288e-05
      -3.684994931967e-01 6.543054974995e-05 1.900000009030e-05
      7.572158999981e-02 3.029048840887e-04 2.893705155732e-05
      -1.889218509292e-01 1.252093342661e-04 2.566977705359e-05
C2G1K2 13 6.153283562545e-01
      -1.451073174769e-01 1.004880395246e-04 1.900000000086e-05
      -1.406412017426e-01 7.380676243941e-05 1.900000000089e-05
      1.866863224107e-01 3.335859064303e-04 8.011071824143e-05
      0.000000000000e+00 0.000000000000e+00 1.000000000000e-04
C2G2K0 13 9.958282627315e-02
      1.403914074924e-01 1.228996462913e-04 2.710412883093e-05
      3.139980593165e-01 1.861498245760e-04 4.464422268276e-05
      -5.000000000000e-01 2.884270615100e-04 1.324459741496e-04
      0.000000000000e+00 0.000000000000e+00 1.000000000000e-04
C2G2K1 13 3.500712307757e-01
      4.388083132369e-02 7.026877940788e-05 1.900000247251e-05
      -5.000000000000e-01 1.694115585812e-04 7.532022458435e-05
      3.139750270444e-01 3.039242576725e-04 1.303349031397e-04
      2.393953269750e-01 1.069682805671e-04 3.194075811149e-05
C2G2K2 13 5.533024685789e-01
      -5.814439369440e-02 8.336071946878e-05 1.900000002563e-05
      -2.174865727811e-01 1.145997013969e-04 2.546958839279e-05
      1.147863830811e-01 3.027023527200e-04 2.942461804673e-05
      0.000000000000e+00 0.000000000000e+00 1.000000000000e-04
```

C2G3K0 13 2.488048779592e-01
 -7.376523175731e-03 4.900000042321e-05 1.900000099223e-05
 3.966479080695e-01 3.236163639331e-04 1.082046612037e-04
 -2.059323215392e-01 3.236898999142e-04 4.711039979672e-05
 0.000000000000e+00 0.000000000000e+00 1.000000000000e-04
 C2G3K1 13 2.461608469103e-01
 4.674130347472e-02 1.687077081808e-04 1.900799419139e-05
 -2.794472656256e-02 5.107787166486e-05 1.412590641878e-04
 7.436412219051e-02 1.136159049836e-04 2.624440907822e-05
 -7.960012873965e-02 3.938295627999e-04 5.309302833351e-05
 C2G3K2 13 5.361718380678e-01
 5.315206295079e-02 3.287037890915e-04 1.900000000000e-05
 -5.000000000000e-01 1.146306227947e-04 9.813832211789e-05
 2.662725929134e-01 5.392115870259e-05 8.112200882298e-05
 0.000000000000e+00 0.000000000000e+00 1.000000000000e-04
 C2G4K0 13 1.687236475812e-01
 7.113669341089e-03 9.988779813436e-05 1.900000001484e-05
 5.000000000000e-01 3.254265849236e-04 2.366699271885e-05
 -4.312007789861e-01 3.285132462864e-04 1.900000004371e-05
 0.000000000000e+00 0.000000000000e+00 1.000000000000e-04
 C2G4K1 13 2.661699109217e-01
 4.399894404372e-01 6.469079472513e-05 1.900002792875e-05
 -4.606326147938e-01 6.420416250047e-05 1.992585774443e-05
 1.329683418526e-01 1.473297842672e-04 1.285266189031e-04
 -1.939540171209e-02 2.530719859195e-04 1.900000007586e-05
 C2G4K2 13 5.602667264728e-01
 -5.000000000000e-01 6.738734467548e-05 9.779215728119e-05
 4.023477793097e-01 4.900000004164e-05 8.480914056812e-05
 -5.101459925552e-02 2.995347120099e-04 1.900000000260e-05
 0.000000000000e+00 0.000000000000e+00 1.000000000000e-04
 C2G5K0 13 1.567566173104e-01
 6.682817215789e-02 1.339276088322e-04 4.728966492850e-05
 4.646476023305e-01 2.722282269920e-04 5.601494419298e-05
 -4.516048111886e-01 2.895525618605e-04 5.664603768768e-05
 0.000000000000e+00 0.000000000000e+00 1.000000000000e-04
 C2G5K1 13 2.557049185399e-01
 4.082363669862e-01 1.152376039324e-04 4.951508080879e-05
 -5.000000000000e-01 1.174888785383e-04 2.523767518845e-05
 3.021243319223e-01 1.155520421017e-04 1.900000000059e-05
 -1.258972242181e-01 2.665180712692e-04 6.305234638958e-05

A CALIBRATION FILES FOR 2012

C2G5K2 13 5.929591149996e-01
8.924015695921e-02 3.149153686166e-04 1.900000010435e-05
-5.000000000000e-01 8.576156116232e-05 7.429529356284e-05
1.796493836213e-01 5.426724583071e-05 4.891971336968e-05
0.000000000000e+00 0.000000000000e+00 1.000000000000e-04

C2G6K0 13 1.340308410534e-01
-9.094263558029e-02 4.900000001601e-05 4.375542859231e-05
5.000000000000e-01 1.122961325155e-04 5.727585355504e-05
-2.778811558588e-01 3.058273454415e-04 4.538143704233e-05
0.000000000000e+00 0.000000000000e+00 1.000000000000e-04

C2G6K1 13 2.541485474779e-01
1.650605848618e-01 5.541369915726e-05 2.537089113133e-05
-1.804158617700e-01 1.384224135960e-04 2.746117128753e-05
9.554347112423e-02 3.026332372914e-04 1.900000003920e-05
-2.646035615713e-02 2.059960995066e-04 1.900000029255e-05

C2G6K2 13 4.617428105623e-01
4.601548595303e-01 4.900000107578e-05 2.330430338225e-04
9.132715309407e-02 3.215764712429e-04 5.794053450429e-05
-5.000000000000e-01 7.148103744673e-05 4.742545142995e-05
0.000000000000e+00 0.000000000000e+00 1.000000000000e-04

C2G7K0 13 3.157393410980e-01
-4.439637746541e-01 4.900000130773e-05 3.128217008670e-04
5.000000000000e-01 8.176226033713e-05 3.750177229230e-05
-1.606425638798e-01 3.123584776090e-04 3.140188501521e-05
0.000000000000e+00 0.000000000000e+00 1.000000000000e-04

C2G7K1 13 1.500677971319e-01
2.389615703725e-01 4.907934950911e-05 3.177185379099e-05
-3.813750559622e-01 9.303383073069e-05 3.902389903917e-05
4.789431053421e-01 1.359639676724e-04 4.986118535815e-04
3.032113559598e-02 2.962923334915e-04 2.002379676603e-05

C2G7K2 13 5.573131611578e-01
2.617982144190e-01 6.822850924903e-05 8.583040373766e-05
-5.000000000000e-01 5.722544140346e-05 3.471983747386e-05
9.718344695885e-02 3.177067827786e-04 2.111355158291e-05
0.000000000000e+00 0.000000000000e+00 1.000000000000e-04

C2G8K0 13 2.517456419912e-01
-5.000000000000e-01 2.380981056515e-04 1.112431799104e-04
4.346259515311e-01 6.419780228779e-05 3.339885750281e-05
1.419299114157e-01 2.072106335193e-04 4.105562580474e-05
0.000000000000e+00 0.000000000000e+00 1.000000000000e-04

C2G8K1 13 6.300536217084e-01
-4.984183249114e-01 6.455894726886e-05 3.551115324203e-05
4.303287621986e-01 1.100849290373e-04 1.252588556686e-04
3.610741742568e-01 3.001660158537e-04 6.151190146132e-05
-4.967628914873e-01 2.550710225733e-04 1.678482905593e-04

```
#Parametrization for the likelihood limits.  
#In order to make it flexible it is given as a TF1 string from ROOT  
LIMIT C2G0PKLIM -7.9+2.0*TMath::ATan((x-5e-05)/3.8e-05)  
LIMIT C2G0PPLIM -11.8+5.8*TMath::ATan((x+7e-06)/2.0e-05)  
LIMIT C2G0KKLIM -5.7+2.1*TMath::ATan((x-4e-05)/5.0e-05)  
LIMIT C2G0KPLIM -7.0+1.6*TMath::ATan((x-5e-05)/2.0e-05)  
LIMIT C2G1PKLIM -7.7+1.5*TMath::ATan((x-5e-05)/2.0e-05)  
LIMIT C2G1PPLIM -11.5+5.8*TMath::ATan((x+7e-06)/2.0e-05)  
LIMIT C2G1KKLIM -7.8+3.6*TMath::ATan((x-4e-06)/3.9e-05)  
LIMIT C2G1KPLIM -6.6+1.6*TMath::ATan((x-5e-05)/2.0e-05)
```

A.3 ECAL2 position dependent correction file

```

// Comments can be used, the are started with '///',
// and run till the end of the current line.
// Options are not case sensitive.

//production from which the parameters were obtained
Tag primp2012t11

// new pos = old pos - correction
// energy = p0
// parametrizes ( P1*atan((energy-P2)/P3)
//               + P4*atan((energy-P5)/P6) + P7) * sin(P8*dist)
//               + ( P9*atan((energy-P10)/P11)
//               + P12*atan((energy-P13)/P14) + P15)
//               *sin(P16*dist)*sin(P16*dist)*sin(P16*dist);

// Position correction along X
// P0 = lowest energy for which the correction should be applied
// CorrectionPositionX  0.000   1.094   34.5195 -8.12087\
//                    713.952 -370.857  78876.8 -3.59556 25.4359\
//                    21.961  -16.2008  -22.9661 24.5323 -15.6048\
//                    3.622   0.164051835696594955
// Position correction along Y
// CorrectionPositionY   0.      0.198097 -64.1109 -0.0448388\
//                    309.396  101.701 341424 -0.0243823 -0.457019\
//                    39.9254   3.71998 -0.37124 126.81 -6.60438 0.291758\
//                    0.164051835696594955

// Correct the energy depending on the cluster position in the cell
//
// possible shapes:
// - quarter:
// all corrections are projected to values in the upper right (x>0, y>0)
// quarter of the cell, the number of corrections is the square of the
// number of bins given
// first value is correction for cell closest to cell center, then column-wise
// along y axis

```

```

//All parameters are given in cm, z stands for the energy
//          <cellType> <threshold> <usedMethod>
CorrectionEnergyPosDep Shashlik -0.5
quarterfunction
(z
  -(-3.78765-2.90262*TMath::ATan(2.51816e-02*(z-1.07450e+02)))
  -(-0.49489*TMath::ATan(0.0956023*(z-50.624)))
  +(
    (2.93524+4.45274*TMath::ATan(0.0197639*(z-45.9495)))
    *TMath::Exp(-0.5*((x-0.850)**2
  )
  +(y-0.850)**2)/(0.2)**2)
  -1.0*TMath::Exp(-0.5*((x-0.750)**2
  +(y-0.750)**2)/(0.2)**2)
  -((0.80000+0.54*TMath::ATan(0.34*(z-35)))
    *TMath::Exp(-0.5*((x-0.319)**2+(y-0.319)**2)/(0.2)**2)
  )
  -((1.67469-0.434183*TMath::ATan(-0.0820287*(z-118.792))
    -0.777134*TMath::ATan(-0.159251*(z-28.6608)))
    *TMath::Exp(-0.5*((x-0.319)**2+(y-1.319)**2)/(0.2)**2)
  )
  -((1.85643-0.690931*TMath::ATan(-0.093842*(z-103.617))-0.547604
    *TMath::ATan(-1*(z-28.6325)))
    *TMath::Exp(-0.5*((x-1.319)**2+(y-1.319)**2)/(0.2)**2)
  )
  -((2.12864-0.989622*TMath::ATan(-0.033194*(z-106.476))
    -0.577403*TMath::ATan(-1*(z-39.9827)))
    *TMath::Exp(-0.5*((x-1.319)**2+(y-0.319)**2)/(0.2)**2)
  )
  -((1.57337+1.43701*TMath::ATan(0.0347502*(z-114.784)))
    *TMath::Exp(-0.5*(x-1.915)**2/(0.256)**2)
  )
  -( 2.65/1.6*(0.80000+0.54*TMath::ATan(0.34*(z-35)))
    *TMath::Exp(-0.5*((x-1.915)**2/(0.180)**2+y**2/0.48**2)) )
  -(
    (0.35714*TMath::ATan(.5*(z-4))+0.35714*TMath::ATan(-.5*(z-23)))
    *TMath::Exp(-0.5*((x-1.915)**2/(0.480)**2
  )
  +(y-1.915)**2/0.48**2))
  +(1.2+.8*TMath::ATan(-.1*(z-1)))*TMath::Exp(-0.5*((x-0.800)**2
  +(y-0.800)**2)/(0.2)**2)
  +(0.5*TMath::ATan(0.5*(z-23))+0.5*TMath::ATan(-1*(z-39)))
    *TMath::Exp(-0.5*((x-1.100)**2+(y-1.100)**2)/(0.2)**2)
  +(0.2*TMath::ATan(0.5*(z-23))+0.2*TMath::ATan(-1*(z-39)))
    *TMath::Exp(-0.5*((x-0.300)**2+(y-1.400)**2)/(0.3)**2)+0.35
  )*0.983

```


Bibliography

- [1] C. Adolph et al. Measurement of the charged-pion polarizability. *Phys. Rev. Lett.*, 114:062002, Feb 2015. (Cited on pages , 23, 53, 59, 60, 61, 62, 75, 76, 115, and 117.)
- [2] C. Adolph, R. Akhunzyanov, M.G. Alexeev, et al. Collins and sivers asymmetries in muonproduction of pions and kaons off transversely polarised protons. *Physics Letters B*, 744:250 – 259, 2015. (Cited on page 1.)
- [3] F. Schwabl. *Quantenmechanik (QM I)*:. Springer-Lehrbuch. Springer, 2002. (Cited on page 2.)
- [4] K. A. Olive et al. Review of Particle Physics. *Chin. Phys.*, C38:090001, 2014. (Cited on pages 2, 3, 71, 84, 95, and 115.)
- [5] H. Leutwyler. On the foundations of chiral perturbation theory. *Annals Phys.*, 235:165–203, 1994. (Cited on page 3.)
- [6] Juerg Gasser, Mikhail A. Ivanov, and Mikko E. Sainio. Revisiting $\gamma\gamma \rightarrow \pi^+\pi^-$ at low energies. *Nucl. Phys.*, B745:84–108, 2006. (Cited on pages 3, 4, 5, 6, 76, 78, and 79.)
- [7] Sinya Aoki et al. Review of lattice results concerning low-energy particle physics. *Eur. Phys. J.*, C74:2890, 2014. (Cited on page 3.)
- [8] M. Bychkov et al. New Precise Measurement of the Pion Weak Form Factors in $\pi^+ \rightarrow e^+\nu\gamma$ Decay. *Phys. Rev. Lett.*, 103:051802, 2009. (Cited on page 4.)
- [9] Mikhail A. Ivanov and T. Mizutani. Pion and kaon polarizabilities in the quark confinement model. *Phys. Rev.*, D45:1580–1601, 1992. (Cited on page 4.)
- [10] L. V. Fil'kov and V. L. Kashevarov. Determination of π^\pm meson polarizabilities from the $\gamma\gamma \rightarrow \pi^+\pi^-$ process. *Phys. Rev. C*, 73:035210, Mar 2006. (Cited on pages 4 and 5.)
- [11] B. Pasquini, D. Drechsel, and S. Scherer. The Polarizability of the pion: No conflict between dispersion theory and chiral perturbation theory. *Phys. Rev.*, C77:065211, 2008. (Cited on pages 4 and 76.)

BIBLIOGRAPHY

- [12] B. Pasquini, D. Drechsel, and S. Scherer. Reply to “comment on ‘polarizability of the pion: No conflict between dispersion theory and chiral perturbation theory’”. *Phys. Rev. C*, 81:029802, Feb 2010. (Cited on pages 4 and 76.)
- [13] M. R. Pennington. What we can learn by measuring $\gamma\gamma \rightarrow \pi\pi$ at DAPHNE. In *2nd DAPHNE Physics Handbook:531-558*, pages 531–558, 1995. (Cited on page 4.)
- [14] Yu. M. Antipov et al. Measurement of pi- Meson Polarizability in Pion Compton Effect. *Phys. Lett.*, B121:445–448, 1983. (Cited on pages 4 and 5.)
- [15] T. A. Aibergenov, P. S. Baranov, O. D. Beznisko, et al. Radiative Photoproduction of Pions and Pion Compton Scattering. *Czech. J. Phys.*, B36:948–951, 1986. (Cited on pages 4 and 5.)
- [16] J. Ahrens et al. Measurement of the π^+ meson polarizabilities via the $\gamma p \rightarrow \gamma \pi^+ n$ reaction. *Eur. Phys. J.*, A23:113–127, 2005. (Cited on pages 4 and 5.)
- [17] D. Babusci, S. Bellucci, G. Giordano, et al. Chiral symmetry and pion polarizabilities. *Phys. Lett.*, B277:158–162, 1992. (Cited on page 5.)
- [18] Christoph Berger et al. Pion Pair Production in Photon-photon Interactions. *Z. Phys.*, C26:199, 1984. (Cited on page 5.)
- [19] D. Morgan and M. R. Pennington. Low-energy $\gamma\gamma \rightarrow \pi\pi$ Cross-section and the QED Born Amplitude. *Phys. Lett.*, B192:207–211, 1987. (Cited on page 5.)
- [20] J. Boyer et al. Two photon production of pion pairs. *Phys. Rev.*, D42:1350–1367, 1990. (Cited on page 5.)
- [21] John F. Donoghue and Barry R. Holstein. Photon-photon scattering, pion polarizability and chiral symmetry. *Phys. Rev.*, D48:137–146, 1993. (Cited on page 5.)
- [22] A. E. Kaloshin and V. V. Serebryakov. π^+ and π^0 polarizabilities from $\gamma\gamma \rightarrow \pi\pi$ data on the base of S matrix approach. *Z. Phys.*, C64:689–694, 1994. (Cited on page 5.)
- [23] H. Marsiske, D. Antreasyan, Bartels, et al. Measurement of $\pi^0\pi^0$ production in two-photon collisions. *Phys. Rev. D*, 41:3324–3335, Jun 1990. (Cited on page 5.)
- [24] H. Aihara, M. Alston-Garnjost, R. E. Avery, et al. Pion and kaon pair production in photon-photon collisions. *Phys. Rev. Lett.*, 57:404–407, Jul 1986. (Cited on page 5.)
- [25] H. J. Behrend et al. An Experimental study of the process $\gamma\gamma \rightarrow \pi^+\pi^-$. *Z. Phys.*, C56:381–390, 1992. (Cited on page 5.)
- [26] Fumiaki Yabuki, Koya Abe, Katsuya Amako, et al. Study of $\pi^+\pi^-$ pair production in a two-photon process at tristan. *Journal of the Physical Society of Japan*, 64(2):435–447, 1995. (Cited on page 5.)

- [27] A. Heister, Evelina Bouhova-Thacker, Christopher Bowdery, et al. Exclusive production of pion and kaon meson pairs in two photon collisions at lep. *Physics Letters B*, 569(3-4):140–150, 9 2003. (Cited on page 5.)
- [28] H. Nakazawa et al. Measurement of the $\gamma\gamma \rightarrow \pi^+\pi^-$ and $\gamma\gamma \rightarrow K^+K^-$ processes at energies of 2.4-GeV to 4.1-GeV. *Phys. Lett.*, B615:39–49, 2005. (Cited on page 5.)
- [29] T. Nagel. *Measurement of the Charged Pion Polarizability*. Dissertation, Technische Universität München, 2012. (Cited on pages 5, 53, 65, 66, 68, 102, and 113.)
- [30] D. Drechsel. *Pion Polarizability: A Cornerstone of Hadronic Physics*. 2013. (Cited on page 4.)
- [31] H. Primakoff. Photo-production of neutral mesons in nuclear electric fields and the mean life of the neutral meson. *Phys. Rev.*, 81:899–899, Mar 1951. (Cited on pages 4 and 6.)
- [32] I. Larin, László L. Jenkovszky, and Aleksander Polański. *A Precision Measurement of the Neutral Pion Life Time: Updated Results from the PrimEx Experiment*, pages 157–162. Springer Netherlands, Dordrecht, 2009. (Cited on page 6.)
- [33] C. F. v. Weizsäcker. Ausstrahlung bei stößen sehr schneller elektronen. *Zeitschrift für Physik*, 88(9):612–625, 1934. (Cited on page 6.)
- [34] E. J. Williams. Nature of the high energy particles of penetrating radiation and status of ionization and radiation formulae. *Phys. Rev.*, 45:729–730, May 1934. (Cited on page 6.)
- [35] J.D. Jackson and K. Müller. *Klassische Elektrodynamik*. de Gruyter, 2002. (Cited on pages 6 and 67.)
- [36] V.A. Petrunkin. Scattering of low-energy photons on a zero-spin particle. *Nuclear Physics*, 55:197 – 206, 1964. (Cited on page 8.)
- [37] D. Drechsel and L. V. Filkov. Compton scattering on the pion and radiative pion photoproduction from the proton. *Z. Phys.*, A349:177–184, 1994. (Cited on pages 8 and 76.)
- [38] A. S. Galperin and Guenakh Mitselmakher. Calculation of Ultrarelativistic Pion Bremsstrahlung Cross-section on Nuclei With the Allowance for Pion Polarization. *Submitted to: Yadernaya Fiz.*, 1980. (Cited on page 9.)
- [39] P. Abbon et al. The compass experiment at cern. *Nucl. Instrum. Methods Phys. Res.*, A, 577:455–518, Jan 2007. (Cited on pages 14, 65, and 66.)

BIBLIOGRAPHY

- [40] Alexander Austregesilo. *Central Production of Two-Pseudoscalar Meson Systems at the COMPASS Experiment at CERN*. Dissertation, Technische Universität München, München, 2014. (Cited on pages 15 and 91.)
- [41] Stefanie Grabmüller. *Cryogenic Silicon Detectors and Analysis of Primakoff Contributions to the Reaction $\pi^- \text{Pb} \rightarrow \pi^- \pi^+ \pi^- \text{Pb}$ at COMPASS*. Dissertation, Technische Universität München, "München", 2012. (Cited on page 15.)
- [42] Karl Bicker. *Construction and Commissioning of a Cooling and Support Structure for the Silicon Detectors for the COMPASS Experiment*. Diploma thesis, Technische Universität München, "München", 2011. (Cited on page 15.)
- [43] B. Holzgartner. *Water Cooling for the Frontend Electronics and a modular Phase Separator for the COMPASS Silicon Detectors and Alignment for the 2012 Primakoff Run*. Diploma thesis, Technische Universität München, 2012. (Cited on pages 15 and 104.)
- [44] P. Abbon, C. Adolph, R. Akhunzyanov, et al. The COMPASS setup for physics with hadron beams. *Nucl. Instrum. Methods Phys. Res., A*, 779:69 – 115, 2015. (Cited on pages 15, 16, 19, 20, 21, 42, 54, 67, 90, and 91.)
- [45] F. Binon, V.M. Buyanov, S.V. Donskov, et al. Hodoscope multiphoton spectrometer gams-2000. *Nuclear Instruments and Methods in Physics Research Section A: Accelerators, Spectrometers, Detectors and Associated Equipment*, 248(1):86 – 102, 1986. (Cited on pages 16 and 18.)
- [46] Vladimir Polyakov. Radiation hard shashlik calorimeter for compass experiment. <http://goo.gl/4lJ8uG>. (Cited on page 17.)
- [47] M. Adamovich et al. WA92: A fixed target experiment to trigger on and identify beauty particle decays. *Nucl. Instrum. Meth.*, A379:252–270, 1996. (Cited on page 19.)
- [48] P. Astbury et al. Measurement of deep inelastic compton scattering of high energy photons. *Phys. Lett.*, B152:419, 1985. (Cited on page 19.)
- [49] A. Mann, A. M. Dinkelbach, B. Grube, et al. The universal sampling adc readout system of the compass experiment. In *IEEE Nuclear Science Symposium*, pages 2225–2228, 2009. (Cited on pages 19 and 23.)
- [50] Claude Bovet, R Maleyran, Alfredo Placci, and Massimo Placidi. The CEDAR (Cerenkov Differential Counters with Achromatic Ring Focus) project. *IEEE Trans. Nucl. Sci.*, 25(CERN-SPS-EBP-77-19):572–576. 9 p, Sep 1977. (Cited on page 19.)
- [51] F. Tessarotto S. Levorato. Light RICH-1 beam pipe. 2012. (Cited on page 20.)
- [52] F. Tessarotto, P Abbon, M Alexeev, et al. Long term experience and performance of COMPASS RICH-1. *Journal of Instrumentation*, 9(09):C09011, 2014. (Cited on page 20.)

- [53] Stefan Huber. *Development of a Digital Trigger for Electromagnetic Calorimeter*. Diploma thesis, Technische Universität München, München, 2010. (Cited on pages 23, 25, and 53.)
- [54] M. Krämer, J. Friedrich, S. Huber, et al. A digital calorimetric trigger for the compass experiment at cern. In *TWEPP-09: Topical Workshop on Electronics for Particle Physics*, pages 182–185, 2009. (Cited on page 23.)
- [55] Stefan Huber, Jan Friedrich, Bernhard Ketzer, et al. A digital trigger for the electromagnetic calorimeter at the COMPASS experiment. *IEEE Trans. Nucl. Sci.*, 58:1719–1722, 2011. (Cited on page 23.)
- [56] Markus Krämer. *Evaluation and Optimization of a Digital Calorimetric Trigger and Analysis of Pion-Photon-Interactions in $\pi^- Ni \rightarrow \pi^- \pi^0 \pi^0 Ni$ Reactions at COMPASS at CERN*. Dissertation, Technische Universität München, München, 2016. (Cited on pages 23, 31, and 33.)
- [57] A. Mann, I. Konorov, and S. Paul. A versatile sampling adc system for on-detector applications and the advancedtca crate standard. In *15th IEEE-NPSS Real-Time Conference*, 2007. (Cited on page 23.)
- [58] Texas Instruments. 8-Channel, 12-Bit, 40MSPS Analog-to-Digital Converter with Serial LVDS Interface. <http://www.ti.com/lit/ds/symlink/ads5270.pdf>. (Cited on page 23.)
- [59] Cypress Semiconductor. HOTLink design considerations. http://physics.bu.edu/mcen/MCCM_Parts/Hotlinkdesignconsiderations.pdf. (Cited on page 24.)
- [60] B. Grube. *A Trigger Control System for COMPASS and a Measurement of the Transverse Polarization of Λ and Ξ Hyperons from Quasi-Real Photo-Production*. Dissertation, Technische Universität München, 2006. (Cited on pages 24 and 38.)
- [61] XILINX. Virtex-4 FPGA user guide. http://www.xilinx.com/support/documentation/user_guides/ug070.pdf. (Cited on page 25.)
- [62] Robert Konopka. *Real time data processing and feature extraction of calorimeter data in COMPASS*. Diploma thesis, Technische Universität München, München, 2009. (Cited on page 27.)
- [63] Jan Friedrich. private communication. (Cited on pages 31 and 77.)
- [64] Cisco Systems. CISCO 1000BASE-T SFP datasheet. <http://www.future-x.de/images/datasheet/s101552.pdf>. (Cited on page 38.)

BIBLIOGRAPHY

- [65] XILINX. Virtex-6 FPGA GTX transceivers. http://www.xilinx.com/support/documentation/user_guides/ug366.pdf. (Cited on page 38.)
- [66] XILINX. Linear feedback shift registers in virtex devices. http://www.xilinx.com/support/documentation/application_notes/xapp210.pdf, April 2007. (Cited on page 40.)
- [67] Markus Krämer. private communication. (Cited on pages 42, 67, and 91.)
- [68] XILINX. Microblaze soft processor core. <http://www.xilinx.com/products/design-tools/microblaze.html>. (Cited on page 42.)
- [69] Johannes Bernhard. private communication. (Cited on pages 45 and 47.)
- [70] Alexey Guskov. private communication. (Cited on pages 47 and 71.)
- [71] A. Guskov. *Analysis of the charged pion polarizability measurement method at COMPASS experiment*. Dissertation, Università degli Studi di Torino, 2010. (Cited on page 53.)
- [72] National Nuclear Data Center. Nudat 2 database. <http://www.nndc.bnl.gov/nudat2/reCenter.jsp?z=28&n=30>. (Cited on page 53.)
- [73] N. Kaiser and J. M. Friedrich. Radiative corrections to pion Compton scattering. *Nucl. Phys.*, A812:186–200, 2008. (Cited on pages 53, 64, 68, and 75.)
- [74] I.Ya. Pomeranchuk and I.M. Shumushkevich. On processes in the interaction of γ -quanta with unstable particles. *Nuclear Physics*, 23:452 – 467, 1961. (Cited on page 58.)
- [75] C. Dreisbach. *Study of elastic $\pi^- p$ scattering at COMPASS*. Master thesis, Technische Universität München, 2014. (Cited on page 59.)
- [76] Jan Friedrich and Markus Krämer. Reconstruction of the pion beam energy from beam optics. 2012. (Cited on pages 63 and 92.)
- [77] M Buénerd. Prospects for hadron electromagnetic polarizability measurement by radiative scattering on a nuclear target. *Nucl. Instrum. Methods Phys. Res., A*, 361(1–2):111 – 128, 1995. (Cited on page 64.)
- [78] J. M. Friedrich. *Chiral Dynamics in Pion-Photon Reactions*. Habilitation thesis, Technische Universität München, 2012. (Cited on pages 64, 65, 66, 68, and 75.)
- [79] N. Kaiser and J. M. Friedrich. Cross-sections for low-energy pi- gamma reactions. *Eur. Phys. J.*, A36:181–188, 2008. (Cited on pages 64 and 75.)
- [80] U. Burgi. Charged pion pair production and pion polarizabilities to two loops. *Nucl. Phys.*, B479:392–426, 1996. (Cited on page 64.)

- [81] R. Brun, F. Bruyant, Federico Carminati, et al. GEANT Detector Description and Simulation Tool. 1994. (Cited on page 65.)
- [82] R. Brun, M. Goossens, and J. Zoll. Zebra users guide. program library q100. CERN, 1991. (Cited on page 66.)
- [83] M. Leeb. *Optimization of the Clustering and Tracking Algorithms of the Silicon Microstrip Detectors for the COMPASS Experiment*. Diploma thesis, Technische Universität München, 2011. (Cited on pages 66, 104, and 112.)
- [84] C. Bovet, R. Maleyran, L. Piemontese, A. Placci, and M. Placidi. The Cedar Counters for Particle Identification in the SPS Secondary Beams: A Description and an Operation Manual. 1982. (Cited on page 67.)
- [85] Jan Friedrich. Cedar performance 2009. COMPASS note, 2010. (Cited on pages 67, 81, 83, and 85.)
- [86] Alexey Guskov. Muon background and systematics of pion polarizabilities measurement, 2012. COMPASS analysis meeting. (Cited on page 68.)
- [87] Göran Fäldt and Ulla Tengblad. Coulomb-nuclear interference in pion-nucleus bremsstrahlung. *Phys. Rev. C*, 79:014607, Jan 2009. (Cited on page 73.)
- [88] Jan Friedrich. private communication. (Cited on page 73.)
- [89] Alexey Guskov. private communication. (Cited on pages 73 and 74.)
- [90] Barbara Pasquini. private communication. (Cited on pages 76 and 77.)
- [91] The COMPASS collaboration. Compass-II proposal. 2010. (Cited on page 81.)
- [92] Prometeusz Jasinski. *Analysis of diffractive dissociation of K^- into $K^-\pi^+\pi^-$ on a liquid hydrogen target at the COMPASS spectrometer*. PhD thesis, Johannes Gutenberg-Universität in Mainz, 2012. (Cited on page 81.)
- [93] Lau Gatignon. private communication. (Cited on page 82.)
- [94] Tobias Weisrock and Eva-Maria Kabuß. Using bayesian methods for particle identification in the cedars. (Cited on page 84.)
- [95] Stefan Wallner. private communication. (Cited on pages 89 and 115.)
- [96] H.W. Atherton et al. Precise measurements of particle production by 400 gev/c protons on beryllium targets. Yellow report, CERN, 1980. (Cited on page 91.)
- [97] Florian Haas. *Two-Dimensional Partial-Wave Analysis of Exclusive 190 GeV π^-p Scattering into the $\pi^-\pi^-\pi^+$ Final-State at COMPASS (CERN)*. Dissertation, Technische Universität München, München, 2014. (Cited on page 91.)

BIBLIOGRAPHY

- [98] Jan Friedrich. private communication. (Cited on page 92.)
- [99] Sergei Gerassimov. private communication. (Cited on page 99.)
- [100] Sebastian Uhl. private communication. (Cited on page 103.)
- [101] V.Blobel and C. Kleinwort. A New method for the high precision alignment of track detectors. In *Advanced Statistical Techniques in Particle Physics. Proceedings, Conference, Durham, UK, March 18-22, 2002.* (Cited on page 104.)
- [102] Yann Bedfer. private communications, <https://twiki.cern.ch/twiki/bin/view/Compass/DetectorStudies/PrimakEff>. (Cited on page 105.)
- [103] Tobias Kunz. *Entwicklung einer Simulationsumgebung für das COMPASS-II-Experiment mit Geant4.* Diploma thesis, Albert-Ludwigs-Universität Freiburg, 2011. (Cited on page 109.)
- [104] Tobias Szameitat. *Entwicklung einer Monte-Carlo-Simulation für das COMPASS-II-Experiment.* Diploma thesis, Albert-Ludwigs-Universität Freiburg, 2012. (Cited on page 109.)
- [105] S. Agostinelli et al. Geant4 - a simulation toolkit. *NIM*, A506(3):250 – 303, 2003. (Cited on page 109.)
- [106] Guenter Grindhammer and S. Peters. The Parameterized simulation of electromagnetic showers in homogeneous and sampling calorimeters. In *International Conference on Monte Carlo Simulation in High-Energy and Nuclear Physics - MC 93 Tallahassee, Florida, February 22-26, 1993, 1993.* (Cited on page 111.)
- [107] Tobias Szameitat and Christopher Regali. private communication. (Cited on page 111.)
- [108] Julian Seyfried. Master thesis in preparation, Technische Universität München, 2016. (Cited on pages 112 and 116.)
- [109] Dmytro Levit. private communications.